IMPERIAL

Approximation, Control and Observation of Complex Dynamical Systems

Ph.D Candidate: Zilong Gong

Supervisor: Giordano Scarciotti

A Thesis submitted in fulfillment of requirements for the degree of
Doctor of Philosophy

Control and Power Research Group
Department of Electrical and Electronic Engineering
Imperial College London
October 2024

Declaration of Originality

I hereby declare that the material contained within this thesis is my own work, except where other work is appropriately referenced. Any use of the first-person plural is for reasons of clarity.

Zilong Gong

Department of Electrical and Electronic Engineering

Imperial College London, London, UK

October 2024

Copyright Declaration

The copyright of this thesis rests with the author. Unless otherwise indicated, its contents are licensed under a Creative Commons Attribution-Noncommercial 4.0 International Licence (CC BY-NC).

Under this licence, you may copy and redistribute the material in any medium or format. You may also create and distribute modified versions of the work. This is on the condition that: you credit the author and do not use it, or any derivative works, for a commercial purpose.

When reusing or sharing this work, ensure you make the licence terms clear to others by naming the licence and linking to the licence text. Where a work has been adapted, you should indicate that the work has been changed and describe those changes.

Please seek permission from the copyright holder for uses of this work that are not included in this licence or permitted under UK Copyright Law.

Zilong Gong

Department of Electrical and Electronic Engineering

Imperial College London, London, UK

October 2024

Abstract

The present work contributes to the topics of approximation, control, and observation of complex dynamical systems. The thesis consists of three parts. The first part of the thesis considers the approximation of large-scale systems. First, the data-driven model order reduction (MOR) by moment-matching is considered, with a focus on multiple-input multiple-output (MIMO) systems. Then, the developed method is validated on a combined system of a 200-turbine wind farm interconnected to the IEEE 14-bus system. The second part of the thesis deals with three classes of state-feedback control problems for stochastic nonlinear systems. Exploiting a dynamic extension, approximate solutions are provided for optimal control problems and min-max zero-sum games while exact solutions are given for the H_∞ control problem. The level of approximation can be exactly quantified in terms of an additional cost, which gives the distance from the optimal solution. Finally, the observation of stochastic linear systems is presented in the last part of the thesis. An *a posteriori* method is considered to approximate the variations of the Brownian motion. Based on this approximation, a hybrid observer is constructed, with the property that the estimation error converges to zero asymptotically in probability as the sampling period tends to zero.

Acknowledgements

A relaxing PhD is usually not a qualified PhD. It is quite challenging when things are uncertain and complex. However, working with excellent people made my journey incredibly enjoyable.

I would like to express my sincere gratitude to my supervisor Giordano Scarciotti for giving me the opportunity to pursue a PhD at Imperial College London and for his endless support throughout my PhD. His profound knowledge, keen insight and rigorous attitude to research have deeply influenced me.

I would like to thank Adrià Junyent-Ferré, who is almost my unofficial second supervisor. I have benefited from his patient guidance and warm encouragement. Without these, I could not overcome the obstacles in my research and would have struggled longer.

I am grateful to all my colleagues and previous colleagues in the group. Special thanks to Alberto for the solid collaboration and kind help in my first year; Han, for inviting me to the weekly basketball game; Junyu, Zirui and Hanqing for their unlimited support and concern. The past four years are irreplaceable memories for me.

I would take this opportunity to thank my friends: Debraj, Mohammad Fahim, Guilin, Pudong, Guoxuan, Wangkun, Jianli and Kaiwen for various help. I am also grateful to other people in the Control and Power group.

Finally, I owe my sincere gratitude to my parents, who raised me with unconditional love, and my grandparents, who shaped me but left me forever during my PhD. They have deeply inspired me to follow in their footsteps on my extensive journey.

I dedicate this thesis to the memory of my beloved grandparents.

Contents

Declaration of Originality **3**

Copyright Declaration **5**

Abstract **7**

Acknowledgements **9**

Contents **13**

List of Figures **17**

List of Tables **23**

List of Symbols **25**

List of Abbreviations **27**

1 Introduction **28**

1.1 Background and Motivation 28

1.2 Thesis Outline 30

1.3 Notation 31

1.4 Publication 32

I Approximation **33**

2 Preliminary: Model Order Reduction by moment matching for SISO Systems 35

2.1 Introduction . . . 35

2.2 Model order reduction by moment-matching for linear systems . . . 36

2.3 Model order reduction by moment-matching for nonlinear systems . . . 42

2.4 Conclusion . . . 48

3 Preliminary: Wind turbine generator model 49

3.1 Wind turbine mechanism . . . 49

3.2 Generator dynamics . . . 53

3.3 Generator vector control . . . 56

3.4 Power converter . . . 57

3.5 Grid-side dynamics . . . 58

3.6 Grid-side control . . . 59

3.7 Wind Farm Model . . . 61

3.8 Conclusion . . . 62

4 Model Order Reduction of Large-scale Wind Farms: A Data-driven approach 63

4.1 Introduction . . . 63

4.2 Model-based model order reduction of MIMO systems . . . 67

4.3 Data-driven model order reduction of MIMO systems . . . 71

4.4 Application to large-scale wind farms . . . 80

4.5 Conclusion . . . 93

II Control 95

5 Approximate Solutions to Classes of State-Feedback Control Problems for Stochastic Nonlinear Systems 97

5.1 Introduction . . . 97

5.2 Preliminary: Stochastic Differential Equations . . . 99

5.3 Preliminaries: Three Classes of Problems . . . 102

5.4 Formulation of the Auxiliary Problems 107
5.5 Step 1: Design of the algebraic solution, extended value function and control u 110
5.6 Step 2: Design of the dynamic extension 114
5.7 Simulations 119
5.8 Conclusion 125

III Observation **127**

6 A Hybrid Observer for Stochastic Linear Systems **129**

6.1 Introduction 129
6.2 Preliminaries 131
6.3 Hybrid Stochastic Observer 134
6.4 Example: deterministic, idealistic and hybrid stochastic observer 141
6.5 Conclusion 149

7 Conclusions **150**

7.1 Contributions 150
7.2 Future Work 151

A Parameters **153**

Bibliography **156**

List of Figures

2.1 The diagram of the interconnected system in Theorem 2.1. 39

2.2 Bode plot of the FOM and ROMs. The solid blue line, black dotted line and red dashed line represent the FOM, ROM (model-based) and ROM_DD (data-driven), respectively. The cyan diamonds indicate the selected interpolation points. 42

2.3 The diagram of the interconnected system in Theorem 2.4. 44

2.4 Top: output of the FOM and ROMs. The solid purple line represents the FOM. The blue, red and yellow dashed lines represent ROMs constructed by the sets of basis functions Ω_1, Ω_2 and Ω_3, respectively. Bottom: corresponding error. 48

3.1 The diagram of the back-to-back converter. 57

4.1 The diagram of the direct interconnection. 69

4.2 The diagram of the swapped interconnection. 70

4.3 The diagram of the two-sided interconnection. 71

4.4 Algorithmic overview of the method 77

4.5 Bode plot of the right side moment-matching along the tangential direction l. The solid blue line, black dotted line and red dashed line represent the quantities for the FOM, ROM (model-based) and ROM_DD (data-driven), respectively. 78

4.6 Bode plot of the left side moment-matching along the tangential direction l. The solid blue line, black dotted line and red dashed line represent the quantities for the FOM, ROM (model-based) and ROM_DD (data-driven), respectively. 79

4.7 Bode plot of the FOM and ROMs. The solid blue line, black dotted line and red dashed line represent the FOM, ROM (model-based) and ROM_DD (data-driven), respectively. 79

4.8 The layout of the combined system. 81

4.9 Bode plot of the right side moment-matching along the tangential direction l. The solid blue line, black dotted line and red dashed line represent the quantities for the FOM, ROM (model-based) and ROM_DD (data-driven), respectively. 83

4.10 Bode plot of the left side moment-matching along the tangential direction r. The solid blue line, black dotted line and red dashed line represent the quantities for the FOM, ROM (model-based) and ROM_DD (data-driven), respectively. 84

4.11 Bode plot of the FOM and ROMs. The solid blue line, black dotted line and red dashed line represent the FOM, ROM (model-based) and ROM_DD (data-driven), respectively. 84

4.12 Magnitude plots of the reduced-order models under 20 realizations of additive Gaussian noise. The red regions, blue regions and brown dashed lines refer to the estimation with 1000 measurements (Algorithm 1, $\widetilde{\nu} = 1000$), estimation with 30 measurements (Algorithm 1, $\widetilde{\nu} = 30$) and the ideal estimation (no noise), respectively. 86

4.13 Magnitude plots of the reduced-order models under 20 realizations of additive Gaussian noise. The red regions, blue regions and brown dashed lines refer to the robust algorithm (Algorithm 2), non-robust method (Theorem 4.2) and the ideal estimation (no noise), respectively. 86

4.14 Magnitude plots of the reduced-order models under 20 realizations of additive Gaussian noise. The red regions, blue regions and brown dashed lines refer to the estimation with 1000 measurements (Algorithm 1, $\widetilde{\nu} = 1000$), estimation with 30 measurements (Algorithm 1, $\widetilde{\nu} = 30$) and the ideal estimation (no noise), respectively. 87

4.15 Magnitude plots of the reduced-order models under 20 realizations of additive Gaussian noise. The red regions, blue regions and brown dashed lines refer to the robust algorithm (Algorithm 2), non-robust method (Theorem 4.2) and the ideal estimation (no noise), respectively. 87

4.16 Eigenvalues of the FOM and ROM_DD (data-driven), represented by the blue stars and hollow red circles, respectively. 88

4.17 Top: PCC voltage of the FOM and ROM_DD (data-driven), represented by solid blue and dashed red lines, respectively. Bottom: corresponding relative error. 89

4.18 Top: PCC voltage of the FOM and ROM_DD (data-driven), represented by solid blue and dashed red lines, respectively. Bottom: corresponding relative error. 91

4.19 Top: PCC voltage of the FOM and ROM_DD (data-driven), represented by solid blue and dashed red lines, respectively. Bottom: corresponding relative error. 92

5.1 Top and middle: time histories of x (the state using u_d), ξ (the state of the dynamic extension), x^e (the state using u_e) and $\bar{x}$ (the state using u_l). Bottom: control inputs. 121

5.2 Attenuation regions $\bar{\Omega}_d$ (blue), $\bar{\Omega}_e$ (yellow) and $\bar{\Omega}_l$ (purple). 124

6.1 Time history of the state of the system x_t (green) and of the corresponding estimated states $\hat{x}_t^D$ (purple), $\hat{x}_t^I$ (yellow) and $\hat{x}_t^H$ (red and blue) for the scalar case of deterministic, idealistic and hybrid observers, respectively. 143

6.2 Time history of the estimation errors e_t^D (purple), e_t^I (yellow) and e_t^H (red and blue) for the scalar case of deterministic, idealistic and hybrid observers, respectively. The black dash line represents the error dynamics $\dot{e}_t = -L_1 C_a e_t$. 143

6.3 Time history of the state of the system x_t (green) and of the corresponding estimated states $\hat{x}_t^D$ (purple), $\hat{x}_t^I$ (yellow) and $\hat{x}_t^H$ (red and blue) for the scalar case of deterministic, idealistic and hybrid observers, respectively. 144

6.4 Time history of the estimation errors e_t^D (purple), e_t^I (yellow) and e_t^H (red and blue) for the scalar case of deterministic, idealistic and hybrid observers, respectively. The black dash line represents the error dynamics $\dot{e}_t = -L_1 C_a e_t$. 145

6.5 Time history of the state x_1 (green) and of the corresponding estimated state $\hat{x}_1^D$ (purple), $\hat{x}_1^I$ (yellow) and $\hat{x}_1^H$ (red and blue) for the general case of deterministic, idealistic and hybrid observers, respectively. 146

6.6 Time history of the estimation error e_1^D (purple), e_1^I (yellow) and e_1^H (red and blue) for the general case of deterministic, idealistic and hybrid observers, respectively. 147

6.7 Time history of the state x_2 (green) and of the corresponding estimated state $\hat{x}_2^D$ (purple), $\hat{x}_2^I$ (yellow) and $\hat{x}_2^H$ (red and blue) for the general case of deterministic, idealistic and hybrid observers, respectively. 147

6.8 Time history of the estimation error e_2^D (purple), e_2^I (yellow) and e_2^H (red and blue) for the general case of deterministic, idealistic and hybrid observers, respectively. 148

6.9 Time history of the state x_3 (green) and of the corresponding estimated state $\hat{x}_3^D$ (purple), $\hat{x}_3^I$ (yellow) and $\hat{x}_3^H$ (red and blue) for the general case of deterministic, idealistic and hybrid observers, respectively. 148

6.10 Time history of the estimation error e_3^D (purple), e_3^I (yellow) and e_3^H (red and blue) for the general case of deterministic, idealistic and hybrid observers, respectively. 149

A.1 The diagram of IEEE 14-bus system, indicating generators, loads positions and transmission lines. 154

List of Tables

4.1 Computational comparison 90

5.1 Ratios $J^r_{u_e}$ and $J^r_{u_l}$ for different η_1 and η_2. 122

5.2 Proportions ρ_{u_d}, ρ_{u_e} and ρ_{u_l} for different η_1 and η_2. 122

5.3 Ratios $J^r_{u_e}$ and $J^r_{u_l}$ for different x_0. 123

5.4 The sign of J_{u_d}, J_{u_e} and J_{u_l} for different η_1, η_2. 124

A.1 Bus parameters 155

A.2 Line parameters 155

List of Symbols

Roman symbols

A	Wind turbine swept surface
C	DC bus capacity
I_a	One-mass wind turbine aggregated inertia
K_{C_p}	Constant tip speed ratio speed control law coefficient
L_l	Inductance of the grid connection impedance
P	Generator pole pairs
Q_s	Generator stator reactive power
R	Wind turbine radius
V_{DC}	DC bus voltage
V_{bus}	Infinite bus voltage
c_p	Aerodynamic power coefficient
f	Electrical network frequency
f^r	Rated frequency
r_s	Resistance of a single phase of the stator windings
r_l	Resistance of the grid connection impedance
U_g^r	Rated collection grid voltage
U_w^r	Rated wind turbine output voltage
v_w	Wind speed

Greek symbols

Γ_m	Generator torque
Γ_t	Wind turbine torque
β	Pitch angle
λ_m	Flux linkage per rotating speed unit
ν	Gearbox multiplication ratio
ω_{mn}	Nominal generator speed
ω_m	Generator mechanical angular speed
ω_r	Generator electrical angular speed
ω_t	Wind turbine speed
ρ	Air density
τ	Time constant of the pitch angle controller
θ_m	Generator shaft angular position
θ_r	Generator rotor electric angle

Superscripts and Subscripts

$*$	Reference value
abc	Vector of abc components
qd	Vector of qd components
m	Variable related to the generator shaft
r	Variable related to the generator rotor
s	Variable related to the generator stator
t	Variable related to the turbine
z	Variable related to the grid connection point

List of Abbreviations

AC	alternating current
ADI	Alternating Direction Implicit
DC	direct current
FOM	full-order model
GHJB	Generalized-Hamilton-Jacobi-Bellman
HJB	Hamilton-Jacobi-Bellman
IRKA	Iterative Rational Krylov Algorithm
LQR	linear quadratic regulator
MIMO	multiple-input multiple-output
MOR	model order reduction
PCC	point of common coupling
PDE	partial differential equation
PMSG	permanent magnet synchronous generator
POD	proper orthogonal decomposition
RK	Rational Krylov
ROM	reduced-order model
SDRE	state-dependent Riccati equation
SISO	single-input single-output
SNR	signal-noise-ratio
SVD	singular value decomposition
WFT	wind farm transformer
WTG	wind turbine generator

Chapter 1

Introduction

1.1 Background and Motivation

Dynamical systems have been widely exploited in many fields of research. The main feature of a *dynamical system* is that the variation of some quantities over time relies on other quantities. An essential class of dynamical systems is the linear systems, usually represented by

$$\begin{aligned} \dot{x}(t) &= Ax(t) + Bu(t), \\ y &= Cx(t), \end{aligned} \tag{1.1}$$

where $u(t)$ is the *input*, $y(t)$ is the *output*, $x(t)$ is the *state*, A, B and C are constant system matrices. By "*linear system*", we mean that the input-to-state and state-to-output relations described by the matrices are linear. While many theoretical tools effectively deal with linear systems (which are not large-scale), the rest of the dynamical systems remain complex and classified as nonlinear systems. By "*nonlinear system*", we refer to systems including nonlinear mathematical relations, which can be represented by

$$\begin{aligned} \dot{x}(t) &= f(x(t), u(t)), \\ y &= h(x(t)), \end{aligned} \tag{1.2}$$

where f and h are nonlinear mappings. A large amount of research focuses on this class of systems to understand their nonlinear system behavior.

Another very important classification of dynamical systems is the *stochastic systems*. The dynamics of this class of systems contain stochastic processes, known as the diffusion term. For instance, typical linear stochastic systems are usually represented by

$$dx(t) = [Ax(t) + Bu(t)]dt + [Cx(t) + Du(t)]d\mathcal{W}_t, \tag{1.3}$$

while nonlinear stochastic systems can be represented by

$$dx(t) = [f(x(t)) + g(u(t))]dt + [h(x(t)) + l(u(t))]d\mathcal{W}_t, \tag{1.4}$$

where A, B, C and D are constant system matrices, f, g, h and l are nonlinear mappings and $\mathcal{W}_t$ represents the Brownian motion. The *Brownian motion*, also known as the *Wiener process*, is everywhere continuous but not differentiable. Therefore, the study of stochastic differential equations is usually complex.

The present thesis focuses on complex dynamical systems. By "*complex*" we refer to the classes of dynamical systems that are at least large-scale, or nonlinear, or stochastic. The thesis aims to give insights into fundamental problems that arose in the study of complex dynamical systems, namely approximation, control and observation. These three topics cover almost all problems regarding dynamical systems. For the analysis of any dynamical system, the first key step is to find a mathematical representation. This consists of determining the mathematical equations and related parameters, usually known as modeling. In this thesis, we consider the problem of *approximation* instead of modeling, motivated by the fact that an approximate but simpler representation is required when considering complex dynamical systems. The problem of *control* is to design control inputs to obtain some system behavior, *e.g.* asymptotic stability. Many control problems consider the state-feedback, relying on the full information of system states (while the rest consider the output-feedback which is restricted by the mapping

between the outputs and states). Therefore, the problem of *observation* is to estimate the system states, which are not always measurable in practice. All these three topics together describe a clear flowchart for the control of dynamical systems, *i.e.* determining an approximate mathematical representation of the system, then constructing a state observer if needed and finally designing a control input for the required system behavior.

This thesis studies the topics of approximation, control and observation of complex dynamical systems. In particular, the model order reduction of large-scale systems and its application in wind farms, classes of control problems of nonlinear stochastic systems and the observer design of linear stochastic systems.

1.2 Thesis Outline

The thesis is divided into three parts, covering the topics of approximation, control and observation, respectively. Each part consists of several chapters and each chapter contains its own introduction, problem statement, theoretical results and examples.

Part I consists of 3 chapters and covers the topic of **approximation**. **Chapter 2** reviews the model order reduction of SISO systems by the moment-matching approach. **Chapter 3** provides the wind farm model used in Part 1. **Chapter 4** proposes a data-driven method for the model order reduction of large-scale wind farms.

Part II consists of 1 chapter and covers the topic of **control**. **Chapter 5** deals with three control problems for stochastic nonlinear systems: the infinite-horizon optimal control problem, the H_∞ control problem and the min-max zero-sum two-player game.

Part III consists of 1 chapter and covers the topic of **observation**. **Chapter 6** presents a hybrid observer for linear stochastic systems.

Finally, a summary of the contributions and future work are given in **Chapter 7**

1.3 Notation

Standard notation is used throughout the Thesis. The new notation that is not introduced in this section, is defined in the relevant sections of the Thesis.

The symbol $\mathbb{Z}$ denotes the set of integer numbers. The symbol $\mathbb{R}$ denotes the fields of real numbers. The symbol $\mathbb{C}$ denotes the fields of complex numbers. The symbols $\mathbb{C}_0$ and $\mathbb{C}_{<0}$ denote the fields of complex numbers with zero real part and strictly negative real part, respectively.

The symbol I denotes the identity matrix. The symbol $0_{m\times n}$ denotes the $m \times n$ zero matrix. $\sigma(A)$ is the spectrum of the matrix $A \in \mathbb{R}^{n\times n}$. $A^\top$ is the transpose of the matrix A. $A^\dagger$ is the Moore-Penrose pseudo-inverse of A. The vectorization of a matrix $A \in \mathbb{R}^{n\times m}$ is a $nm \times 1$ vector denoted by $\mathrm{vec}\,(A)$, namely $\mathrm{vec}\,(A) = [a_1^\top, a_2^\top, \cdots, a_n^\top]^\top$ where $a_i \in \mathbb{R}^n$ are the columns of A. The symbol $\|\cdot\|$ denotes the induced Euclidean matrix norm and $\delta_0(t)$ denotes the delta-Dirac impulse. The symbol e_j denotes the j-th vector of the standard basis, namely $e_j = [\underbrace{0 \cdots 0, 1}_{j}, 0 \cdots 0]^\top$.

The symbol $\mathcal{W}_t$ denotes a standard Wiener process. The symbol E denotes the expected value operator. $(\nabla, \mathcal{A}, \mathcal{P})$ is a probability space with a given set ∇, a σ-algebra $\mathcal{A}$ on ∇ and a probability measure $\mathcal{P}$ on the measurable space $(\nabla, \mathcal{A})$. A stochastic process with state space $\mathbb{R}^n$ is a family $\{x_t,\, t \in \mathbb{R}\}$ of $\mathbb{R}^n$-valued random variables, namely for every fixed $t \in \mathbb{R}$, $x_t(\cdot)$ is an $\mathbb{R}^n$-valued random variable and, for every fixed $\omega \in \nabla$, $x_\cdot(\omega)$ is an $\mathbb{R}^n$-valued function of time. For ease of notation, a stochastic process $\{x_t,\, t \in \mathbb{R}\}$ is simply denoted by x_t. Any subscript different from the symbol "t" indicates the corresponding component of the vector x_t, *e.g.* x_i is the i-th component of the vector x_t. $x(t; x_0, t_0)$ denotes the solution of a stochastic system with zero input and initial value x_0 at t_0. The solutions of the systems are intended in Itô sense.

1.4 Publication

The papers related to the specific topics of this thesis are summarised as follows.

- [1] **Z. Gong***, J. Mao, A. Junyent-Ferré, and G. Scarciotti, "Model Order Reduction of Large-Scale Wind Farms: A Data-Driven Approach", *IEEE Transactions on Power Systems*, accepted.

- [2] **Z. Gong***, T. Mylvaganam and G. Scarciotti, "Constructive Approximate Solutions to Classes of State-Feedback Control Problems for Stochastic Nonlinear Systems", *Automatica*, revision submitted.

- [3] **Z. Gong*** and G. Scarciotti, "A hybrid observer for practical observability of linear stochastic systems", in *Proceedings of the 61st IEEE Conference on Decision and Control (CDC)*, Cancún, 2022, pp. 1033–1038.

- [4] H. Zhang*, **Z. Gong**, A. Junyent-Ferré and G. Scarciotti, "A Benchmark Model for Model Order Reduction: Large-scale Wind Farms", in *Proceedings of the 11th Vienna International Conference on Mathematical Modelling (MATHMOD)*, Vienna, 2025, accepted.

Another paper on pandemic modelling was published at the beginning of the PhD, but this work is not included in the thesis as the pandemic model is not complex.

- [5] A. Mellone, **Z. Gong*** and G. Scarciotti, "Modelling, prediction and design of COVID-19 lockdowns by stringency and duration", *Scientific Reports*, vol. 11, no. 1, p. 15708, 2021.

Part I

Approximation

Chapter 2

Preliminary: Model Order Reduction by moment matching for SISO Systems

2.1 Introduction

Mathematical models are commonly used in engineering and science to describe a physical or artificial process. These mathematical models are fundamental for simulations and control design. Nowadays, as the need for more precise models increases, the complexity of models has increased significantly. For instance, an accurate mathematical description of fluid dynamics requires a large-scale system, involving millions of state variables. The simulation of large-scale systems is often time-consuming or infeasible due to the limited computational power [6]. While waiting for more advanced computational power, another solution for this problem is to represent the model in a reduced form, also known as *model order reduction*. The problem of model order reduction is finding a simplified mathematical description of the full dynamical systems, preserving the main properties (*e.g.* input-output relationship or stability). For linear systems, this problem has been addressed by two families of techniques. One is the singular

value decomposition (SVD)-based method and another is the Krylov subspace-based or moment-matching method. The former includes the balanced truncation [7–13] and the use of Hankel-norm [14–20], while the latter includes the projections and interpolations [21–30]. A detailed summary of these methods is given by [6]. While the linear systems can be readily reduced, more developed techniques are required for the nonlinear systems. Proper orthogonal decomposition (POD)-based methods have been presented in [31–36]. Some energy-based methods have been introduced in [37–40]. Finally, for the analysis of fluid and mechanical dynamics, the model order reduction of some specific nonlinear systems, such as quadratic-bilinear systems and Hamiltonian systems are studied in [41–47].

In the rest of the chapter, we briefly recall the moment-matching method proposed in [48, 49]. A thorough review of this method can be found in [50]. In Section 2.2, we introduce the notion of the moment and the moment-matching method for linear systems. We validate this method on a benchmark linear system. In Section 2.3, we move to nonlinear systems, providing an extended notion of the moment. Some results on the model order reduction of nonlinear systems are provided. The purpose of this chapter is to recall the model order reduction techniques for single-input, single-output (SISO) linear and nonlinear systems based on moment-matching, which is fundamental for the development of our method for multiple-input, multiple-output (MIMO) systems in Chapter 4.

2.2 Model order reduction by moment-matching for linear systems

In this section, we briefly recall the model order reduction by moment-matching for linear systems. We first recall the notion of the moment for linear systems, then the model-based and data-driven methods, and finally provide an illustrative example.

2.2.1 Moment of linear systems

This section briefly recalls the notion of the moment and the so-called "moment-matching" techniques for the model order reduction introduced in [48]. Let us consider a linear, single-input, single-output (SISO), continuous-time system

$$\dot{x} = Ax + Bu, \qquad y = Cx, \tag{2.1}$$

where $x(t) \in \mathbb{R}^n$ is the state, $u(t) \in \mathbb{R}$ is the input, $y(t) \in \mathbb{R}$ is the output, $A \in \mathbb{R}^{n\times n}$, $B \in \mathbb{R}^{n\times 1}$, $C \in \mathbb{R}^{1\times n}$ are the system matrices. Without loss of generality, system (2.1) is assumed to be minimal, *i.e.* controllable and observable. Let

$$W(s) = C(sI - A)^{-1}B,$$

be the associated transfer function of system (2.1). We are now ready to introduce the definition of moment.

Definition 2.1. Let $s_i \in \mathbb{C}\backslash\sigma(A)$. The *k-moment* of system (2.1) at s_i is a complex number $\eta_k(s_i) = \dfrac{(-1)^k}{k!}\left[\dfrac{d^k}{ds_i^k}W(s_i)\right]$, for $k \geq 0$ integer.

In particular the 0-*moment* of the system $\eta_0(s_i) = W(s_i)$, takes the value of the transfer function of system (2.1) at s_i. The quantities s_i are called interpolation points. The idea of model order reduction by moment-matching is to construct a reduced-order model with transfer function $\hat{W}(s)$ that, for ν interpolation points s_i, satisfies the following moment-matching condition, namely

$$\eta_k(s_i) = \hat{\eta}_k(s_i), \qquad \text{for } i = 1, ..., \nu. \tag{2.2}$$

The reduced-order model is matched with system (2.1) in terms of the transfer function (and the associated k-th derivatives) at all interpolation points s_i. This problem is readily solved by [48]

Lemma 2.1. [48] Consider system (2.1) and $s_i \in \mathbb{C}\backslash\sigma(A)$ for all $i = 1, \cdots, \eta$. The moments of the system, namely $\eta_0(s_1)$, ..., $\eta_{k_1-1}(s_1)$, ..., $\eta_0(s_\eta)$, ..., $\eta_{k_\eta-1}(s_\eta)$ are in one-to-one relation with the vector $C\Pi$, where the quantity Π is the unique solution of the Sylvester equation

$$A\Pi + BL = \Pi S. \tag{2.3}$$

with $S \in \mathbb{R}^{\nu\times\nu}$ be any matrix with characteristic and minimal polynomials $p(s) = \prod_{i=1}^{\eta}(s - s_i)^{k_i}$, where $\nu = \sum_{i=1}^{\eta} k_i$, and $L \in \mathbb{R}^{1\times\nu}$, any vector such that (S, L) is an observable pair.

Lemma 2.1 describes a one-to-one[1] relation between the moments and the vector $C\Pi$. The main contribution of this lemma is to further establish a one-to-one relation between the moments and the steady-state response through the Sylvester equation. This result is summarized in Theorem 2.1.

Theorem 2.1. [48] Consider system (2.1) with $\sigma(A) \subset \mathbb{C}_{<0}$ and $s_i \in \mathbb{C}\backslash\sigma(A)$ for all $i = 1, \cdots, \eta$. Let $S \in \mathbb{R}^{\nu\times\nu}$ be any matrix with characteristic and minimal polynomials $p(s) = \prod_{i=1}^{\eta}(s - s_i)^{k_i}$, where $\nu = \sum_{i=1}^{\eta} k_i$. Consider the interconnection of system (2.1) with the system

$$\dot{\omega} = S\omega, \qquad u = L\omega, \tag{2.4}$$

for any L and the initial condition $\omega(0)$ such that the triple $(L, S, \omega(0))$ is minimal. Then, the moments of the system, namely $\eta_0(s_1)$, ..., $\eta_{k_1-1}(s_1)$, ..., $\eta_0(s_\eta)$, ..., $\eta_{k_\eta-1}(s_\eta)$ are in one-to-one[2] relation with the steady-state response of the output y of the interconnected system given by Fig.2.1.

An input signal u is produced by (2.4) and then fed into (2.1). In the rest of the section by signal generator, we mean (2.4). The steady-state response of the output y can be

[1]The moments are fixed by matrices A, B, C and the zeros of $p(s)$. Given any observable pair (L, S) with S its characteristic and minimal polynomials coincide, there exists an invertible matrix $T \in \mathbb{C}^{\nu\times\nu}$ such that the vector $C\Pi T^{-1}$ is a collection of all ν moments. See [48, Lemma 3].

[2]The moments are uniquely determined by the steady-state response of $y(t)$ and *vice versa*.

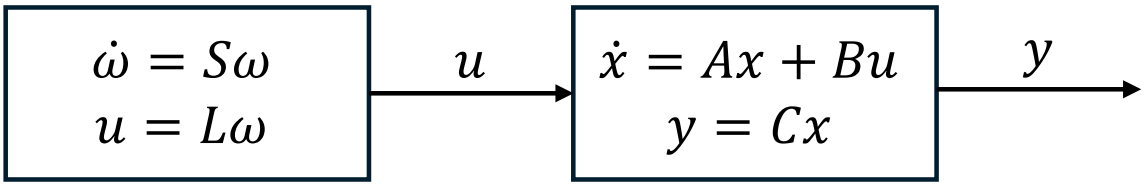

Figure 2.1: The diagram of the interconnected system in Theorem 2.1.

readily computed. Consider the interconnected system in Fig.2.1, we have

$$\begin{aligned}\dot{\overbrace{x - \Pi\omega}} = \dot{x} - \Pi\dot{\omega} &= Ax + BL\omega - \Pi S\omega \\ &= A(x - \Pi\omega) + (A\Pi + BL - \Pi S)\omega \\ &= A(x - \Pi\omega),\end{aligned}$$

yielding the output response $y(t) = C(\Pi\omega(t) + e^{At}(x(0) - \Pi\omega(0))$. Note that system (2.1) is assumed to be stable, *i.e.* $\sigma(A) \in \mathbb{C}_{<0}$. Therefore, the steady-state response of the output is $y_{ss} = C\Pi\omega$. With the one-to-one relations described in Lemma 2.1 and Theorem 2.1, we are now ready to construct the reduced-order model satisfying the moment-matching condition (2.2).

Theorem 2.2. [48] Consider system (2.1) and the signal generator (2.4) with $\sigma(A) \cap \sigma(S) = \emptyset$. Then, the system

$$\dot{\xi} = F\xi + Gu, \qquad \psi = H\xi, \tag{2.5}$$

with $\xi(t) \in \mathbb{R}^\nu$, $F \in \mathbb{R}^{\nu\times\nu}$, $G \in \mathbb{R}^{\nu\times 1}$ and $H \in \mathbb{R}^{1\times\nu}$ achieves the moment-matching with (2.1) at all interpolation points s_i encode by S if there exists a unique solution P of the equation

$$FP + GL = PS, \tag{2.6}$$

such that

$$HP = C\Pi, \tag{2.7}$$

where Π is the unique solution of (2.3).

Finally, as shown in [48], a family of systems

$$\dot{\xi} = (S - GL)\xi + Gu, \qquad \psi = C\Pi\xi, \tag{2.8}$$

with $\nu < n$ is a family of reduced-order models, matching the moments of (2.1) at all interpolation points s_i encoded by S, for any $G \in \mathbb{R}^{\nu\times 1}$ such that $\sigma(S) \cap \sigma(S - GL) = \emptyset$. Now, we conclude this section with a series of remarks.

Remark 2.1. G is a free parameter that can be selected to satisfy additional properties, *e.g.* the specific poles ensuring the asymptotic stability of the reduced-order model.

Remark 2.2. By Lemma 2.1, a one-to-one relation is established between the moments and the vector $C\Pi$ [HP] through the Sylvester equation (2.3) [(2.6)]. Theorem 2.2 is a direct result of matching the moments.

Remark 2.3. With the expression "exists a unique solution P" we mean that for assigned fixed matrices F, G, L and S, a unique solution P is decided by (2.6). This is guaranteed if $\sigma(F) \cap \sigma(S) = \emptyset$. The family of reduced-order models is not unique.

Remark 2.4. The family of reduced-order models (2.8) is obtained by selecting the solution as $P = I$, avoiding solving equation (2.6). This selection results in $F = S - GL$ and $H = C\Pi$. Therefore, the free parameter G is selected such that $\sigma(S) \cap \sigma(S - GL) = \emptyset$ to ensure the solution $P = I$ is unique.

Remark 2.5. It is observed that to construct a family of reduced-order models, only the quantity $C\Pi$ is required. By Theorem 2.2, it is possible to construct a reduced-order model using the time series of the output of the interconnected system. This is summarized as a data-driven method in the next section.

2.2.2 Data-driven method

With the analysis in Theorem 2.1, we have the steady-state response of the interconnected system $y_{ss} = C\Pi\omega$, where y is a measurable output and ω can be computed directly.

As presented in [49], it is possible to construct an approximation of $C\Pi$ using the input-output data only. The result is summarised as follows.

Theorem 2.3. [49] Consider the interconnection of system (2.1) and the signal generator (2.4). Assume $\sigma(A) \subset \mathbb{C}_{<0}$, $\sigma(S) \subset \mathbb{C}_0$, S has simple eigenvalues and the triple $(L, S, \omega(0))$ is minimal. For $\widetilde{\nu} \geq \nu$, define the time-snapshots $\widetilde{R}_k \in \mathbb{R}^{\widetilde{\nu}\times\nu}$ and $\widetilde{E}_k \in \mathbb{R}^{\widetilde{\nu}}$ as

$$\widetilde{R}_k = [\omega(t_{k-\widetilde{\nu}+1}) \cdots \omega(t_{k-1})\ \omega(t_k)]^\top,$$
$$\widetilde{E}_k = [y(t_{k-\widetilde{\nu}}+1) \cdots y(t_{k-1})\ y(t_k)]^\top,$$

Then,

$$\operatorname{vec}\left(\widetilde{C\Pi}_k\right) = (\widetilde{R}_k^\top \widetilde{R}_k)^{-1} \widetilde{R}_k^\top \widetilde{E}_k. \tag{2.9}$$

is an *online estimate* of $C\Pi$, namely there exists a sequence $\{t_k\}$ such that $\widetilde{R}_k^\top \widetilde{R}_k$ is full rank and $\lim_{k\to\infty} \widetilde{C\Pi}_k = C\Pi$.

The formula (2.9) is a classic least-square estimation of $C\Pi$ based on the steady-state response of the output y. Therefore, the time sequence $\{t_k\}$ is selected such that $t_k \to \infty$ as $k \to \infty$ and can be truncated at a sufficiently large k for practical estimation. Note that the unique solution Π is not required explicitly in a reduced-order model. Given with an estimation of $C\Pi$, we can construct a reduced-order model without using the knowledge of the full-order model (*i.e.* the system matrices A, B and C).

2.2.3 Example: Building model

To give an insight into understanding the model order reduction by moment-matching, let us consider a building model given in [51, 52], with 1 input, 1 output and 48 states. This building model is commonly used as a benchmark model for the validation of model order reduction in many references, *e.g.* [49, 53].

In this example, the interpolation points are selected as 0, $\pm 5.22\iota$, $\pm 10.3\iota$, $\pm 13.5\iota$, $\pm 22.2\iota$, $\pm 24.5\iota$, $\pm 34.5\iota$, $\pm 44.5\iota$, $\pm 55.9\iota$ and $\pm 70\iota$, resulting in a reduced-order model

of order $\nu = 19$. Fig. 2.2 compares the bode plot of the full-order model (FOM) and reduced-order models (ROMs). In particular, the blue solid lines represent the FOM, the black dotted lines represent the model-based ROM, the dashed red lines represent the data-driven ROM and the cyan diamonds represent the selected interpolation points. The performance of the FOM is fully recovered by the ROMs.

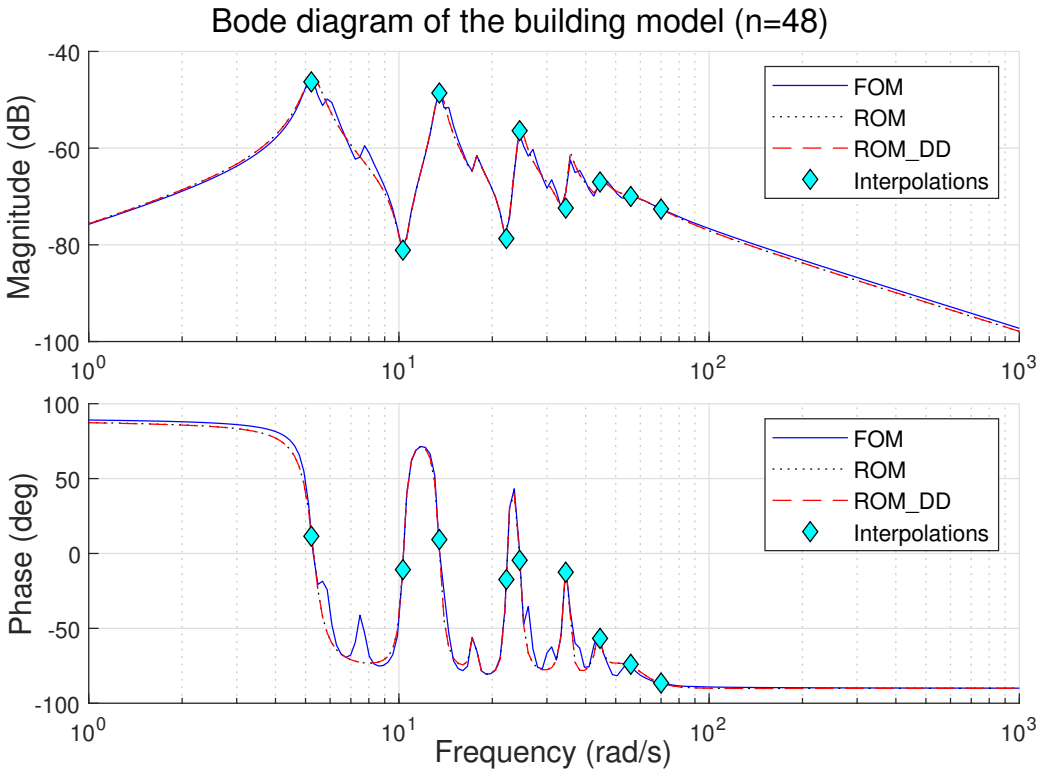

Figure 2.2: Bode plot of the FOM and ROMs. The solid blue line, black dotted line and red dashed line represent the FOM, ROM (model-based) and ROM_DD (data-driven), respectively. The cyan diamonds indicate the selected interpolation points.

2.3 Model order reduction by moment-matching for nonlinear systems

This section briefly recalls the model order reduction by moment-matching for nonlinear systems. We first recall the notion of the moment for nonlinear systems, then the data-driven method, and finally provide an illustrative example.

2.3.1 Moment of nonlinear systems

The notion of the moment can be extended to nonlinear systems, as presented in [48]. Let us consider a nonlinear, single-input, single-output, continuous-time system

$$\dot{x} = f(x, u), \quad y = h(x), \tag{2.10}$$

where $x(t) \in \mathbb{R}^n$ is the state, $u(t) \in \mathbb{R}$ is the input, $y(t) \in \mathbb{R}$ is the output, f and h are smooth mappings. Similar to the linear case, we introduce a signal generator described by the equations

$$\dot{\omega} = s(\omega), \quad u = l(\omega), \tag{2.11}$$

with $\omega(t) \in \mathbb{R}^\nu$, $u(t) \in \mathbb{R}$, s and l are smooth mappings. Furthermore, suppose that $f(0,0) = 0$, $s(0) = 0$, $l(0) = 0$ and $h(0) = 0$ and the following two assumptions hold.

Assumption 2.1. The signal generator (2.11) is observable[3] and Poisson stable[4] with $\omega(0) \neq 0$.

Assumption 2.2. The zero equilibrium of system (2.10) is locally exponentially stable.

With these two assumptions, the steady-state response of the interconnected system of (2.10) and (2.11) is described as follows.

Theorem 2.4. [54] Consider system (2.10) and the signal generator (2.11). Suppose that Assumption 2.1 and 2.2 hold. Then there exists a mapping π, locally defined in a neighbourhood of $\omega = 0$, solves the partial differential equation

$$\frac{\partial \pi}{\partial \omega} s(\omega) = f(\pi(\omega), l(\omega)). \tag{2.12}$$

Furthermore, the steady-state response of the interconnected system in Fig. 2.3 is $h(\pi(\omega))$ for any $x(0)$ and $\omega(0)$ sufficiently small, namely for all $x(0)$ and $\omega(0)$ the corresponding solution $x(t)$, $\omega(t)$ fulfills, $\lim_{t\to\infty}[h(\pi(\omega(t))) - h(x(t))] = 0$

[3]For any pair of initial conditions $\omega_a(0)$ and $\omega_b(0)$, such that $\omega_a(0) \neq \omega_b(0)$, the corresponding output trajectories $l(\omega_a(t))$ and $l(\omega_b(t))$ are such that $l(\omega_a(t)) - l(\omega_b(t)) \not\equiv 0$.

[4]See [54, Chapter 8] for the definition of Poisson stability.

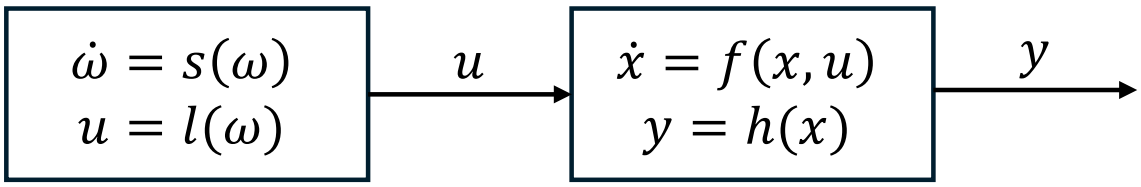

Figure 2.3: The diagram of the interconnected system in Theorem 2.4.

By Theorem 2.4, we define the moment for nonlinear systems and establish the relation between the moment and the steady-state response of the interconnected system.

Definition 2.2. Consider system (2.10) and the signal generator (2.11). Suppose Assumption 2.1 hold. The mapping $h \circ \pi$ is the moment of system (2.10) at (s, l).

Remark 2.6. The moment $h \circ \pi$ computed along a particular trajectory $\omega(t)$ coincides with the steady-state response of the interconnected system.

Remark 2.7. The definition of the moment is consistent for linear and nonlinear systems. If (2.10) and (2.11) is linear (*i.e.* $f(x,u) = Ax + Bu$, $h(x) = Cx$ and $s(\omega) = S\omega$), then the partial differential equation (2.12) degenerates to the Sylvester equation (2.3). The results on linear systems are retrieved.

Finally, as presented in [48], a family of reduced order models of (2.10) at (s, l) is described as

$$\dot{\xi} = s(\xi) - \delta(\xi)l(\xi) + \delta(\xi)u, \quad \Psi = h(\pi(\xi)), \tag{2.13}$$

where δ is any mapping such that the equation

$$\frac{\partial p}{\partial \omega} s(\omega) = s(p(\omega)) - \delta(p(\omega))l(p(\omega)) + \delta(p(\omega))l(\omega), \tag{2.14}$$

has a unique solution $p(\omega) = \omega$.

Commonly, solving the partial differential equation (2.12) is difficult. Given some specific nonlinear mapping f, (2.12) can be solved approximately [44]. However, for general nonlinear systems that allow various mapping f, the model-based method is considered restricted. By the relation between the moment and the steady-state

response of the interconnected system, a data-driven method has been proposed in [49], computing the moment $h \circ \pi$ at (s, l) without using any knowledge of the system, *i.e.* the mapping f and h. We summarise this method in the next section.

2.3.2 Data-driven method

The data-driven method is based on a standard assumption that the mapping $h \circ \pi$ can be approximated by a family of basis functions.

Assumption 2.3. The mapping $h \circ \pi$ belongs to the function space identified by a family of continuous basis functions $\varphi_i : \mathbb{R}^\nu \to \mathbb{R}$, for $i = 1, \cdots, M$ (M can be $+\infty$). There exist coefficients $\gamma_i \in \mathbb{R}$, for $i = 1, \cdots, M$, such that $h(\pi(\omega)) = \sum_{i=1}^{M} \gamma_i \varphi_i(\omega)$ for any ω.

Define the vector of the basis functions φ_i and corresponding coefficients γ_i as follows.

$$\Omega(\omega) = [\varphi_1(\omega), \varphi_2(\omega), \cdots, \varphi_N(\omega)],$$
$$\Gamma = [\gamma_1, \gamma_2, \cdots, \gamma_N],$$

with $N \leq M$. Then, the mapping $h \circ \pi$ can be approximated by terminating at N. The vector $\Omega(\omega)$ contains all selected basis functions while the vector Γ contains the corresponding coefficients. Practically, selecting the basis functions is a trial and error procedure, commonly starting with the polynomial expansion or functions of the same class as the ones generated by the signal generator.

Recall Theorem 2.4, an approximation of the steady-state response of the interconnected system is given by

$$y_{ss} = h(\pi(\omega)) \approx \sum_{i=1}^{N} \gamma_i \varphi_i(\omega) = \Gamma \Omega(\omega), \tag{2.15}$$

which indicates that an approximation of Γ can be computed as follows.

Theorem 2.5. [49] Suppose that Assumption 2.1− 2.3 hold. Define the time-snapshots $\widetilde{U}_k \in \mathbb{R}^{\widetilde{\nu}\times N}$ and $\widetilde{\Upsilon}_k \in \mathbb{R}^{\widetilde{\nu}}$ with $\widetilde{\nu} \geq \nu$ as

$$\begin{aligned} \widetilde{U}_k &= [\Omega(\omega(t_{k-\widetilde{\nu}+1})), \cdots, \Omega(\omega(t_k))]^\top, \\ \widetilde{\Upsilon}_k &= [y(t_{k-\widetilde{\nu}+1}), \cdots, y(t_k)]^\top. \end{aligned} \tag{2.16}$$

If $\widetilde{U}_k$ is full column rank, then

$$\mathrm{vec}\left(\widetilde{\Gamma}_k\right) = (\widetilde{U}_k^\top \widetilde{U}_k)^{-1} \widetilde{U}_k^\top \widetilde{\Upsilon}_k \tag{2.17}$$

is an *online estimate* of Γ, namely there exists a sequence $\{t_k\}$ such that $\lim_{k\to\infty} \widetilde{\Gamma}_k = \Gamma$.

Remark 2.8. By Theorem 2.5, the mapping $h \circ \pi$ is approximated using the input-output data of the interconnected system only, without solving (2.12).

Remark 2.9. Note that the moment is computed along a particular trajectory $\omega(t)$. Unlike linear systems, where the local properties are also global, it is important to consider multiple trajectories for nonlinear systems. To this end, the experiments for data collection are commonly repeated with various initial conditions $\omega(0)$. Namely, define the new time-snapshots of M trajectories as

$$\begin{aligned} U^* &= [\widetilde{U}_k^{1\top}, \widetilde{U}_k^{2\top}, \cdots, \widetilde{U}_k^{M\top}]^\top, \\ \Upsilon^* &= [\widetilde{\Upsilon}_k^{1\top}, \widetilde{\Upsilon}_k^{2\top}, \cdots, \widetilde{\Upsilon}_k^{M\top}]^\top, \end{aligned} \tag{2.18}$$

where $\widetilde{U}_k^{i\top}$ and $\widetilde{\Upsilon}_k^{i\top}$ are defined as in (2.16), considering the i-th trajectory starting from the i-th initial condition $\omega(0) = \omega_0^i$. Then, the new coefficient vector Γ^* is computed by (2.17) using new time-snapshots U^* and Υ^*.

Remark 2.10. The selection of the basis functions is important for the approximation. A comparison of different families of basis functions is given in the next section.

Remark 2.11. Note that this method has been further improved in [55] to match linear and nonlinear moments simultaneously.

2.3.3 Example: Burgers' equation

The viscous Burgers' equation describing the fluid dynamics is commonly considered a benchmark model for the validation of nonlinear model order reduction [56]. Let us consider a one-dimensional Burgers' equation

$$\begin{aligned} v_t + vv_x &= \nu v_{xx}, \quad && (0,1)\times(0,T), \\ \alpha v(0,t) + \beta x(0,t) &= u(t), && t \in (0,T), \\ v_x(1,t) &= 0, && t \in (0,T), \\ v(x,0) &= v_0(x), && x \in (0,1), \end{aligned} \tag{2.19}$$

with the parameters $\alpha = 1$, $\beta = 0$, $\nu = 0.1$ and the initial condition $v_0(x) = 1$. The discretization of this Burgers' equation leads to a n-th order quadratic-bilinear system

$$\begin{aligned} \dot{x} &= Ax + H(x \otimes x) + Nxu + Bu, \\ y &= Cx, \end{aligned} \tag{2.20}$$

where $A \in \mathbb{R}^{n\times n}$, $H \in \mathbb{R}^{n\times n^2}$, $N \in \mathbb{R}^{n\times n}$, $B \in \mathbb{R}^{n\times 1}$ and $C \in \mathbb{R}^{1\times n}$.

In this example, we consider a discretization of 100 steps results in a quadratic-bilinear system of order $n = 100$. The interpolation points are selected as $\pm 5\iota$, $\pm 10\iota$, $\pm 15\iota$ and $\pm 20\iota$, leading to a reduced-order model of order 8. The basis functions are selected as a polynomial surface. We consider three sets of basis functions, namely

$$\begin{aligned} \Omega_1 &= [\omega_1, \cdots, \omega_8]^\top, \\ \Omega_2 &= [\Omega_1^\top, \omega_1^2, \omega_1\omega_2, \cdots, \omega_8^2]^\top, \\ \Omega_3 &= [\Omega_2^\top, \omega_1^3, \omega_1^2\omega_2, \cdots, \omega_8^3]^\top, \end{aligned}$$

where $\omega_1, \cdots, \omega_8$ are the corresponding components of ω.

Fig. 2.4 compares the output of the FOM and ROMs. In particular, the purple solid line represents the quantity related to the FOM. The blue, red and yellow lines represent

the quantity related to the ROMs with the sets of basis functions Ω_1, Ω_2 and Ω_3, respectively. It is observed that the approximation of the mapping is improved by involving the higher-order polynomials as basis functions. With the basis functions of Ω_3, the output error is negligible.

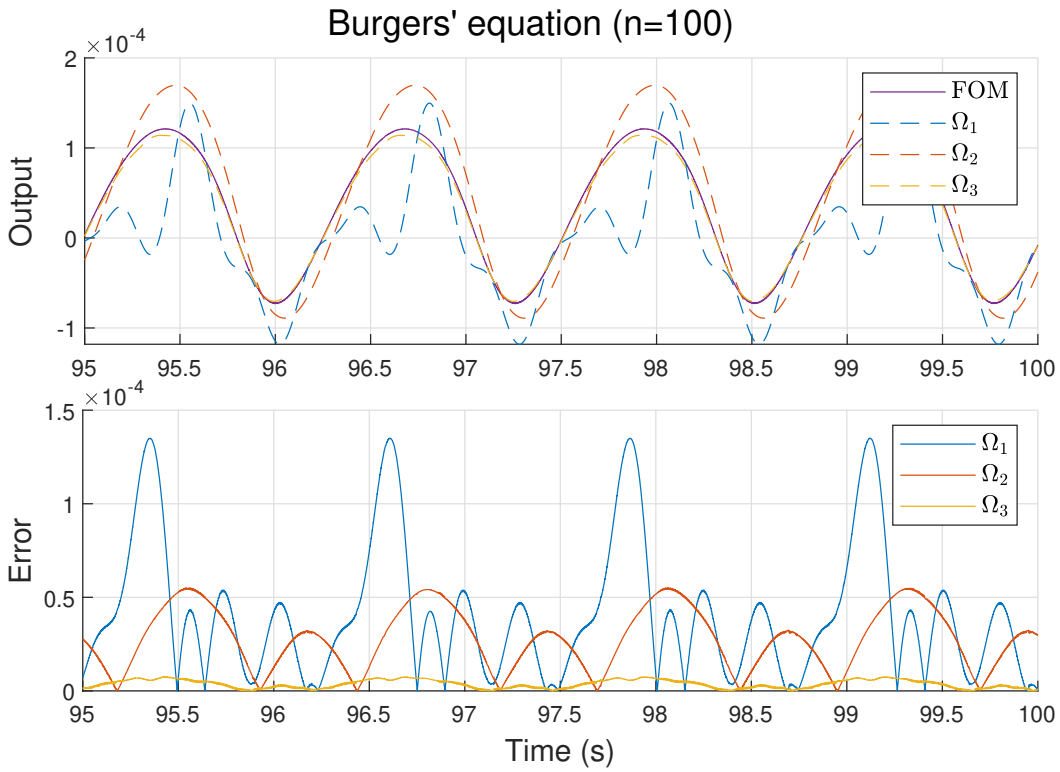

Figure 2.4: Top: output of the FOM and ROMs. The solid purple line represents the FOM. The blue, red and yellow dashed lines represent ROMs constructed by the sets of basis functions Ω_1, Ω_2 and Ω_3, respectively. Bottom: corresponding error.

2.4 Conclusion

In this chapter, we have reviewed the model order reduction by moment-matching for SISO systems. We have recalled the notion of the moment for linear and nonlinear systems and then have introduced the relation between the moment and the steady-state response. With this one-to-one relation, the data-driven methods have been recalled. Two examples of benchmark models have been given to illustrate and compare the model-based and data-driven methods. These results are fundamental for developing model order reduction techniques for MIMO systems in Chapter 4.

Chapter 3

Preliminary: Wind turbine generator model

A wind turbine generator commonly consists of mechanical and electrical systems. While the mechanical system extracts the kinetic energy of the wind by blades, the electrical system converts the supplied mechanical energy to the electrical energy by a rotor. In this chapter, we briefly recall the wind turbine model in [57].

3.1 Wind turbine mechanism

This section recalls the wind turbine mechanism, namely the wind turbine aerodynamics, pitch angle control, drivetrain dynamics and wind turbine speed control.

3.1.1 Wind turbine aerodynamics

A wind turbine extracts the kinetic power of the wind with a power coefficient C_p. The extracted power can be expressed by the kinetic power of the wind multiplied by the

power coefficient C_p, namely

$$P_t = C_p P_w = C_p \frac{1}{2} \rho A v_w^3, \tag{3.1}$$

where P_t is the power extracted by the wind turbine, P_w is the kinetic power supplied by the wind, ρ is the air density assumed to be constant, A is the surface covered by the wind wheel and v_w is the average wind speed.

The power coefficient C_p depends on the average speed of the wind crossed by, the angular speed of the turbine and the pitch angle of the blades. As in [58], an analytic expression of C_p is given by

$$\begin{aligned} C_p(\Lambda, \beta) &= c_1(c_2 \frac{1}{\Lambda} - c_3\beta - c_4\beta^{c_5} - c_6)e^{-c_7 \frac{1}{\Lambda}}, \\ \frac{1}{\Lambda} &= \frac{1}{\lambda + c_8\beta} - \frac{c_9}{1+\beta^3} \end{aligned} \tag{3.2}$$

where β is the blade pitch angle, ω_t is the turbine angular speed, R is the turbine radius and λ is the so-called tip speed ratio defined as $\lambda = \dfrac{\omega_t R}{v_w}$. $[c_1, \cdots, c_9]$ are the characteristic parameters of the wind turbine which can be obtained by the analysis of a real wind turbine or simulations through the finite element method.

Then, divide (3.1) by ω_t the turbine torque Γ_t is easily obtained as

$$\Gamma_t = \frac{1}{2} C_p \rho A v_w^3 \frac{1}{\omega_t}, \tag{3.3}$$

which is used to control the wind turbine speed in the next section.

3.1.2 Pitch angle control

The pitch angle control aims to optimize the power coefficient C_p given by (3.2). A pitch actuator commonly consists of mechanical and hydraulic systems. The actuator

dynamic is a typical first-order system, namely

$$\dot{\beta} = \frac{1}{\tau}(\beta^* - \beta), \tag{3.4}$$

with the transfer function

$$\beta(s) = \frac{1}{\tau s + 1}\beta^*(s), \tag{3.5}$$

where τ is the time constant depends on the pitch actuator and β^* is the reference value of the pitch angle β.

To achieve the pitch angle control, we apply a PI controller given by

$$\beta^*(s) = \frac{K_p s + K_i}{s}(\omega_m(s) - \omega_{mn}(s)), \tag{3.6}$$

with

$$\omega_m = \nu\omega_t, \tag{3.7}$$

where ν is the Gearbox multiplication ratio, ω_m is the mechanical angular speed, ω_{mn} is the nominal mechanical angular speed, K_p and K_i are proportion and integral gains of the PI controller.

3.1.3 Drivetrain dynamics

The drivetrain of a wind turbine generator is a mechanical system composed of the wind turbine, the turbine shaft, the gearbox and the rotor shaft. This mechanical system is commonly modeled as a series of masses connected through elastic couplings with the gearbox ratio, damping ratio and linear stiffness. A one-mass model of the drivetrain

can be expressed as

$$\begin{aligned}\omega_t(s) &= \frac{\nu}{(I_m\nu^2 + I_t)s}\Gamma_m(s) + \frac{1}{(I_m\nu^2 + I_t)s}\Gamma_t(s), \\ &= \frac{\nu}{I_a s}\Gamma_m(s) + \frac{1}{I_a s}\Gamma_t(s),\end{aligned} \tag{3.8}$$

where I_m is the inertia of the rotor and gearbox, I_t is the inertia of the turbine and $I_a \triangleq (I_m\nu^2 + I_t)$ is the aggregated inertia of the one-mass wind turbine.

3.1.4 Wind turbine speed control

In Section 3.1.1, we have shown that a wind turbine extracts the kinetic power from the wind. To maximize the power extraction, the turbine speed ω_t is controlled as different values for various wind speeds. However, the precise measurement of the wind speed is commonly unavailable. To this end, we consider the well-known maximum power point tracking (MPPT) strategy described in the literature [59–62], which maximizes energy extraction without the wind speed measurement. The most basic method of these MPPT techniques is the so-called *constant tip speed ratio control* [63,64] summarised as

$$\begin{aligned}K_{C_p} &= \frac{1}{2}\rho A R^3 \frac{c_1(c_2 + c_6c_7)^3 e^{-\frac{c_2+c_6c_7}{c_2}}}{c_2^2 c_7^4}, \\ \Gamma_m^{opt} &= \frac{1}{\nu}K_{C_p}\omega_t^2, \qquad \Gamma_m^* = \Gamma_m^{opt},\end{aligned} \tag{3.9}$$

where Γ_m^{opt} is the optimal generator torque and Γ_m^* is the generator torque reference value, which the generator control should achieve.

Then, provided with the generator torque and recall (3.8) in the time domain, the angular acceleration of the wind turbine is given by

$$\dot{\omega}_t = \frac{1}{I_a}(\Gamma_t + \nu\Gamma_m), \tag{3.10}$$

3.2 Generator dynamics

We consider the permanent magnet synchronous generator (PMSG). The main feature of PMSG is that the machine is completely isolated from the grid and therefore is less influenced by the grid-disturbance. The dynamic equation of a machine for PMSG is given by

$$v_s^{abc} = r_s i_s^{abc} + \frac{d}{dt}\lambda_s^{abc}, \tag{3.11}$$

where r_s is the single-phase resistance of the stator winding, v_s^{abc} is the three-phase stator voltage vector, i_s^{abc} is the three-phase stator current vector and λ_s^{abc} is the three-phase stator flux linkage vector.

In particular, if the inductance is considered a projection according to the rotor angle, then the stator flux linkage vector λ_s^{abc} can be expressed as

$$\lambda_s^{abc} = (L_1 + L_2(\theta_r))i_s^{abc} + \lambda_m \begin{bmatrix} \sin(\theta_r) \\ \sin(\theta_r - \frac{2\pi}{3}) \\ \sin(\theta_r + \frac{2\pi}{3}) \end{bmatrix}, \tag{3.12}$$

with the inductance independent on θ_r

$$L_1 = \begin{bmatrix} L_{ls} + L_A & -\frac{1}{2}L_A & -\frac{1}{2}L_A \\ -\frac{1}{2}L_A & L_{ls} + L_A & -\frac{1}{2}L_A \\ -\frac{1}{2}L_A & -\frac{1}{2}L_A & L_{ls} + L_A \end{bmatrix}, \tag{3.13}$$

and the inductance dependent on θ_r

$$L_2(\theta_r) = -L_B \begin{bmatrix} \cos(2\theta_r) & \cos(2\theta_r - \frac{2\pi}{3}) & \cos(2\theta_r + \frac{2\pi}{3}) \\ \cos(2\theta_r - \frac{2\pi}{3}) & \cos(2\theta_r + \frac{2\pi}{3}) & \cos(2\theta_r) \\ \cos(2\theta_r + \frac{2\pi}{3}) & \cos(2\theta_r) & \cos(2\theta_r - \frac{2\pi}{3}) \end{bmatrix}, \tag{3.14}$$

where θ_r is the rotor electric angle, λ_m is the flux linkage per rotating speed unit, L_{sl} is the stator leakage inductance, L_1 represents the inductance independent on the rotor

angle, $L_2(\theta_r)$ represents the inductance dependent on the rotor angle, L_A and L_B are constant inductance terms.

Now, substitute (3.12) into (3.11) yields

$$v_s^{abc} = (r_s I_3 + \omega_r \frac{d}{dt} L_2(\theta_r)) i_s^{abc} + (L_1 + L_2(\theta_r)) \frac{d}{dt} i_s^{abc} + \lambda_m \omega_r \begin{bmatrix} \cos(\theta_r) \\ \cos(\theta_r - \frac{2\pi}{3}) \\ \cos(\theta_r + \frac{2\pi}{3}) \end{bmatrix}. \quad (3.15)$$

The above equation is time-varying as θ_r changes over time. To overcome this, we introduce the *Park transformation* which changes variables from the *abc* framework to the *qd* framework (the zero component is omitted), namely

$$T(\theta) = \frac{2}{3} \begin{bmatrix} \cos(\theta) & \cos(\theta - \frac{2\pi}{3}) & \cos(\theta + \frac{2\pi}{3}) \\ \sin(\theta) & \sin(\theta - \frac{2\pi}{3}) & \sin(\theta + \frac{2\pi}{3}) \end{bmatrix}, \quad (3.16)$$

and the inverse Park transformation

$$T^{-1}(\theta) = \begin{bmatrix} \cos(\theta) & \sin(\theta) \\ \cos(\theta - \frac{2\pi}{3}) & \sin(\theta - \frac{2\pi}{3}) \\ \cos(\theta + \frac{2\pi}{3}) & \sin(\theta + \frac{2\pi}{3}) \end{bmatrix}, \quad (3.17)$$

where θ is the rotation angle of the Park transformation.

With Park transformation, the stator voltage, current and flux linkage vectors in *qd* and *abc* framework can be expressed as

$$\begin{aligned} v_s^{qd} &= T(\theta) v_s^{abc}, & v_s^{abc} &= T^{-1}(\theta) v_s^{qd}, \\ i_s^{qd} &= T(\theta) i_s^{abc}, & i_s^{abc} &= T^{-1}(\theta) i_s^{qd}, \\ \lambda_s^{qd} &= T(\theta) \lambda_s^{abc}, & \lambda_s^{abc} &= T^{-1}(\theta) \lambda_s^{qd}. \end{aligned} \quad (3.18)$$

Now, given with (3.16), (3.17) and (3.18), the equation (3.15) can be rewritten as

$$\begin{aligned} v_s^{qd} =& T(\theta)\cdot(r_s I_3 + \omega_r \frac{d}{dt} L_2(\theta_r))\cdot[T^{-1}(\theta) i_s^{qd}] + \lambda_m \omega_r \begin{bmatrix} \cos(\theta_r - \theta) \\ -\sin(\theta_r - \theta) \end{bmatrix} \\ &+ T(\theta)\cdot(L_1 + L_2(\theta_r))\frac{d}{dt}[T^{-1}(\theta) i_s^{qd}]. \end{aligned} \tag{3.19}$$

By selecting $\theta = \theta_r$ for the Park transformation, the generator equation (3.19) can be further simplified as a compact form

$$v_s^{qd} = \begin{bmatrix} r_s & \omega_r L_d \\ -\omega_r L_q & r_s \end{bmatrix} i_s^{qd} + \begin{bmatrix} L_q & 0 \\ 0 & L_d \end{bmatrix} \frac{d}{dt} i_s^{qd} + \lambda_m \omega_r \begin{bmatrix} 1 \\ 0 \end{bmatrix}, \tag{3.20}$$

with the new variables defined as

$$\begin{aligned} L_q &= L_{sl} + \frac{3}{2}(L_A - L_B), \\ L_d &= L_{sl} + \frac{3}{2}(L_A + L_B). \end{aligned} \tag{3.21}$$

Finally, by (3.20) the dynamics of the stator current in qd framework is obtained as

$$\frac{d}{dt} i_s^{qd} = \begin{bmatrix} -\frac{r_s}{L_q} & -\frac{\omega_r L_d}{L_q} \\ \frac{\omega_r L_q}{L_d} & -\frac{r_s}{L_d} \end{bmatrix} i_s^{qd} + \begin{bmatrix} \frac{1}{L_q} & 0 \\ 0 & \frac{1}{L_d} \end{bmatrix} v_s^{qd} - \lambda_m \omega_r \begin{bmatrix} \frac{1}{L_q} \\ 0 \end{bmatrix}. \tag{3.22}$$

To compute the generator torque in the qd framework, we again consider the park transformation to (3.12) with the rotation angle $\theta = \theta_r$, namely

$$\begin{aligned} \lambda_s^{qd} &= T(\theta)(L_1 + L_2(\theta_r))T^{-1}(\theta) i_s^{qd} + \lambda_m \begin{bmatrix} \sin(\theta_r - \theta) \\ \cos(\theta_r - \theta) \end{bmatrix}, \\ &= \begin{bmatrix} L_q & 0 \\ 0 & L_d \end{bmatrix} i^{qd} + \lambda_m \begin{bmatrix} 0 \\ 1 \end{bmatrix}. \end{aligned} \tag{3.23}$$

Given by (3.23), the generator torque Γ_m can be computed using the mechanical power divided by the mechanical angular speed ω_m, namely

$$\begin{aligned}\Gamma_m &= \frac{3}{2}\frac{\omega_r}{\omega_m}(\lambda_{sd}i_{sq} - \lambda_{sq}i_{sd}),\\ &= \frac{3}{2}P(\lambda_m i_{sq} + (L_d - L_q)i_{sq}i_{sd}),\end{aligned} \tag{3.24}$$

where $P = \dfrac{\omega_r}{\omega_m}$ is the number of pole pairs, $\lambda_s^{qd} = [\lambda_{sq}\ \lambda_{sd}]^\top$ and $i_s^{qd} = [i_{sq}\ i_{sd}]^\top$.

3.3 Generator vector control

The goal of the generator control is to drive the machine torque and the reactive power to the desired values. However, these quantities are difficult to measure. Therefore, a stator current control loop is applied with current reference values determined by the desired machine torque Γ_m^* and the stator reactive power Q_s^*, namely

$$i_{sq}^* = \frac{2}{3P}\frac{\Gamma_m^*}{\lambda_m}, \qquad i_{sd}^* = \frac{2}{3P}\frac{Q_s^*}{\omega_m\lambda_m}. \tag{3.25}$$

We note that in (3.20) the q and d variables are coupled. To this end, the following feedback decoupling loop is considered.

$$v_s^{qd} = \hat{v}_s^{qd} + \begin{bmatrix} 0 & \omega_r L_d \\ -\omega_r L_q & 0 \end{bmatrix} i_s^{qd} + \lambda_m\omega_r \begin{bmatrix} 1 \\ 0 \end{bmatrix}. \tag{3.26}$$

where $\hat{v}_s^{qd} = [\hat{v}_{sq}, \hat{v}_{sd}]^{\mathrm{T}}$ represents the outputs of the current controllers. Assuming the decoupling is perfect, then the generator dynamics can be rewritten as

$$\hat{v}_s^{qd} = \begin{bmatrix} r_s & 0 \\ 0 & r_s \end{bmatrix} i_s^{qd} + \begin{bmatrix} L_q & 0 \\ 0 & L_d \end{bmatrix} \frac{d}{dt} i_s^{qd}. \tag{3.27}$$

Now, these equations can be split as two decoupled systems for q and d. Applying the Laplace transform to the above equations results in

$$\frac{i_{sq}}{\hat{v}_{sq}}(s) = \frac{1}{L_q s + r_s}, \qquad \frac{i_{sd}}{\hat{v}_{sd}}(s) = \frac{1}{L_d s + r_s}. \tag{3.28}$$

Finally, the stator currents i_{sq} and i_{sd} can be controlled independently by two PI controllers [65], namely

$$\hat{v}_{sq} = \frac{K_{pq} s + K_{iq}}{s}(i^*_{sq} - i_{sq}), \qquad \hat{v}_{sd} = \frac{K_{pd} s + K_{id}}{s}(i^*_{sd} - i_{sd}), \tag{3.29}$$

where K_{pq}, K_{iq}, K_{pd} and K_{id} are corresponding gains of the PI controllers.

3.4 Power converter

The wind turbine generator is commonly connected to the power grid by a back-to-back converter. This back-to-back converter is an AC-DC-AC converter composed of a machine-inverter, a grid-inverter and a DC bus in between, as shown in Fig. 3.1.

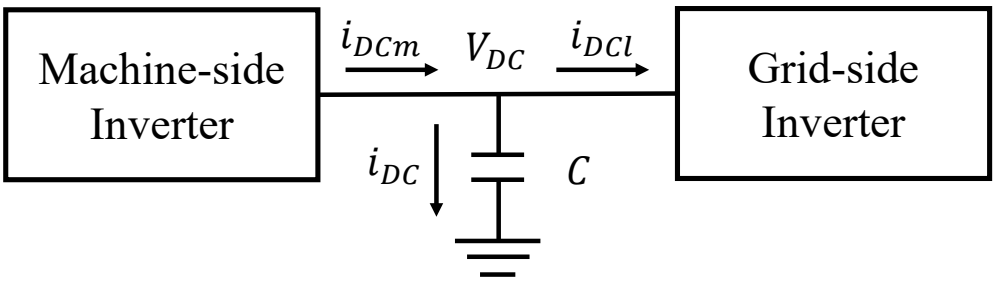

Figure 3.1: The diagram of the back-to-back converter.

The DC bus contains a large capacitor in parallel, which can be expressed as

$$\frac{d}{dt}V_{DC} = \frac{1}{C} i_{DC} = \frac{1}{C}(i_{DCm} - i_{DCl}), \tag{3.30}$$

where V_{DC} is the DC bus voltage, C is the DC bus capacity, i_{DC} is the current going

through the DC bus capacity, i_{DCm} is the current coming from the machine-inverter and i_{DCl} is the current go through the gird-inverter.

If two inverters are considered to be ideal without any losses, then the relationship between the AC-side and DC-side can be expressed as

$$\begin{aligned} \{v_l^{abc}\}^{\mathrm{T}} i_l^{abc} &= V_{DC} i_{DCl}, \\ \{v_s^{abc}\}^{\mathrm{T}} i_s^{abc} &= -V_{DC} i_{DCm}. \end{aligned} \tag{3.31}$$

where v_l^{abc}, i_l^{abc}, v_s^{abc} and i_s^{abc} are the grid-side and machine-side voltage and current, respectively.

3.5 Grid-side dynamics

Now we study the connection of the three-phase converter to the grid. If the three phases are assumed to be balanced[1], then we have

$$v_l^{abc} = r_l i_l^{abc} + L_l \frac{d}{dt} i_l^{abc} + v_z^{abc}, \tag{3.32}$$

where v_l is the voltage between the inverter and DC bus neutral, v_z is the voltage between the transformer and its neutral, i_l is the current flowing through the converter, r_l is the grid connection resistance and L_l is the grid connection inductance.

We again simplify the equation (3.32) by Park transformation, namely

$$\begin{aligned} v_l^{qd} &= r_l i_l^{qd} + L_l T(\theta) \frac{d}{dt} [T^{-1}(\theta) i_l^{qd}] + v_z^{qd}, \\ &= r_l i_l^{qd} + L_l T(\theta) [T^{-1}(\theta) \frac{d}{dt} i_l^{qd} + i_l^{qd} \frac{d}{d\theta} T^{-1}(\theta) \dot{\theta}] + v_z^{qd}, \\ &= r_l i_l^{qd} + L_l \frac{d}{dt} i_l^{qd} + L_l i_l^{qd} \dot{\theta} [T(\theta) \frac{d}{d\theta} T^{-1}(\theta)] + v_z^{qd}. \end{aligned} \tag{3.33}$$

[1]For an unbalanced grid, a similar equation can be obtained by applying the variable change based on the homopolar sequence of v_l and v_z.

Note that the above equation can be further simplified. Recall the Park transformation (3.16) and inverse Park transformation (3.17), then we have the property such that

$$T(\theta)\frac{d}{d\theta}T^{-1}(\theta) = \begin{bmatrix} 0 & 1 \\ -1 & 0 \end{bmatrix}. \tag{3.34}$$

Substitute (3.34) in (3.33) yields

$$v_l^{qd} = \begin{bmatrix} r_l & L_l\dot{\theta} \\ -L_l\dot{\theta} & r_l \end{bmatrix} i_l^{qd} + L_l\frac{d}{dt}i_l^{qd} + v_z^{qd}. \tag{3.35}$$

Finally, the dynamics of the current i_l^{qd} is given by

$$\frac{d}{dt}i_l^{qd} = \begin{bmatrix} -\frac{r_l}{L_l} & -\dot{\theta} \\ \dot{\theta} & -\frac{r_l}{L_l} \end{bmatrix} i_l^{qd} + \frac{1}{L_l}v_l^{qd} - \frac{1}{L_l}v_z^{qd} \tag{3.36}$$

3.6 Grid-side control

This section briefly recalls the grid-side control, namely the DC bus voltage regulation and the AC current control.

3.6.1 DC bus voltage regulation

The DC bus dynamics is described by (3.30). Applying the Laplace transformation to this equation yields

$$V_{DC}(s) = \frac{1}{Cs}i_{DCm}(s) - \frac{1}{Cs}i_{DCl}(s) \tag{3.37}$$

To control the DC bus voltage, we consider a simple PI controller, namely

$$K(s) = \frac{K_{pg}s + K_{ig}}{s} \tag{3.38}$$

where K_{pg} and K_{ig} are the proportion and integral gains, respectively. This leads to the closed-loop transfer function

$$T(s) = \frac{V_{DC}}{V_{DC}^*} = \frac{\frac{K(s)}{Cs}}{1 + \frac{K(s)}{Cs}}, \tag{3.39}$$

where V_{DC}^* is the reference value of the DC bus voltage.

If the current control loop ensures an ideal instantaneous response (*i.e.* $i_{DCl} = i_{DCl}^*$), then the current reference i_{DCl}^* can be expressed as

$$i_{DCl}^* = K(s)(V_{DC}^* - V_{DC}) + i_{DCm}. \tag{3.40}$$

3.6.2 AC current control

Similar to the generator vector control, the AC current is controlled by a feedback loop comparing the desired and actual current. Again, we calculate the current reference from the power reference as

$$i_{lq}^* = \frac{2}{3}\frac{P_z^*}{v_{zq}} = \frac{2}{3}\frac{V_{DC}}{v_{zq}} i_{DCl}^*, \qquad i_{ld}^* = \frac{2}{3}\frac{Q_z^*}{v_{zq}} = 0, \tag{3.41}$$

where i_{lq}^* and i_{ld}^* are the calculated current reference values. P_z^* and Q_z^* are the power reference values at the grid connection point.

Recall (3.35) with θ such that the q-axis is aligned with the voltage and the d-axis leads the q-axis, *i.e.* $v_{zd} = 0$ and $\dot{\theta} = 2\pi f$. There is a coupling between the q and d variables. Again, we apply the similar decoupling method as in Section 3.3, considering a feedback decoupling loop given by

$$v_l^{qd} = \hat{v}_l^{qd} + \begin{bmatrix} 0 & 2\pi f L_l \\ -2\pi f L_l & 0 \end{bmatrix} i_l^{qd} + \begin{bmatrix} v_{zq} \\ 0 \end{bmatrix} \tag{3.42}$$

where f is the electrical network frequency, $\hat{v}_l^{qd} = [\hat{v}_{lq}, \hat{v}_{ld}]^{\mathrm{T}}$ represents the outputs of

the current controllers. Assuming the decoupling is perfect, the dynamics of the system become

$$\hat{v}_l^{qd} = \begin{bmatrix} r_l & 0 \\ 0 & r_l \end{bmatrix} i_l^{qd} + \begin{bmatrix} L_l & 0 \\ 0 & L_l \end{bmatrix} \frac{d}{dt} i_l^{qd}. \tag{3.43}$$

Then, the current i_l^{qd} can be controlled by two independent PI controllers [65], namely

$$\hat{v}_{lq} = \frac{K_{pc}s + K_{ic}}{s}(i_{lq}^* - i_{lq}), \qquad \hat{v}_{ld} = \frac{K_{pc}s + K_{ic}}{s}(i_{ld}^* - i_{ld}), \tag{3.44}$$

where K_{pc} and K_{ic} are the corresponding gains of the PI controllers.

3.7 Wind Farm Model

A typical wind farm comprises multiple strings of wind turbine generators. Each generator is connected to a transformer and then connected to each other through cable lines with capacitors in parallel.

The mathematical description of an ideal transformer is represented by

$$\begin{aligned} v_1^{qd} - v_W^{qd} &= \begin{bmatrix} R_T & L_T\dot{\theta} \\ -L_T\dot{\theta} & R_T \end{bmatrix} i_1^{qd} + L_T \frac{d}{dt} i_1^{qd}, \\ v_N^{qd} - v_2^{qd} &= \begin{bmatrix} R_Z & L_Z\dot{\theta} \\ -L_Z\dot{\theta} & R_Z \end{bmatrix} i_2^{qd} + L_Z \frac{d}{dt} i_2^{qd}, \end{aligned} \tag{3.45}$$

where K is the turns ratio, *i.e.* $v_W^{qd} = K v_N^{qd}$ and $i_2^{qd} = K i_1^{qd}$, v_W^{qd} and v_N^{qd} are the generator-side and grid-side neutral point voltage, v_1^{qd}, i_1^{qd}, R_T, L_T, v_2^{qd}, i_2^{qd}, R_Z and L_Z are the generator-side and grid-side voltage, current, resistance and inductance, respectively.

The dynamics of the cable lines and of the capacitors are described as

$$\frac{d}{dt} i_{line}^{qd} = \frac{1}{L} \begin{bmatrix} -R & -L\dot{\theta} \\ L\dot{\theta} & -R \end{bmatrix} i_{line}^{qd} + v_{line}^{qd}, \tag{3.46}$$

and

$$\frac{d}{dt} v_c^{qd} = \begin{bmatrix} 0 & -\dot{\theta} \\ \dot{\theta} & 0 \end{bmatrix} v_c^{qd} + \frac{1}{C} i_c^{qd}, \tag{3.47}$$

where C is the capacitance, R is the cable line resistance, L is the cable line inductance, v_c^{qd}, i_c^{qd}, v_{line}^{qd}, and i_{line}^{qd} are the corresponding voltages and currents, respectively. Finally, the model of a string is obtained by considering (3.45), (3.46), (3.47) and the equations of the wind turbine.

3.8 Conclusion

In this chapter, the wind turbine model is reviewed, which is used later in Chapter 4. We have recalled the detailed mathematical description of a PMSG-type wind turbine, namely the wind turbine mechanism, generator dynamics, grid dynamics and the associated controllers. Finally, we introduce the model of transformers, cable lines and capacitors and how these components are used to construct a wind farm with wind turbines.

Chapter 4

Model Order Reduction of Large-scale Wind Farms: A Data-driven approach

4.1 Introduction

In recent years, there has been a significant increase in efforts to reduce the dependency on coal, petroleum, natural gas and other fossil fuels in order to overcome the effects of global warming. Society as a whole is motivated to replace traditional synchronous generators with renewable generations. In particular, wind farms, which are considered to be a clean, reliable and constant source of energy, are being deployed worldwide [66]. However, it is worth noting that in average more than 200 wind turbine generators (WTGs) are required to replace a single coal-fired power plant [67]. As a result, a detailed model of a large-scale wind farm typically contains thousands of differential equations. Such a detailed wind farm model can quickly become too complicated for further analysis, especially when hundreds of scenarios need to be simulated. Therefore, there is an urgent need to find reduced models that capture the main dynamics of the large-scale wind farm in a substantially smaller number of differential equations. This

problem is known as model order reduction (MOR). In the context of power systems, model order reduction is normally applied to a partition of the whole network. The idea is to distinguish between a study area, the description of which is maintained in full detail, and an external area (*e.g.* an off-shore wind farm), consisting of the remaining part of the network, which is linearised and reduced. The study area can be precisely analysed and controlled while still considering the interaction of the interconnection of such area with a less faithful representation of a larger external area. This allows faster simulations of hundreds of scenarios in a fraction of the time, [68–71].

Several MOR methods have been successfully applied to large-scale wind farms. Historically, the most widely used one is the aggregation method [72–78], which simply assumes that all WTGs operate uniformly at the same wind speed and output power, and replaces all WTGs with a single aggregated WTG. However, given that large-scale wind farms are typically distributed over a large area, it is unrealistic to assume that the WTGs operate under the same conditions. To overcome this, one may use multiple aggregated WTGs to represent WTGs under different operating conditions. However, the implementation of this method in wind farms remains limited. Unlike classical generators, which can be easily classified into coherent groups by means of their physical characteristic (*e.g.* rotor angle), the criteria for classifying the WTGs remains unclear. Furthermore, the operating conditions of the wind farm change continuously, resulting in dynamic coherent groups over time. Due to the above limitations, non-coherent based techniques have been considered for the reduction of wind farm models, such as Balanced Truncation (BT) [6, 79, 80], and Rational Krylov methods (RK) [6, 81, 82]. Some successful applications of BT and RK methods to power systems can be seen, for instance, in [83–86]. However, these methods have high computational complexity when reducing detailed wind farm models (*e.g.* some may require solving high dimensional Lyapunov equations). To improve this aspect, faster versions of these algorithms have been proposed, *e.g.* the Alternating Direction Implicit (ADI)-based Balanced Truncation [87] and the Iterative Rational Krylov Algorithm (IRKA) [88]. A detailed comparison of these methods is given in [69]. In addition to the high computational

complexity, another weakness of these methods is that they require full information about the model (*i.e.* the system matrices A, B and C, see (4.1)), which is not a realistic assumption, especially in the case of large-scale wind farms. Wind farm model parameters are commonly owned by commercial companies and are not made available to the operators and users, who may have access only to a black-box model. Therefore, in practice effective MOR approaches should be *model free* or, in other words, *data-driven*. A successful application of a data-driven approach to power systems is [68], in which a benchmark model of 16 classical generators is reduced. In particular, [68] (see also [49] for the mathematical development) proposed a **one-sided** time-domain data-driven MOR algorithm based on moment-matching. This approach allows selecting arbitrary "interpolation points" in the frequency domain such that the Bode plots of the full-order model (FOM) and of the reduced-order model (ROM) are matched at these particular frequencies. Some critical frequencies, which are important for analysis purposes and are strongly related to the mechanical and electrical characteristics of the power system are the so-called critical modes. Typically, critical modes are indicated by significant peaks in the magnitude of the Bode plot. Therefore, the moment-matching approach has the notable advantage of enabling the preservation of the critical modes, thus maintaining some physical meaning while reducing the model.

In this chapter, we propose a fully data-driven time-domain **two-sided** model reduction method for multiple input, multiple output (MIMO) systems. Moreover, the method is validated on a combined model of a 200-turbine wind farm (which represents the external area) and the IEEE 14-bus system (which represents the study area) in terms of Bode plots, eigenvalues, and PCC (Point of Common Coupling) voltages of the FOM and ROM. The contributions of this chapter have the following key advantages and novelties.

- With respect to [68], the proposed method is "two-sided". This means that the number of interpolation points is *doubled*. The implication is that for the same order, the ROM that we produce is as accurate as one with double its order. In

other words, we can construct a ROM with the same number of interpolation points but further reduces the order to *half*. Moreover [68] was validated on synchronous generators instead of wind turbine generators.

- With respect to the state-of-the-art of (model-based) MOR of wind farms, the proposed method is data-driven. This allows to apply the method even if the parameters of the wind farm are IP-protected and unknown to the user.

- Even when the model is available, the proposed method provides computational advantages with respect to model-based MOR. In this case synthetic data is generated in simulation by accurate or black-box models, and is noise free. We show that the execution of the proposed data-driven method has computational speed which is hundreds of times faster than the equivalent model-based method. Moreover, with respect to [68] (which considered only the noise free scenario) we propose robust variations of our data-driven algorithms that we demonstrate on data affected by noise. Thus, in the validation section (Section 4.4), we show a combination of comparisons with and without noise, to illustrate the advantages of the proposed method in both the real and synthetic data scenarios.

- With respect to [89] which considered the SISO case, the method is extended to MIMO systems and demonstrated on a combined model of a 200-turbine wind farm and the IEEE 14-bus system.

- With respect to [69], which achieved model-based MOR of a wind farm with an infinite bus (*i.e.* in isolation), our method is data-driven and validated on an integrated model where the wind farm is connected to the IEEE 14-bus system. Instead of simple voltage variations at the infinite bus, we consider extensive fault scenarios of the integrated model.

The rest of the chapter is organised as follows. In Section 4.2, some preliminaries on moment-matching are given. With a specific focus on MIMO systems, we introduce the moment-matching conditions along tangential directions. In Section 4.3, we propose

data-driven algorithms for the MOR of MIMO systems. In Section 4.4.1, we describe the combined model of the wind farm and the IEEE 14-bus system, the nonlinear model of the study area and the linearised model of the external area. In Section 4.4.2 the external area is reduced and compared with the FOM in terms of the Bode plot, while in Section 4.4.3 the robustness of the data-driven algorithms is assessed under noise conditions. In Section 4.4.4 the ROM is reconnected to the study area and validated in terms of eigenvalues and the PCC voltage. In Section 4.4.5, the performance of the data-driven MOR method is evaluated by comparing the time required to construct the ROM and the time to execute a simulation. In Section 4.4.6, we analyse the fault behaviour of the FOM and ROM. Finally, we provide some concluding remarks in Section 4.5.

4.2 Model-based model order reduction of MIMO systems

In this section we recall the model-based moment-matching method for linear MIMO systems. We first recall a family of ROMs matching ν so-called right interpolating conditions, then a family of ROMs matching ν so-called left interpolating conditions, and then show how to obtain a ROM that matches 2ν interpolating conditions.

4.2.1 Right Interpolation ≡ Direct Interconnection

Consider a linear MIMO continuous-time system

$$\dot{x} = Ax + Bu, \qquad y = Cx, \tag{4.1}$$

where $x(t) \in \mathbb{R}^n$ is the state, $u(t) \in \mathbb{R}^m$ is the input, $y(t) \in \mathbb{R}^p$ is the output, $A \in \mathbb{R}^{n\times n}$, $B \in \mathbb{R}^{n\times m}$, $C \in \mathbb{R}^{p\times n}$ are the system matrices. Without loss of generality system (4.1)

is assumed to be the minimal realisation of the transfer matrix $W(s) = C(sI - A)^{-1}B$. We now introduce the definition of moments.

Definition 4.1. Let $s_i \in \mathbb{C}\backslash\sigma(A)$ and $l_i \in \mathbb{R}^m$. The *k-moment of system* (4.1) *along* l_i is a vector defined as $\eta_k(s_i, l_i) = \dfrac{(-1)^k}{k!}\left[\dfrac{d^k}{ds_i^k}W(s_i)\right] l_i$, for $k \geq 0$ integer.

The quantities s_i are called interpolation points, while the quantities l_i are called right tangential directions.

The idea of MOR by moment-matching is to construct a ROM with transfer function $\hat{W}(s)$ (and k-moment along l_i called $\hat{\eta}_k(s_i, l_i)$) that, for ν interpolation points s_i, satisfies the right side moment-matching condition, namely

$$\eta_k(s_i, l_i) = \hat{\eta}_k(s_i, l_i), \qquad \text{for } i = 1, ..., \nu. \tag{4.2}$$

This problem is readily solved as follows: let $S \in \mathbb{R}^{\nu\times\nu}$ be any matrix with characteristic and minimal polynomials $p(s) = \prod_{i=1}^{\bar{k}}(s - s_i)^{k_i}$, where $\nu = \sum_{i=1}^{\bar{k}} k_i$, and $L = [l_1, l_2, ..., l_\nu] \in \mathbb{R}^{m\times\nu}$, any matrix such that (S, L) is an observable pair. Then, the family of models

$$\dot{\xi} = (S - GL)\xi + Gu, \qquad \psi = C\Pi\xi, \tag{4.3}$$

achieves moment-matching at the interpolation points encoded by S along the directions encoded by L, for any $G \in \mathbb{R}^{\nu\times m}$ such that $\sigma(S) \cap \sigma(S - GL) = \emptyset$, as long as L is selected as in [90, Section 2.4] (*e.g.* $l_i = l \neq 0_{m\times 1}$ for all i). The quantity Π in (4.3) is the unique solution of the Sylvester equation

$$A\Pi + BL = \Pi S. \tag{4.4}$$

It is important to notice for the sake of the data-driven algorithms that we develop in this chapter, that the quantity $C\Pi\omega(t)$ is the steady-state output y_{ss} of system (4.1)

interconnected (see Fig. 4.1) with the input produced by the generator

$$\dot{\omega} = S\omega, \qquad u = L\omega. \tag{4.5}$$

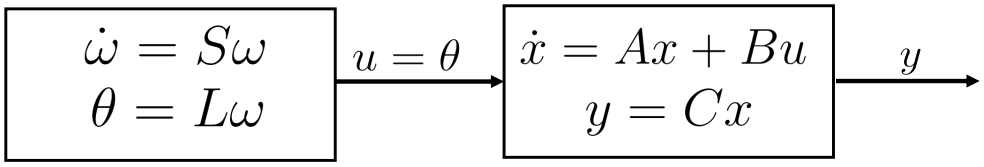

Figure 4.1: The diagram of the direct interconnection.

4.2.2 Left Interpolation ≡ Swapped Interconnection

The same approach can be developed for the so-called left-side interpolation data.

Definition 4.2. Let $q_i \in \mathbb{C}\backslash\sigma(A)$ (interpolation points) and $r_i \in \mathbb{R}^{1\times m}$ (left tangential directions). The *k-moment of system* (4.1) *along* r_i is a vector defined as $\mu_k(q_i, r_i) = r_i \dfrac{(-1)^k}{k!}\left[\dfrac{d^k}{dq_i^k}W(q_i)\right]$, for $k \geq 0$ integer.

Similarly to before, we now want to find a ROM with moments $\hat{\mu}_k(q_i, r_i)$, such that

$$\mu_k(q_i, r_i) = \hat{\mu}_k(q_i, r_i), \qquad \text{for } i = 1, ..., \nu. \tag{4.6}$$

Also this problem is readily solved: let $Q \in \mathbb{R}^{\nu\times\nu}$ be any matrix with characteristic and minimal polynomials $p(q) = \prod_{i=1}^{\bar{k}}(q - q_i)^{k_i}$, where $\nu = \sum_{i=1}^{\bar{k}} k_i$, and $R = [r_1^\top, r_2^\top, ..., r_\nu^\top]^\top \in \mathbb{R}^{\nu\times p}$, any matrix such that (Q, R) is a reachable pair. Then, the family of models

$$\dot{\xi} = (Q - RH)\xi + \Upsilon Bu, \qquad \psi = H\xi, \tag{4.7}$$

achieve moment-matching at the interpolation points encoded by Q along the direction encoded by R, for any $H \in \mathbb{R}^{p\times\nu}$ such that $\sigma(Q) \cap \sigma(Q - RH) = \emptyset$, as long as $R^\top$ is

selected as in [90, Section 2.4] (*e.g.* $r_i = r \neq 0_{1\times p}$ for all i). The quantity Υ in (4.7) is the unique solution of the Sylvester equation

$$\Upsilon A + RC = Q\Upsilon, \tag{4.8}$$

It is important to notice (see [53]) for the sake of the data-driven algorithms that we develop in this chapter, that **for SISO systems** the quantity $e^{Qt}\Upsilon B$ is the output d or steady-state of ϖ of the system

$$\dot{\varpi} = Q\varpi + Ry, \qquad d = \varpi + \Upsilon x, \tag{4.9}$$

that filters the output impulse response of system (4.1), that is $d(t) = \varpi_{ss}(t) = e^{Qt}\Upsilon B$ (see Fig. 4.2). In this chapter, we prove these properties **for MIMO systems**.

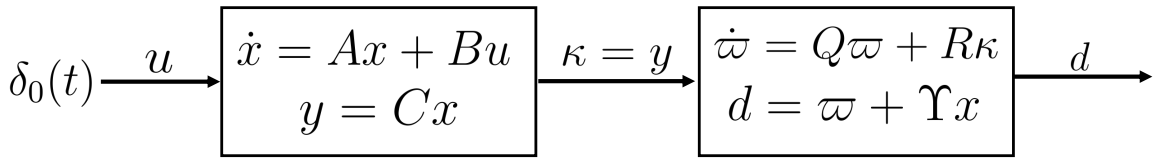

Figure 4.2: The diagram of the swapped interconnection.

4.2.3 Concurrent Left and Right Interpolation ≡ Two-sided Interconnection

The ROM (4.3) [(4.7) respectively] are of order ν and match ν right [left] interpolation condition while they have a free G [H]. It is possible to select G [H] in such a way that also the left [right] interpolation conditions are satisfied (assuming that these conditions are different, *i.e.* $\sigma(S) \cap \sigma(Q) = \emptyset$). In particular, the ROM (4.3) [(4.7)] with

$$G = (\Upsilon\Pi)^{-1}\Upsilon B, \qquad [H = C\Pi(\Upsilon\Pi)^{-1}]$$

matches both left and right interpolation data (see [91]). Thus the obtained reduced-order model of order ν matches 2ν moments. It is important to notice for the sake of the data-driven algorithms that this setup corresponds to the two-sided interconnection shown in Fig. 4.3 for which the steady-state property $d_{ss}(t) - \varpi_{ss}(t) = \Upsilon\Pi\omega(t)$ holds.

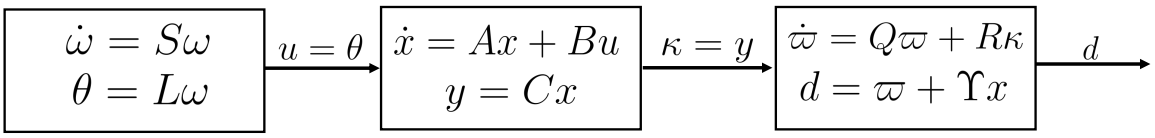

Figure 4.3: The diagram of the two-sided interconnection.

The idea of the method presented in this chapter is to use time series of the outputs of these interconnections to generate a two-sided reduced-order model without solving (4) and (8) or using A, B and C.

4.3 Data-driven model order reduction of MIMO systems

One can see that the ROMs proposed in (4.3) and (4.7) rely on the unique solutions of the Sylvester equations (4.4) and (4.8) respectively. Since these Sylvester equations involve $n \times \nu$ conditions, if n is large they are computationally challenging to solve. This results in high computational complexity when implementing this approach to wind farms which are commonly large-scale. Furthermore, as mentioned in Section 4.1, detailed information of the system matrices (*i.e.* A, B and C) of large-scale wind farms may not be available. Thus, we are motivated to find a data-driven MOR approach that requires input-output data only.

A data-driven algorithm for two-sided MOR of SISO systems has been proposed in [89]. However, large-scale wind farms are commonly modeled with multiple inputs and multiple outputs (*i.e.* voltages and currents in dq framework). Thus, a MIMO method is required. A data-driven algorithm for *one-sided* MOR of MIMO systems was presented

in [68]. Here we propose a novel algorithm for *two-sided* MOR of MIMO systems, thus producing ROMs with double the accuracy of the method[1] given in [68].

From Section 4.2 we have seen that a reduced-order model by moment-matching that achieved two-sided interpolation can be constructed as

$$\dot{\xi} = (S - (\Upsilon\Pi)^{-1}\Upsilon BL)\xi + (\Upsilon\Pi)^{-1}\Upsilon Bu, \qquad \psi = C\Pi\xi, \tag{4.10}$$

if we have the matrices $C\Pi$, ΥB and $\Upsilon\Pi$. Therefore, the data-driven approach consists in finding accurate approximations $\widetilde{C\Pi}$, $\widetilde{\Upsilon B}$ and $\widetilde{\Upsilon\Pi}$ from data.

4.3.1 Constructing $\widetilde{C\Pi}$

Consider the experimental setup in Fig. 4.1 or Fig. 4.3 in which the system is excited with inputs produced by the generator (4.5). Samples of the output $y(t_i)$ of the system are collected together with $\omega(t_i)$ (the latter can be collected or computed exactly). Then the following theorem provides a formula to estimate $C\Pi$.

Theorem 4.1. Consider the interconnection of system (4.1) and the signal generator (4.5). Assume $\sigma(A) \subset \mathbb{C}_{<0}$, $\sigma(S) \subset \mathbb{C}_0$, S has simple eigenvalues and the triple $(L, S, \omega(0))$ is minimal. For $\widetilde{\nu} \geq \nu$, define the time-snapshots $\widetilde{R}_k \in \mathbb{R}^{\widetilde{\nu}\times\nu}$ and $\widetilde{E}_k^j \in \mathbb{R}^{\widetilde{\nu}}$ as

$$\widetilde{R}_k = [\omega(t_{k-\widetilde{\nu}+1}) \cdots \omega(t_{k-1})\ \omega(t_k)]^\top,$$
$$\widetilde{E}_k^j = [y^j(t_{k-\widetilde{\nu}}+1) \cdots y^j(t_{k-1})\ y^j(t_k)]^\top,$$

where $y^j(t_i)$ is the j-th row of $y(t_i)$. Denote the j-th row of C as C^j. Then,

$$\operatorname{vec}\left(\widetilde{C^j\Pi_k}\right) = (\widetilde{R}_k^\top \widetilde{R}_k)^{-1}\widetilde{R}_k^\top \widetilde{E}_k^j. \tag{4.11}$$

is an *online estimate* of $C^j\Pi$, which is the j-th row of $C\Pi$, namely there exists a

[1]There is also a difference in the MIMO aspect with respect to [68]. In [68], a heuristic was used to determine L, producing only *approximate* one-sided moment-matching. Here, L and R are selected based on the recent results in [90]. The resulting ROM is not an approximation.

sequence $\{t_k\}$ such that $\widetilde{R}_k^\top \widetilde{R}_k$ is full rank and $\lim_{k\to\infty} \widetilde{C^j\Pi}_k = C^j\Pi$.

Proof. The minimality of the triple $(L, S, \omega(0))$ implies the excitability of the pair $(S, \omega(0))$. By [92, Lemma 3], there exists a time sequence $\{t_k\}$ with $\lim_{k\to\infty} t_k = \infty$ such that the time-snapshots $\widetilde{R}_k$ is column full rank. The rest of the proof is the same as the proof of [68, Theorem 2].

□

With the convergence guarantees provided by Theorem 4.1, the quantity $C\Pi$ can be approximated by Algorithm 1 as follows.

Algorithm 1 Approximate $C\Pi$

Input: A sufficiently large integer $k_0 \in \mathbb{Z}_{>0}$ and sufficiently small error thresholds $\eta^j_{C\Pi} > 0$, with $j = 1, ..., p$. Let $\widetilde{\nu} = \nu$ (increase $\widetilde{\nu}$ sufficiently for robustness).

1: **for** $j = 1$ to p **do**
2: Let $k = k_0$.
3: Construct the matrices $\widetilde{R}_k$ and $\widetilde{E}^j_k$.
4: **if** $\text{rank}(\widetilde{R}_k) = \nu$ **then**
5: Compute $\widetilde{C^j\Pi}_k$ from equation (4.11).
6: **if** $\dfrac{||\widetilde{C^j\Pi}_k - \widetilde{C^j\Pi}_{k-1}||}{t_k - t_{k-1}} > \eta^j_{C\Pi}$ **then**
7: $k = k + 1$ go to 3.
8: **end if**
9: **else**
10: Increase $\widetilde{\nu}$ go to 3.
11: **end if**
12: **return** $\widetilde{C^j\Pi}_k$.
13: **end for**
14: **return** $\widetilde{C\Pi}_k$.

Algorithm 1 can be made robust against measurement noise. It is enough to pick a larger $\widetilde{\nu}$. This variant gives the optimal estimation (i.e. maximum likelihood estimation) of $C^j\Pi$ when the measurements are affected by Gaussian additive noise.

4.3.2 Constructing $\widetilde{\Upsilon B}$

Consider the experimental setup in Fig. 4.2 in which the output impulse response of system (4.1) is filtered by (4.9). Samples of the filtered state $\varpi(t_i)$ are collected together

with the quantities e^{Qt_i} (these can be computed exactly). Then the following theorem provides a formula to estimate ΥB.

Theorem 4.2. Consider the interconnection of system (4.1) and (4.9). Assume $\sigma(A) \subset \mathbb{C}_{<0}$, $\sigma(Q) \subset \mathbb{C}_0$, Q has simple eigenvalues and the pair (Q, R) is reachable. Denote the j-th column of B as B^j. Let the initial conditions $x(0) = 0$ and $\varpi(0) = 0$, and the input of the j-th experiment $u_j = e_j \delta_0(t)$. Then

$$\widetilde{\Upsilon B}_k^j := e^{-Qt_k} \varpi(t_k) \tag{4.12}$$

is an online estimate of ΥB^j with the following asymptotic property: there exists a time sequence $\{t_k\}$ such that $\lim_{k\to\infty} \widetilde{\Upsilon B}_k^j = \Upsilon B^j$.

Proof. Since Υ is the unique solution of the Sylvester equation (4.8), we have

$$\begin{aligned} \dot{d} &= \dot{\varpi} + \Upsilon \dot{x} = Q\varpi + Ry + \Upsilon(Ax + Bu) \\ &= Q\varpi + (RC + \Upsilon A)x + \Upsilon B u = Q(\varpi + \Upsilon x) + \Upsilon B u \\ &= Qd + \Upsilon B u \end{aligned} \tag{4.13}$$

Since the initial condition $x(0) = 0$ and $\varpi(0) = 0$, we have $d(0) = \varpi(0) + \Upsilon x(0) = 0$. Then, the input $u = e_j \delta_0(t)$ yields $\varpi(t) + \Upsilon x(t) = d(t) = e^{Qt} \Upsilon B^j$. Note that system (4.1) is assumed to be asymptotically stable. Thus, $x(t) \to 0$ as $t \to \infty$ yielding

$$\begin{aligned} \Upsilon B^j &= \lim_{t\to\infty} e^{-Qt}(\varpi(t) + \Upsilon x(t)) \\ &= \lim_{t\to\infty} e^{-Qt} \varpi(t). \end{aligned}$$

This proves Theorem 4.2.

□

Equation (4.12) can be made robust against measurement noise. To this end we replace (4.12) with

$$\operatorname{vec}\left(\widetilde{\Upsilon B}_k^j\right) = (\widetilde{P}_k^\top \widetilde{P}_k)^{-1} \widetilde{P}_k^\top \widetilde{O}_k^j, \tag{4.14}$$

where $\widetilde{O}_k^j \in \mathbb{R}^{\widetilde{q}\nu}$ and $\widetilde{P}_k \in \mathbb{R}^{\widetilde{q}\nu \times \nu}$ are defined as

$$\widetilde{O}_k^j = [\varpi(t_{k-\widetilde{q}+1})^\top \cdots \varpi(t_{k-1})^\top \ \varpi(t_k)^\top]^\top,$$
$$\widetilde{P}_k = [e^{Q^\top t_{k-\widetilde{q}+1}} \cdots e^{Q^\top t_{k-1}} \ e^{Q^\top t_k}]^\top,$$

and note that $\widetilde{P}_k$ is always full column rank. The robustness claim is a consequence of (4.14) being the least-square version of (4.12). For a sufficiently large number $\widetilde{q}$, this variant gives the optimal estimation (i.e. maximum likelihood estimation) of ΥB^j when the measurements are affected by Gaussian additive noise. The results of this section are summarised in Algorithm 2.

Algorithm 2 Approximate ΥB

Input: A sufficiently large integer $k_0 \in \mathbb{Z}_{>0}$ and sufficiently small error thresholds $\eta^j_{\Upsilon B} > 0$ with $j = 1, ..., m$. Let $\widetilde{q} = 1$ (increase $\widetilde{q}$ sufficiently for robustness).

1: **for** $j = 1$ to m **do**
2: Let $k = k_0$.
3: Produce the data with the input $u_j = e_j \delta_0(t)$.
4: Construct the matrices $\widetilde{O}_k^j$ and $\widetilde{P}_k$.
5: Compute $\widetilde{\Upsilon B}_k^j$ from equation (4.14).
6: **if** $\dfrac{||\widetilde{\Upsilon B}_k^j - \widetilde{\Upsilon B}_{k-1}^j||}{t_k - t_{k-1}} > \eta^j_{\Upsilon B}$ **then**
7: $k = k + 1$ go to 4.
8: **end if**
9: **return** $\widetilde{\Upsilon B}_k^j$.
10: **end for**
11: **return** $\widetilde{\Upsilon B}_k$.

4.3.3 Constructing $\widetilde{\Upsilon\Pi}$

Provided with satisfying approximations $\widetilde{C\Pi}_k$ and $\widetilde{\Upsilon B}_k$, we are left with the problem of estimating $\Upsilon\Pi$ from data. For SISO systems, [89] proposed a third algorithm based on an additional experiment and the use of a "surrogate" system (see [89] for details). Here we present an alternative method (for both SISO and MIMO systems) that has the advantage of not requiring a third experiment and algorithm.

By multiplying equation (4.4) from the left by Υ, and equation (4.8) from the right by

Π and matching the resulting common terms $\Upsilon A\Pi$, yield the new equation

$$Q\Upsilon\Pi - \Upsilon\Pi S = RC\Pi - \Upsilon BL.$$

Exploiting the approximations $\widetilde{C\Pi}_k$ and $\widetilde{\Upsilon B}_k$, we can find an approximation of $\Upsilon\Pi$ by solving the Sylvester equation

$$Q\widetilde{\Upsilon\Pi}_k - \widetilde{\Upsilon\Pi}_k S = R\widetilde{C\Pi}_k - \widetilde{\Upsilon B}_k L \tag{4.15}$$

with respect to $\widetilde{\Upsilon\Pi}_k$. This equation has a unique solution as long as Q and S have no common eigenvalues. Since Q and S are arbitrary, this is not a restriction. Moreover, note that differently from the Sylvester equations (4.4) and (4.8) that correspond to n by ν and ν by n scalar equations, respectively, the Sylvester equation (4.15) only involves ν by ν scalar equations. Since $\nu \ll n$, the computational complexity of solving (4.15) is small and does not need to be avoided as it was the case for (4.4) and (4.8).

4.3.4 Algorithmic overview

The complete method can be summarised as a flowchart in Fig. 4.4. Once the study and external areas are given, we determine a linearised model of the external area. The next step consists in selecting the number and location of the interpolation points and the corresponding tangential directions for the right and left side moment-matching. These parameters can be selected based on user's knowledge of the wind farm or its operating conditions, or by using a fast Fourier transform on available data to determine the frequencies of interest to be interpolated. We construct the interconnected systems to generate the data $y(t)$, $\omega(t)$, and $\varpi(t)$, and compute $\widetilde{C\Pi}_k$ and $\widetilde{\Upsilon B}_k$ by Algorithm 1 and Algorithm 2 respectively. $\widetilde{\Upsilon\Pi}_k$ is obtained by solving (4.15). Finally, the two-sided reduced-order model is given by (4.10). If the resulting ROM is not satisfactory, we return to the step of selecting the interpolation points and tangential directions. Otherwise, we stop. An illustrative Demo of the method is available in Appendix A.

Remark 4.1. One may find that data-driven MOR has in common with system identification, as both of the techniques can construct a (reduced-order) model using the data. However, the data required for the proposed method is less, presenting lower computational complexity. Furthermore, the proposed method allows arbitrarily selecting interpolation points in the frequency domain such that the Bode plots match at the selected frequencies. This allows for maintaining some mechanical and electrical characteristics of the wind farm when constructing the model.

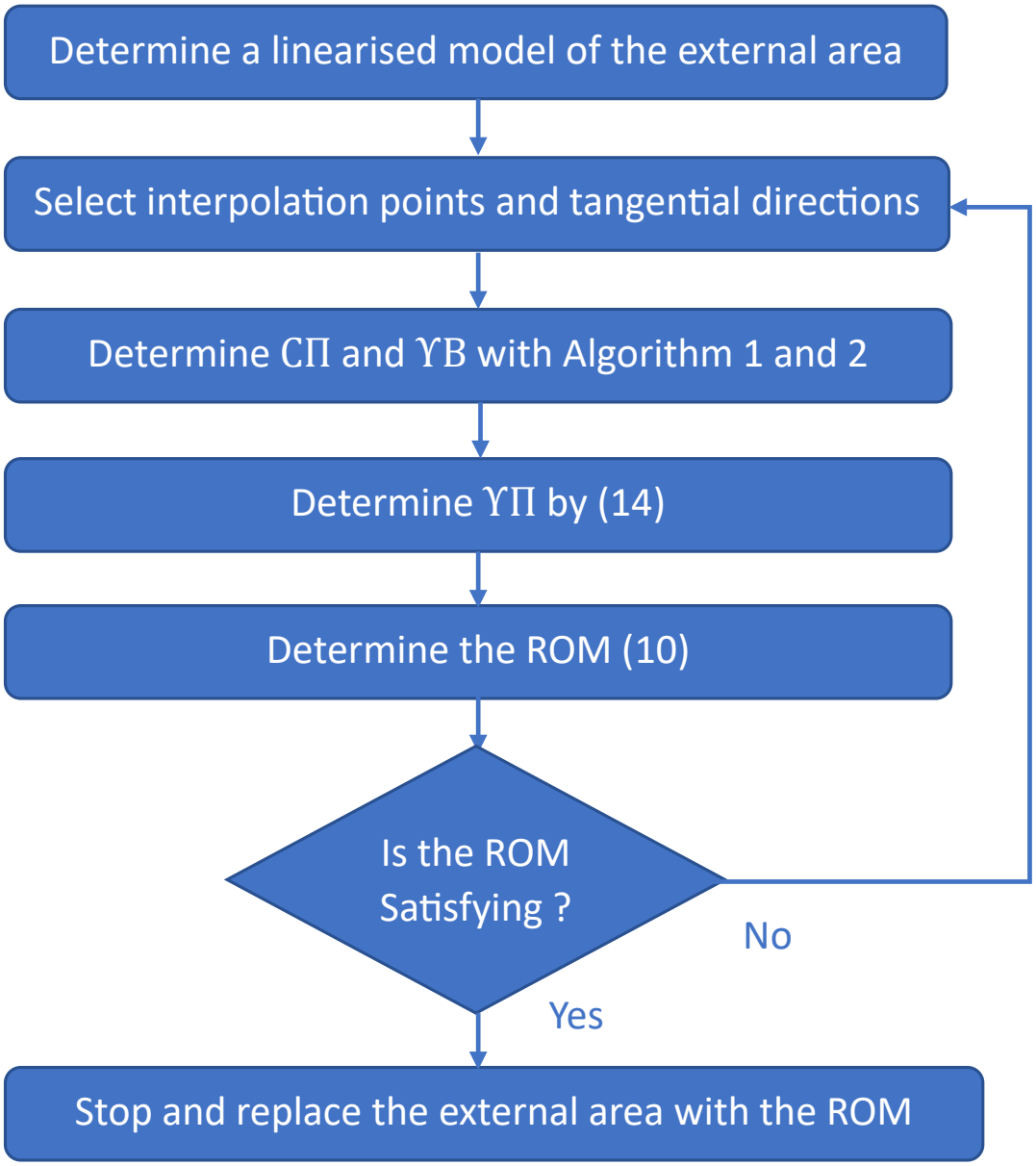

Figure 4.4: Algorithmic overview of the method

4.3.5 Example: A pre-validation on the CD player model

Before applying the proposed method to the wind farm, we first validate it on a CD player model with 2 inputs, 2 outputs and 120 states, commonly used as a benchmark model for model order reduction [51, 52]. In this example, the interpolation points are selected as $\pm 0.1\iota$, $\pm 1\iota$, $\pm 23\iota$, $\pm 48\iota$, $\pm 65\iota$, $\pm 80\iota$, $\pm 87\iota$, $\pm 130\iota$, $\pm 300\iota$, $\pm 440\iota$, $\pm 587\iota$ and $\pm 688\iota$ for the right interpolation and $\pm 0.5\iota$, $\pm 10\iota$, $\pm 28.3\iota$, $\pm 60\iota$, $\pm 75\iota$, $\pm 83\iota$, $\pm 100\iota$, $\pm 200\iota$, $\pm 350\iota$, $\pm 520\iota$, $\pm 600\iota$ and $\pm 1000\iota$ for the left interpolation. This selection results in a reduced-order model of order $\nu = 24$. Fig. 4.5 to Fig. 4.7 compare the bode plot of the right-side moment-matching, the left-side moment-matching and the transfer function matrix, respectively. In particular, the blue solid lines represent the quantities related to the FOM, the black dotted lines represent the quantities related to the model-based ROM and the dashed red lines represent the quantities related to the data-driven ROM. We conclude that the data-driven ROM is as accurate as the model-based one and recovers the performance of the FOM precisely.

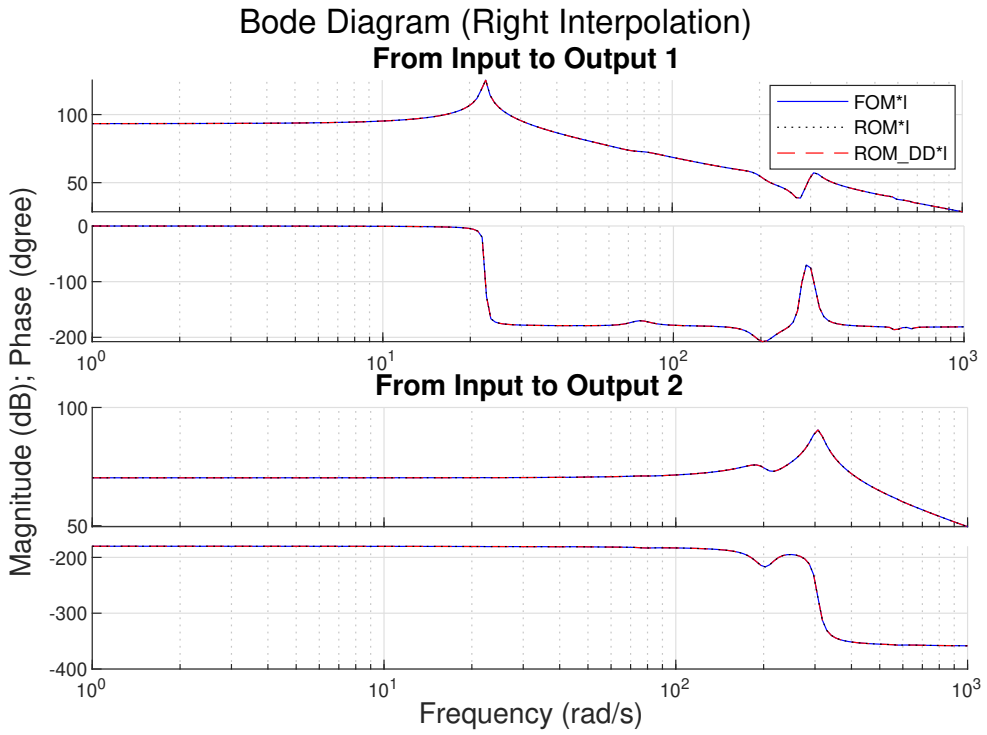

Figure 4.5: Bode plot of the right side moment-matching along the tangential direction l. The solid blue line, black dotted line and red dashed line represent the quantities for the FOM, ROM (model-based) and ROM_DD (data-driven), respectively.

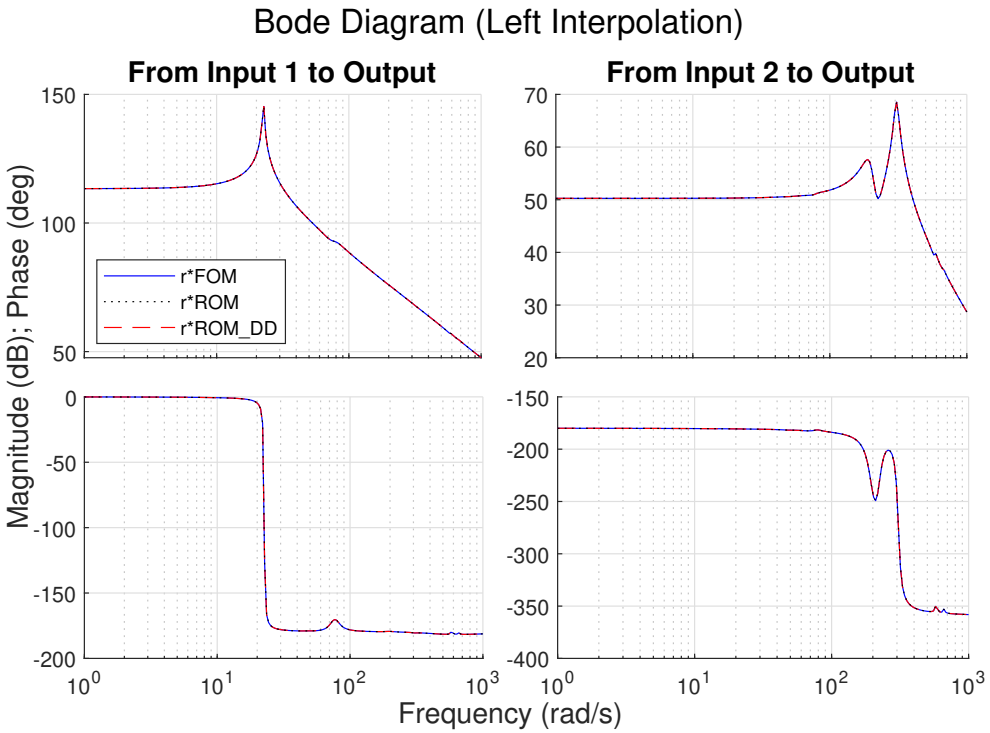

Figure 4.6: Bode plot of the left side moment-matching along the tangential direction l. The solid blue line, black dotted line and red dashed line represent the quantities for the FOM, ROM (model-based) and ROM_DD (data-driven), respectively.

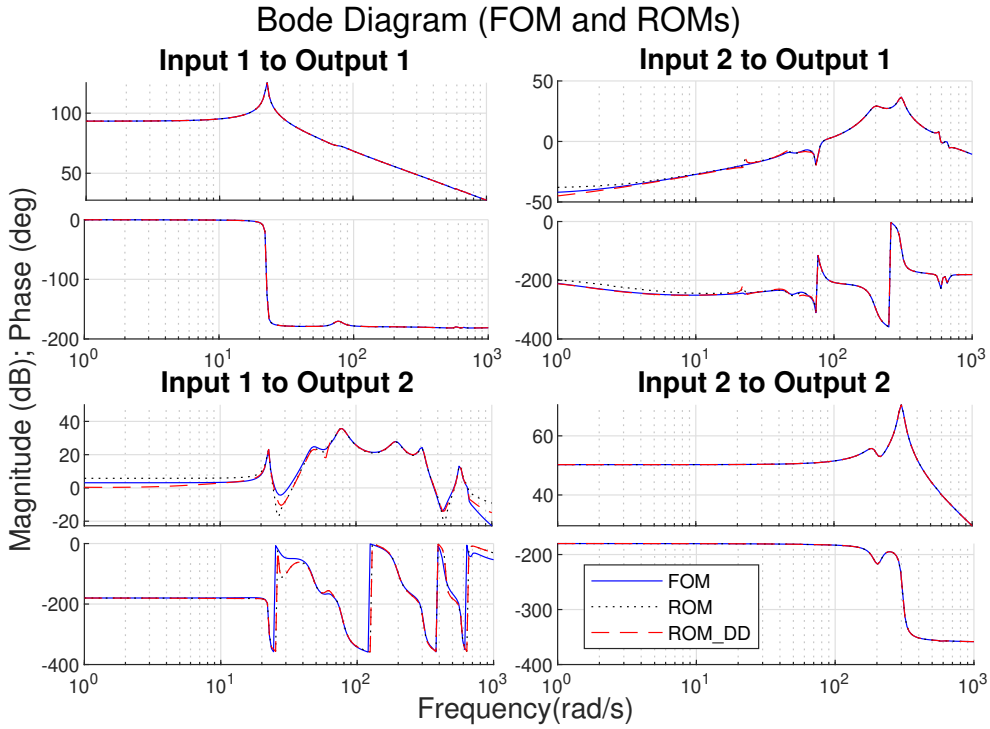

Figure 4.7: Bode plot of the FOM and ROMs. The solid blue line, black dotted line and red dashed line represent the FOM, ROM (model-based) and ROM_DD (data-driven), respectively.

4.4 Application to large-scale wind farms

In this section we present extensive simulation results to validate the proposed method. After introducing the wind farm model used in this work (Section 4.4.1) and the obtained ROM (Section 4.4.2), we first evaluate the robustness of the data-driven algorithms to measurement noise (Section 4.4.3) and then compare the FOM and the ROM in terms of eigenvalues, PCC voltage, computational time and fault behaviour (Sections 4.4.4, 4.4.5, 4.4.6).

4.4.1 Combined system: a wind farm interconnected to the grid

To validate our MOR approach, we consider a 200 $\times$ 1MW wind farm of type-4 wind turbine generators (WTGs) in a 50Hz power system. The basic layout of the combined system is shown in Fig. 4.8. The wind farm consists of 20 strings, where each string contains 10 WTGs, while the rest of the power system consists of 14 buses, 5 synchronous generators, 11 loads and 20 transmission lines (see Appendix A for more detail). The wind farm is connected to the Bus 7. In Fig. 4.8, each triangle represents a WTG connected to a wind turbine transformer (WTT). The dynamic model of a single WTG has order 9 (see *e.g.* [57]), which increases to 17 once connected with the transformer and cable. The full detailed model is given in Chapter 3 while the parameters used in this study are provided in Appendix A. The large-scale wind farm and the IEEE 14-bus system are modelled using Matlab/Simulink. We define the study area and the external area as shown in Fig. 4.8. The study area is preserved while the external area is linearised using the linearisation toolbox in Matlab/Simulink (see [69, 71]). The resulting model of the external area has an order of 3402 with 1592 conjugate pairs of eigenvalues. This linear FOM of the external area includes two inputs and two outputs, namely the current at the wind farm transformer (WFT) on the qd-axis and the PCC voltage on the qd-axis, respectively. The FOM of the external area is subsequently

reduced by our data-driven approach and reconnected to the study area for comparison and validation against the FOM. Note that for the purpose of model order reduction, no parameters or system matrices are used. Only the data as defined in the data-driven algorithms are used. The matrices are used only for validation purposes.

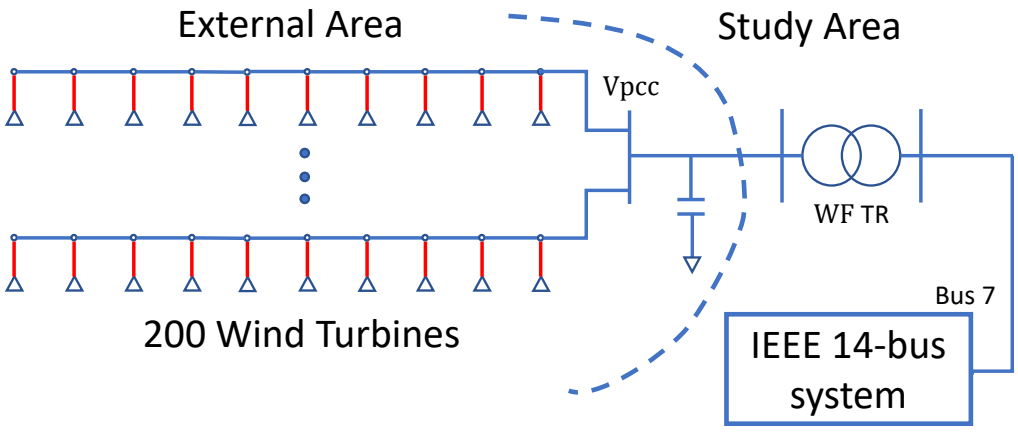

Figure 4.8: The layout of the combined system.

4.4.2 Design of the reduced-order model

Following the development of Section 4.3, we implement Algorithm 1, Algorithm 2 and solve[2] (4.15), finding estimations of $C\Pi$, ΥB and $\Upsilon\Pi$, respectively. The first step is to determine the interpolation points and the corresponding tangential directions for moment-matching. In this example, the interpolation points are selected by spreading them between the frequencies[3] of 0Hz and 10000Hz, placing some of these frequencies in S and some in Q. Specifically, we used $\pm 1\iota$, $\pm 20\iota$, $\pm 70\iota$, $\pm 120\iota$, $\pm 300\iota$, $\pm 500\iota$, $\pm 700\iota$, $\pm 900\iota$, $\pm 4400\iota$ and $\pm 8500\iota$ for Algorithm 1 and $\pm 10\iota$, $\pm 50\iota$, $\pm 100\iota$, $\pm 200\iota$, $\pm 400\iota$, $\pm 600\iota$, $\pm 800\iota$, $\pm 1000\iota$, $\pm 7000\iota$ and $\pm 10000\iota$ for Algorithm 2. We select the tangential directions according to [90] as $l_i = [1, 4]^\top$ and $r_i = [4, 1]$ for all $i = 1, \ldots, \nu$ for the direct and swapped moment-matching, respectively. The performance of the

[2]Using the function "sylvester" in Matlab.

[3]It may not always be possible to arbitrarily select the input of system (4.1) as in Fig. 4.1 and Fig. 4.2, and in reality the input signal may be composed of several unwanted frequencies. For this case, one can use a band-pass filter and apply the algorithms to the filtered data, as suggested for instance in [49, Remark 2].

data-driven algorithms is evaluated by the normalised approximation error defined as

$$e_{\mathrm{x}} = \frac{||\widetilde{\mathrm{x}}_k - \mathrm{x}||}{||\mathrm{x}||},$$

where x is any quantity required to construct the ROM (*i.e.* $C\Pi$, ΥB and $\Upsilon\Pi$) and $\widetilde{\mathrm{x}}_k$ is the corresponding approximation given by the data-driven algorithm (*i.e.* $\widetilde{C\Pi}_k$ $\widetilde{\Upsilon B}_k$ and $\widetilde{\Upsilon\Pi}_k$). The system is simulated for 100 seconds to generate sufficient data[4] for the two algorithms. This yields sufficiently small normalised approximation errors $e_{C\Pi} = 2.1 \times 10^{-6}$ and $e_{\Upsilon B} = 8.8 \times 10^{-4}$. Once satisfactory approximations of $C\Pi$ and ΥB are obtained, we solve equation (4.15) to estimate $\Upsilon\Pi$, yielding a normalised approximation error of $e_{\Upsilon\Pi} = 1.2 \times 10^{-6}$. Provided with approximations $\widetilde{C\Pi}_k$, $\widetilde{\Upsilon B}_k$ and $\widetilde{\Upsilon\Pi}_k$, the ROM is given by (4.10).

Fig. 4.9 and Fig. 4.10 compare the Bode plots for the right- and left-side moment-matching, respectively. In particular, the blue solid lines represent quantities related to the FOM, the black dotted lines represent quantities related to the model-based ROM and the dashed red lines represent quantities related to the data-driven ROM. The figures show that the selection of the interpolation points is effective and the transfer matrix along the tangential directions is perfectly matched. Hence, the performance of the model-based reduced-order model is fully recovered by the data-driven approach. In Fig. 4.11, the Bode plot of the FOM and ROMs (model-based and data-driven) are represented by solid blue, black dotted and red dashed lines, respectively. Note that while there is no guarantee that the transfer matrix is well matched (the guarantee is along the left and right directions only), the figure clearly shows that the transfer matrix itself is well matched across all the considered frequencies.

In conclusion, in terms of quality of matching, the performance of the data-driven algorithm in absence of noise is satisfactory and equivalent to a model-based method. It is important to stress that this result is very valuable even when the model of the system is available and noiseless data is generated by means of simulations because, as

[4]In practice, the required data can be collected by the phase measurement unit (PMU). In this example, the data is obtained directly from simulations.

shown later in Section 4.4.5, the data-driven method produces a reduced-order model in much less computational time than the model-based approach. Nevertheless, we study the robustness of the data-driven method to measurement noise in the next section.

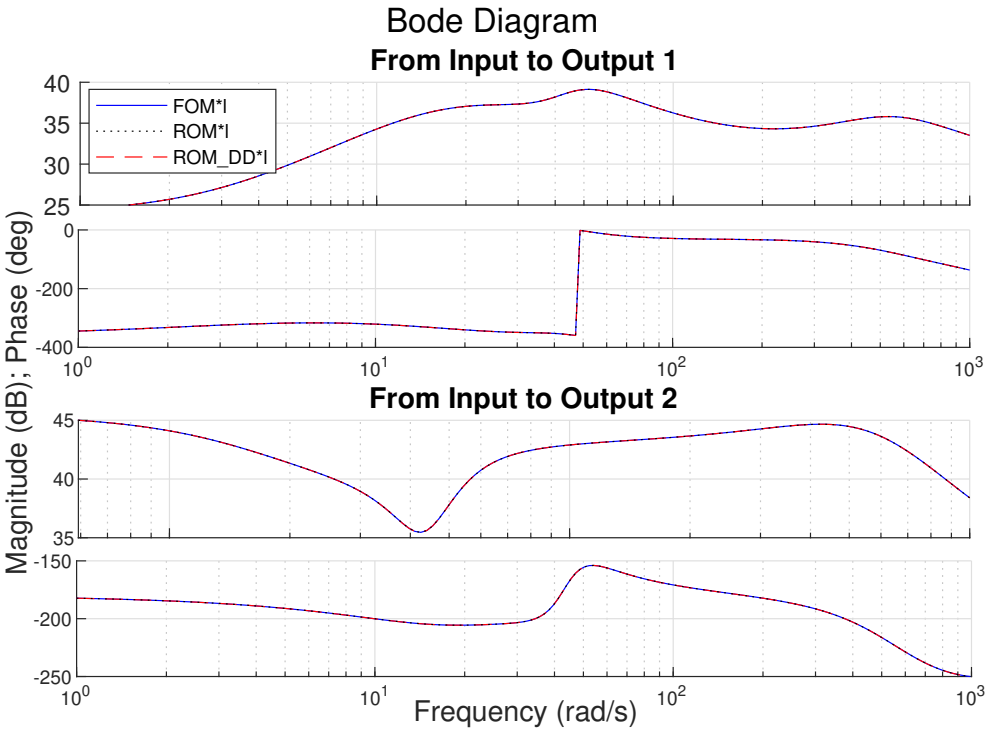

Figure 4.9: Bode plot of the right side moment-matching along the tangential direction l. The solid blue line, black dotted line and red dashed line represent the quantities for the FOM, ROM (model-based) and ROM_DD (data-driven), respectively.

4.4.3 Robustness against measurement noise

We first evaluate the robustness of Algorithm 2, compared with the non-robust method of Theorem 4.2. To this end, we add Gaussian noise to the measurements of $\varpi(t)$. We consider 20 realisations of the noise with signal-noise-ratio (SNR) of 60dB, and we estimate the quantity ΥB both by the robust (Algorithm 2) and the non-robust (Theorem 4.2) method. The average of $e_{\Upsilon B}$ over 20 realisations is denoted as $\bar{e}^r_{\Upsilon B}$ for the robust and $\bar{e}_{\Upsilon B}$ for the non-robust estimation. The corresponding average of $e_{\Upsilon\Pi}$ is denoted as $\bar{e}^r_{\Upsilon\Pi}$ and $\bar{e}_{\Upsilon\Pi}$, respectively. The robust algorithm (Algorithm 2) uses 1000 measurements, while the non-robust method (Theorem 4.2) uses only one measurement (the last). The robust estimations have small averaged errors, *i.e.* $\bar{e}^r_{\Upsilon B} = 3.2 \times 10^{-5}$

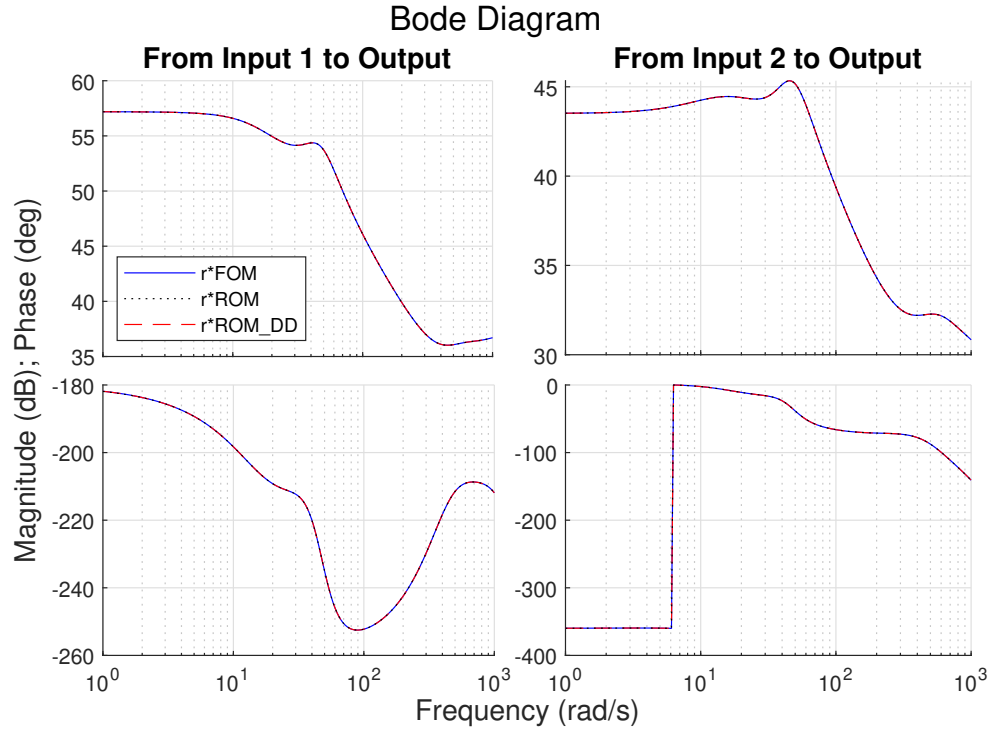

Figure 4.10: Bode plot of the left side moment-matching along the tangential direction r. The solid blue line, black dotted line and red dashed line represent the quantities for the FOM, ROM (model-based) and ROM_DD (data-driven), respectively.

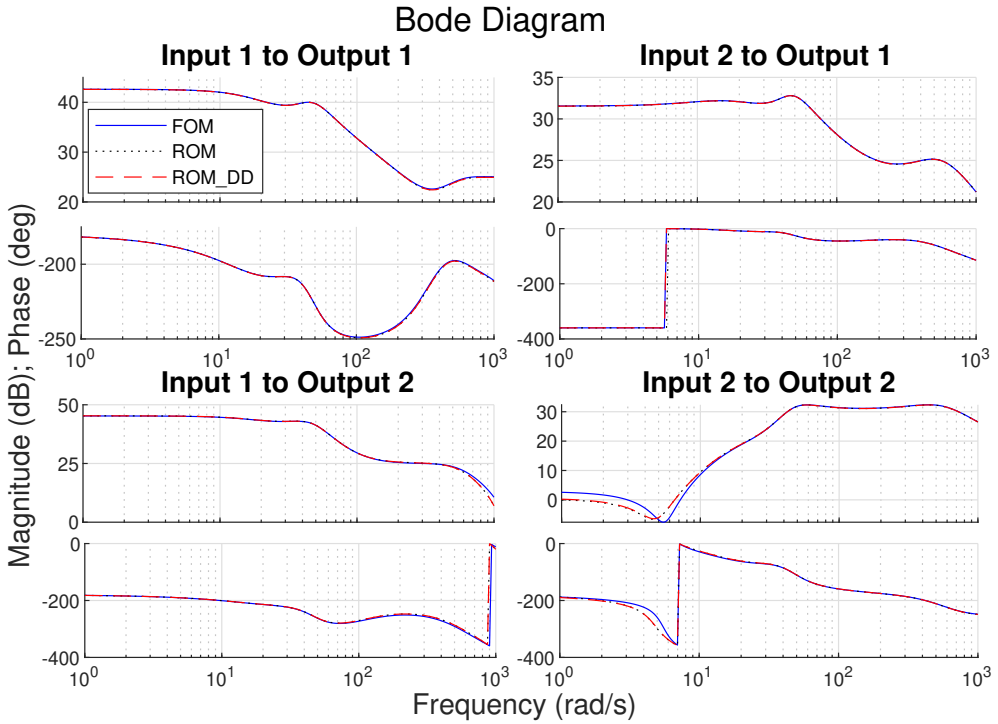

Figure 4.11: Bode plot of the FOM and ROMs. The solid blue line, black dotted line and red dashed line represent the FOM, ROM (model-based) and ROM_DD (data-driven), respectively.

and $\bar{e}^r_{\Upsilon\Pi} = 5.3 \times 10^{-5}$, while the non-robust estimations present averaged errors two orders of magnitude higher, namely $\bar{e}_{\Upsilon B} = 1.0 \times 10^{-3}$ and $\bar{e}_{\Upsilon\Pi} = 1.4 \times 10^{-3}$, respectively. Fig. 4.13 shows the regions between the upper and lower envelopes of all obtained magnitude plots of the ROMs obtained for the 20 realisations of the noise. In particular, the red regions refer to the robust estimation (Algorithm 2), the blue regions refer to the non-robust estimation (Theorem 4.2) and the brown dashed lines represent the ideal estimation (no noise). This figure confirms that the proposed data-driven algorithm (Algorithm 2) is robust with respect to measurement noise as, for $\widetilde{q}$ sufficiently large, the red regions are not only significantly smaller than the blue regions, but they are also close to the ideal case. We also evaluate the robustness of Algorithm 1 in Fig. 4.12, by adding noise to $y(t)$ and estimating $C\Pi$ with small or sufficiently large $\widetilde{\nu}$.

The same analysis has been carried out to study the robustness of Algorithm 1 and Algorithm 2 under a larger level of noise. Fig. 4.14 and Fig. 4.15 present the performances of Algorithm 1 and Algorithm 2 under the noise with SNR of 40dB. In particular, the red regions refer to the estimation with sufficient measurements ($\widetilde{\nu} = 1000$ or $\widetilde{q} = 1000$), the blue regions refer to the estimation with limited measurements ($\widetilde{\nu} = 30$ or $\widetilde{q} = 1$) and the brown dashed lines represent the ideal estimation (no noise). All figures confirm that the data-driven method is robust to the measurement noise.

4.4.4 Initial validation: stability and PCC voltage

In the two-sided approach, one free parameter G is used to double the number of interpolation points (See Section 4.2.3 and (4.10)). We select the interpolation points (encoded by S) and tangential directions L such that the ROM is stable. For further validation, we first compare the eigenvalues of the ROM and FOM and then we reconnect them with the study area to compare the PCC voltage. In Fig. 4.16, the eigenvalues of the FOM are represented by blue stars while the eigenvalues of the ROM obtained by the data-driven MOR method are illustrated by hollow red circles. The figure shows that the obtained ROM is stable and that the eigenvalues of the ROM have a similar

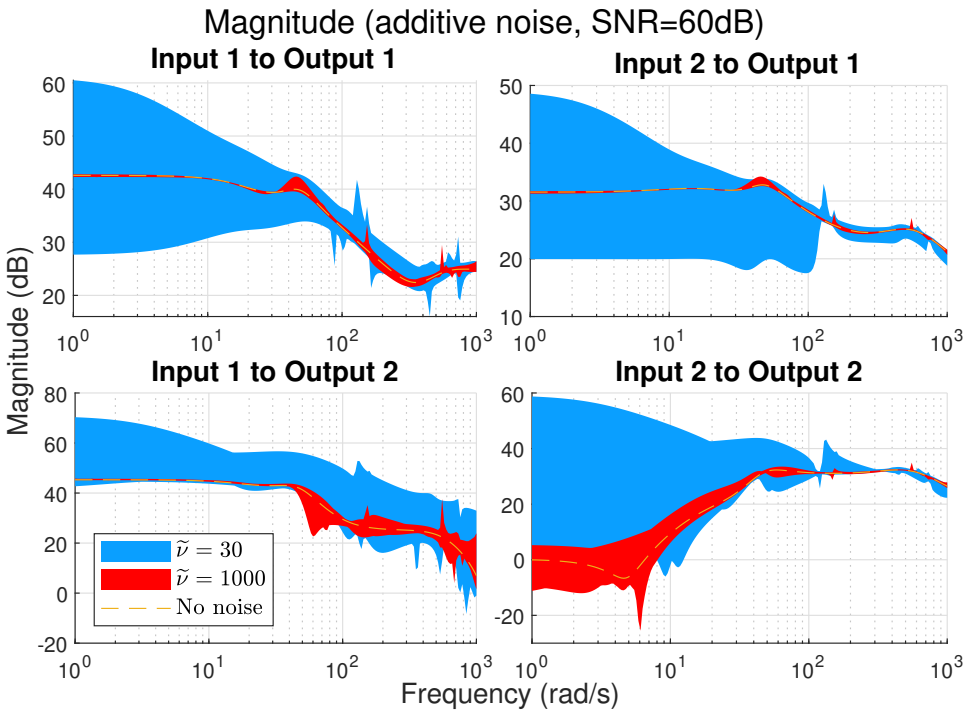

Figure 4.12: Magnitude plots of the reduced-order models under 20 realizations of additive Gaussian noise. The red regions, blue regions and brown dashed lines refer to the estimation with 1000 measurements (Algorithm 1, $\widetilde{\nu} = 1000$), estimation with 30 measurements (Algorithm 1, $\widetilde{\nu} = 30$) and the ideal estimation (no noise), respectively.

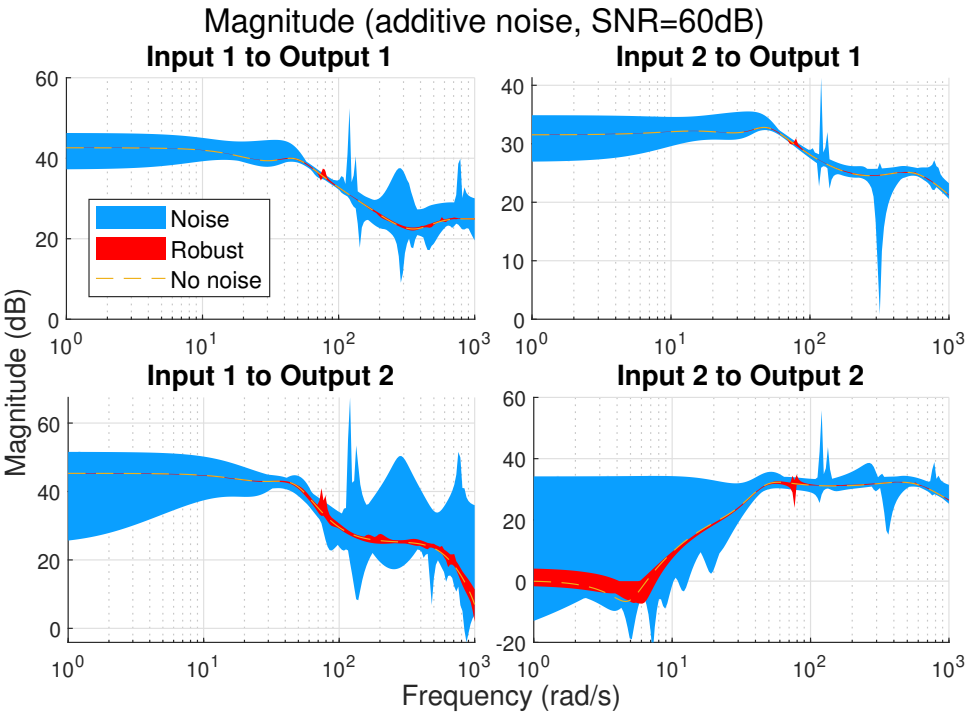

Figure 4.13: Magnitude plots of the reduced-order models under 20 realizations of additive Gaussian noise. The red regions, blue regions and brown dashed lines refer to the robust algorithm (Algorithm 2), non-robust method (Theorem 4.2) and the ideal estimation (no noise), respectively.

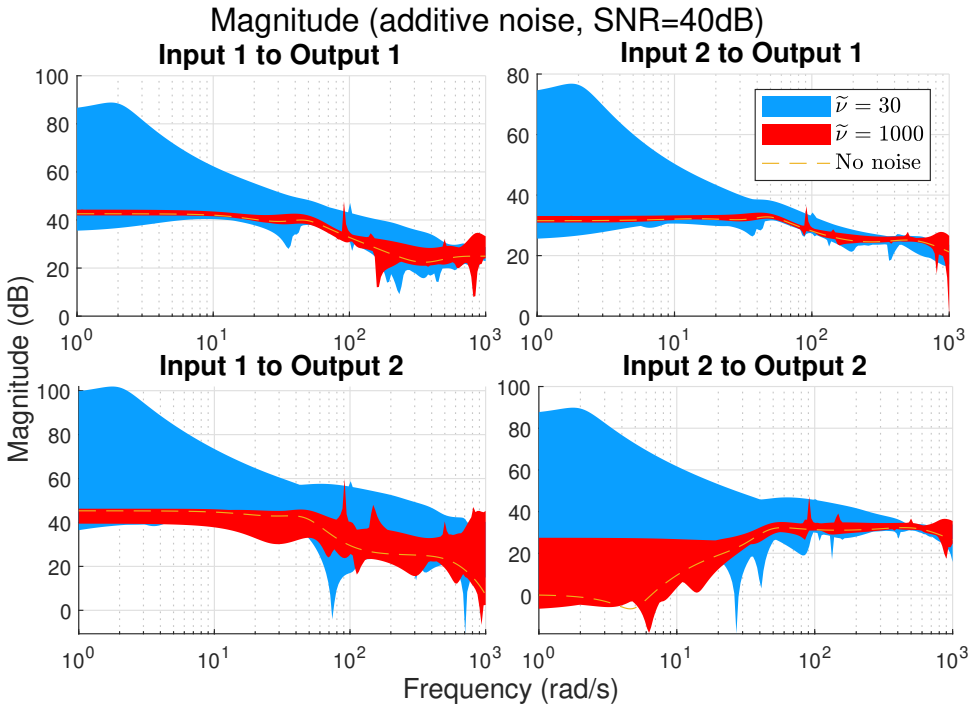

Figure 4.14: Magnitude plots of the reduced-order models under 20 realizations of additive Gaussian noise. The red regions, blue regions and brown dashed lines refer to the estimation with 1000 measurements (Algorithm 1, $\widetilde{\nu} = 1000$), estimation with 30 measurements (Algorithm 1, $\widetilde{\nu} = 30$) and the ideal estimation (no noise), respectively.

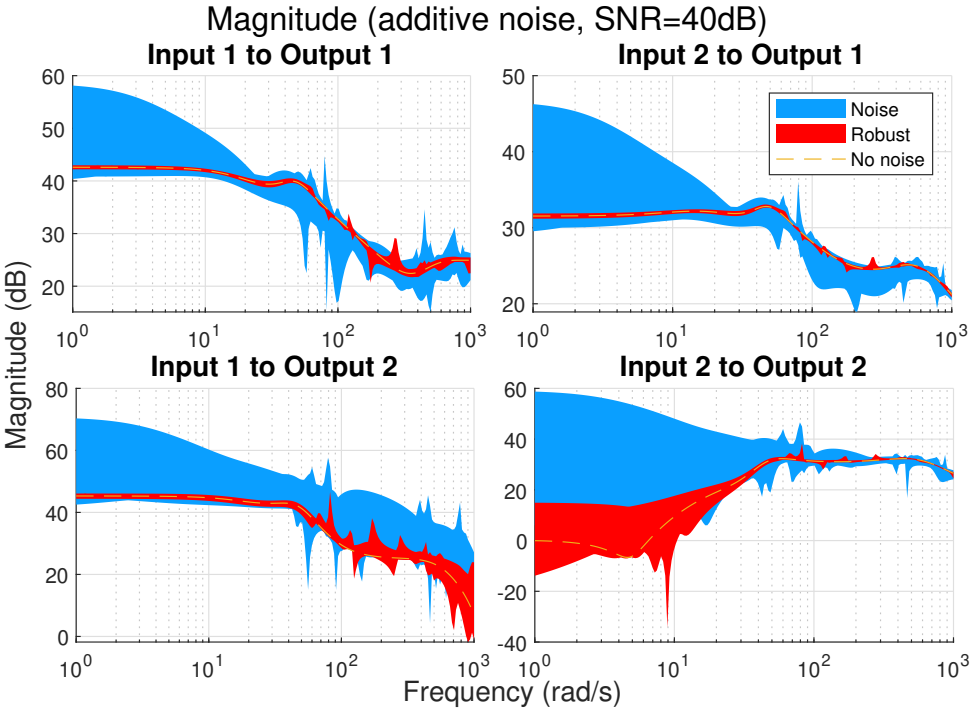

Figure 4.15: Magnitude plots of the reduced-order models under 20 realizations of additive Gaussian noise. The red regions, blue regions and brown dashed lines refer to the robust algorithm (Algorithm 2), non-robust method (Theorem 4.2) and the ideal estimation (no noise), respectively.

spread as those of the FOM. Fig. 4.17 compares the PCC voltage of the FOM and ROM when they are reconnected to the study area. The top plot shows the PCC voltages in per-unit (with $V_{base} = 66\text{kV}$), whereas the bottom plot shows the relative error in percentage. The relative error of the PCC voltage decreases to less than 0.3% within $0.1s$. Hence, the simulations confirm that the ROM can accurately recover the performance of the FOM in a short time.

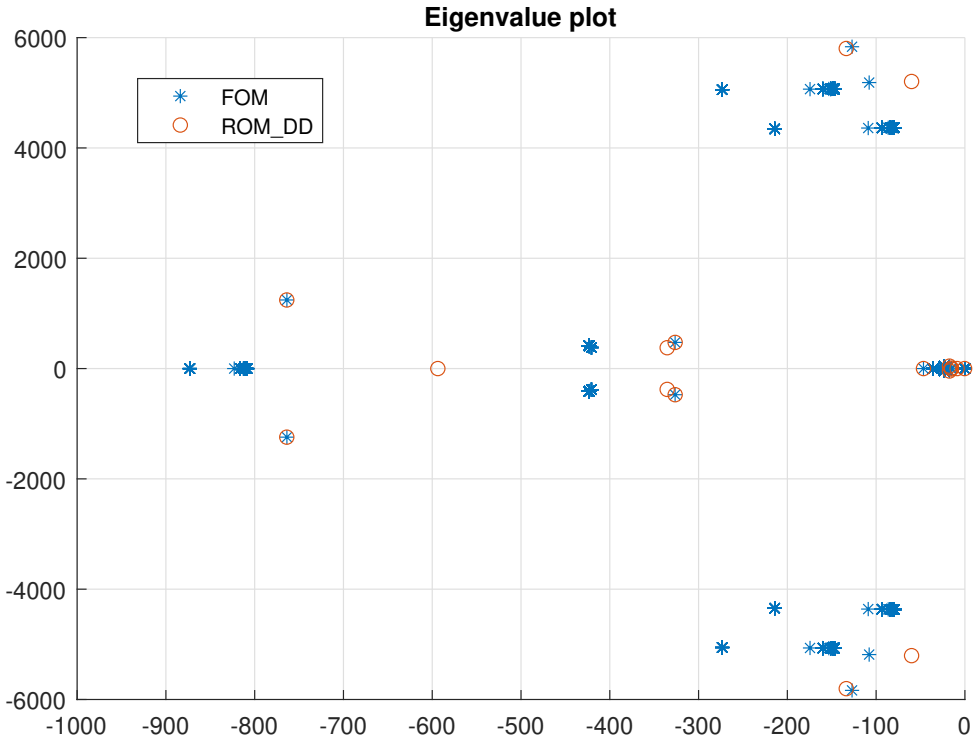

Figure 4.16: Eigenvalues of the FOM and ROM_DD (data-driven), represented by the blue stars and hollow red circles, respectively.

4.4.5 Comparison of computational time

In order to evaluate the advantages of the data-driven MOR approach proposed in this chapter, we compare the computational time of four wind farm models: 1) the nonlinear FOM (of the external area), 2) its linearisation, 3) the ROM constructed by solving the Sylvester equation (*i.e.* model-based method) and 4) the ROM constructed by the proposed data-driven approach. In addition, to show that the proposed data-driven method is advantageous in the synthetic data scenario, we compare also the "extraction

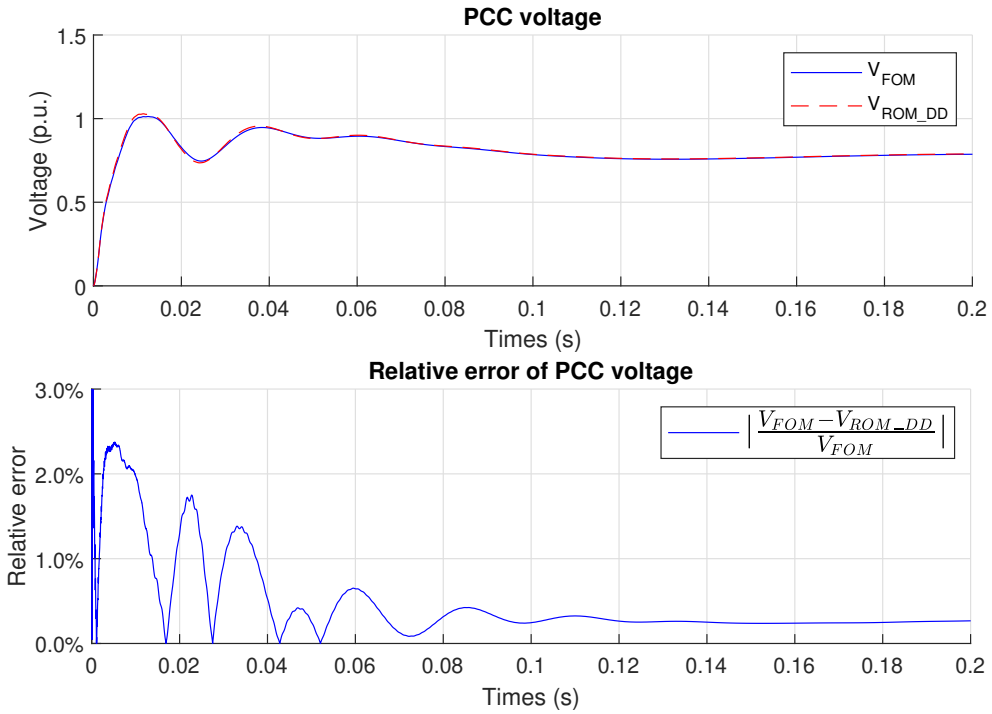

Figure 4.17: Top: PCC voltage of the FOM and ROM_DD (data-driven), represented by solid blue and dashed red lines, respectively. Bottom: corresponding relative error.

time" of the MOR (that is, the time required to construct the ROM) for the data-driven method and the model-based method. Recall that the FOM of the wind farm has order 3402. The two ROMs have order 20.

Table 4.1 compares the computational time of the four models in terms of "extraction time" of the MOR and "elapsed time" of a 1 second simulation of the wind farm. All the simulations and MOR algorithms are run in Matlab/Simulink R2023b on the same personal laptop (Windows 10, Intel Core i7-10750H and 16GB RAM). The table shows that to perform a simulation of 1 second, the nonlinear FOM requires 1268.26 seconds (about 21 minutes), whereas the linearised FOM requires 796.31 seconds (about 13 minutes), which is time-consuming. By reducing the order of the model from 3402 to 20, the elapsed time is significantly reduced to around 1.5 seconds for both the model-based ROM and the data-driven ROM. While the elapsed time of the two ROMs is similar, the two methods show a stark difference in the extraction time, which reflects the computational complexity of the MOR methods. In fact, to construct a ROM of order 20 using a model-based approach requires 28.60 seconds, whereas using the data-driven

method takes only 0.10 seconds. In summary, a simulation using the data-driven ROM is 530 times faster than a simulation using the linearised FOM, and this model is 280 times faster to construct than a model-based ROM. Note that the difference in extraction time can be justified theoretically and is independent of the specific model-based method used. In fact, any model-based ROM method operates on the matrices A, B, C which have order n, whereas the proposed algorithms have computational complexity that is independent of n and depends only on ν. As $\nu \ll n$, the proposed method is faster.

Table 4.1: Computational comparison

Model	Order	Extraction time	Elapsed time
FOM (nonlinear)	3402	-	1268.26s
FOM (linear)	3402	-	796.31s
ROM	20	28.60s	1.53s
ROM_DD	20	0.10s	1.52s

4.4.6 Advanced validation: fault behaviour

Further validation is provided by means of fault simulations. Two fault scenarios are considered:

- 1) A self-clearing fault at bus 14 of the study area occurring at $t = 0.3$s and cleared after 50ms.
- 2) A fault at bus 8 of the study area occurring at $t = 0.3$s. After 100ms bus 8 is disconnected to protect the rest of the power system.

All the faults are produced by the 'Three-Phase Fault' block in the Simulink.

In this section, we reconnect the external area to the study area to verify if the ROM of the external area behaves well not just in isolation, but in the realistic case in which this is interconnected to the rest of the power system. For both cases, the PCC voltage is presented in per-unit (with $V_{base} = 66$kV) while the corresponding relative error is shown in percentage.

Case study 1 (Self-clearing fault)

A fault occurs at bus 14 of the power system at $t = 0.3$s and is cleared at $t = 0.35$s. The PCC voltage drops by 19.43% and recovers within 0.15s after the fault is cleared. The top of Fig. 4.18 shows the PCC voltage of the study area when it is reconnected to the FOM (solid blue lines) and the ROM (dashed red lines) respectively. The PCC voltage of the two models is almost indistinguishable when the bus 14 experiences the fault. The bottom of Fig. 4.18 shows the respective relative errors (in percentage). The largest relative error occurs in the transient period after the PCC voltage drops or steps (*i.e.* t = 0.32s and $t = 0.36s$). These peak errors are small (0.72% and 0.84%) and decrease to less than 0.4% within $0.1s$. We conclude that when a self-clearing fault occurs at the bus of the power system, the influence on the PCC voltage is recovered precisely by the ROM. Thus, the fault behaviour is fully preserved by the data-driven MOR approach.

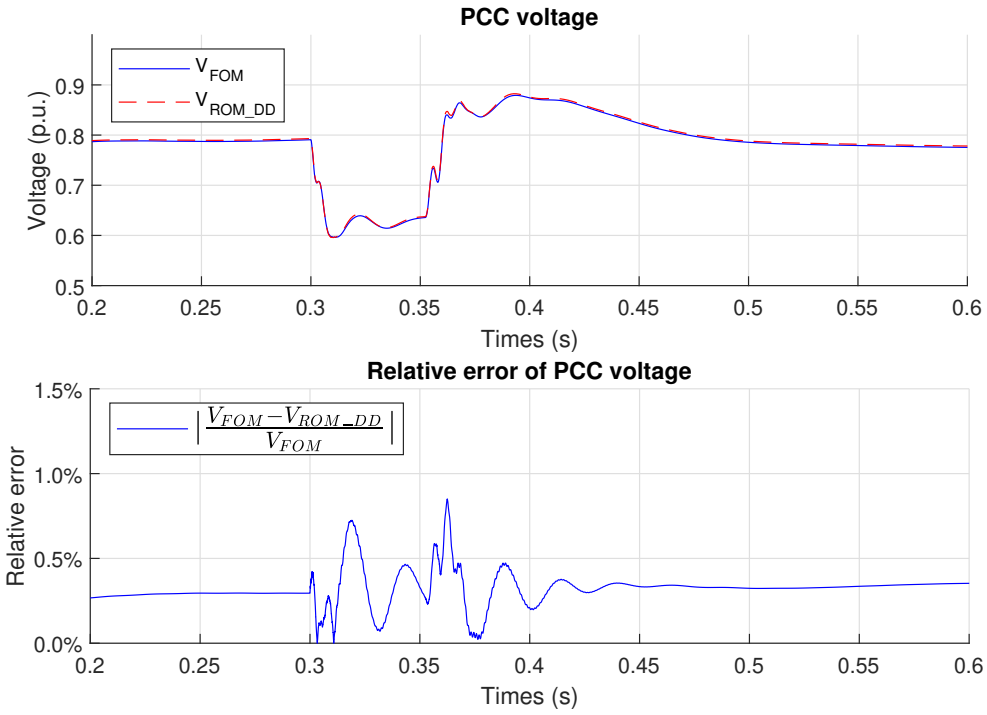

Figure 4.18: Top: PCC voltage of the FOM and ROM_DD (data-driven), represented by solid blue and dashed red lines, respectively. Bottom: corresponding relative error.

Case study 2 (Not self-clearing fault)

A fault occurs at bus 8 of the power system at $t = 0.3$s and cannot be cleared. Bus 8 is disconnected at $t = 0.4$s to protect the rest of the power system. This fault results in a voltage drop of 28.04% at the PCC. The top of Fig. 4.19 shows the PCC voltage of the combined system of the study area and the FOM (solid blue lines) or ROM (dashed red lines), respectively. The bottom of Fig. 4.19 shows the corresponding relative errors of the PCC voltage with a peak of 1.22% at $t = 0.41$s and decreasing to less than 0.5% within $0.1s$. Since this fault cannot be self-cleared, it is isolated by disconnecting bus 8. Missing the generator at bus 8, the PCC voltage cannot recover and decreases to a smaller value of 0.73pu. This behavior is fully captured by the use of the ROM in place of the FOM.

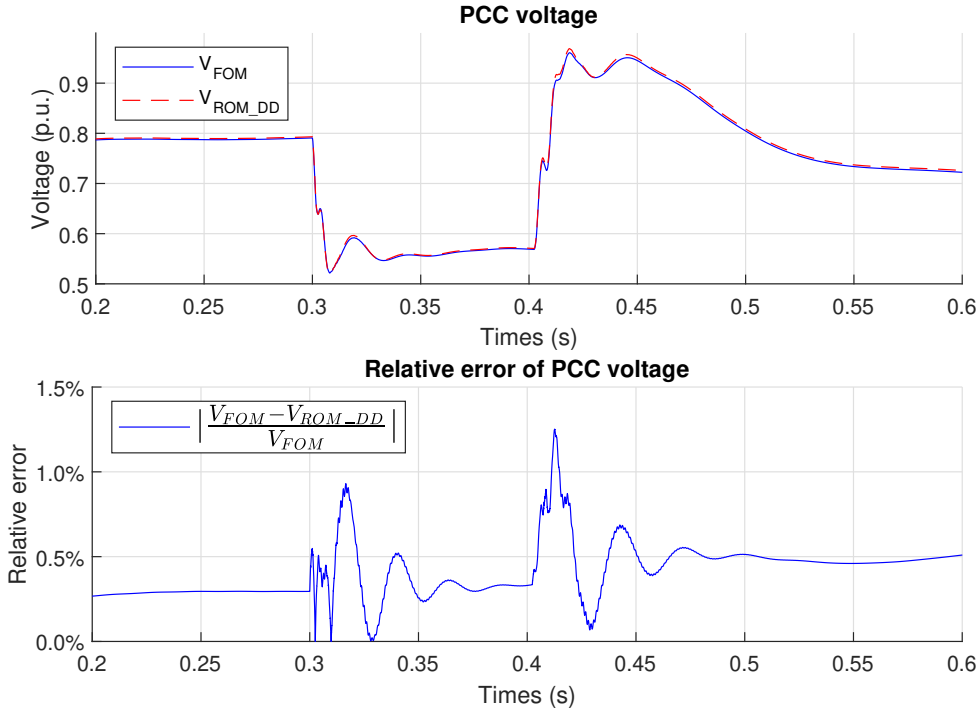

Figure 4.19: Top: PCC voltage of the FOM and ROM_DD (data-driven), represented by solid blue and dashed red lines, respectively. Bottom: corresponding relative error.

Combining all the simulation results presented in this section, we conclude that by reducing the external area from a complicated FOM to a simple ROM, we considerably reduce the elapsed time of simulations while maintaining high fidelity across a range of

different criteria. In addition, the proposed method is robust to measurement noise, it is completely model free and has the advantage of low computational complexity (*i.e.* small extraction time) even in the synthetic data scenario.

4.5 Conclusion

We have presented a data-driven algorithm for the MOR of large-scale wind farms. We presented algorithms to achieve two-sided moment-matching for MIMO systems. Unlike other MOR approaches that require full information of the system matrices, the proposed data-driven algorithm is model free, robust to measurement noise and offers low computational complexity to practically overcome the challenges posed by large-scale wind farm. Finally, we have provided extensive simulations that validate the proposed method on a combined model of a 200-turbine wind farm interconnected to the IEEE 14-bus system in terms of Bode plot, eigenvalues, PCC voltage and fault behaviour.

Part II

Control

Chapter 5

Approximate Solutions to Classes of State-Feedback Control Problems for Stochastic Nonlinear Systems

5.1 Introduction

In this chapter, we propose constructive approximate solutions for three strongly related stochastic nonlinear control problems: the infinite-horizon optimal control problem, the $\mathcal{H}_\infty$ control problem and the min-max zero-sum two-player game. Optimal control concerns the design of control laws to achieve certain objectives - described in terms of a cost functional - in an optimal manner, see *e.g.* [93] (for the deterministic formulation) and [94] (for the stochastic formulation). The $\mathcal{H}_\infty$ control problem instead concerns the design of control laws that ensure that the $\mathcal{L}_2$ gain (from an exogenous input/disturbance to the output of the system) is bounded (from above) by a given attenuation factor, see *e.g.* [95] (deterministic) and [96] (stochastic). The latter problem is closely related to the min-max zero-sum two-player game, see *e.g.* [97] (deterministic) and [98] (stochastic). It is well-known that the solutions to these problems can be found by solving second-order stochastic partial differential equations (PDEs) or inequalities

which are referred to as the *Hamilton-Jacobi-Bellman (HJB)* equations or inequalities (see, *e.g.* [94]). Practically, a major obstacle associated with implementing such solutions is that solving HJB equations or inequalities is very challenging, see *e.g.* [94]. Some methods have been proposed based on successively approximating the HJB equation by a sequence of *Generalized-Hamilton-Jacobi-Bellman (GHJB)* equations, see *e.g.* [99] (for deterministic systems) and [100] (for stochastic). These GHJB equations are linear PDEs, which can be solved by Galerkin approximation method but suffer from the curse of dimensionality. An alternative approach where neural networks are employed to approximate the GHJB solution was proposed in [101] for discrete-time stochastic systems. Alternatively, [102] exploited the dynamic programming principle to numerically approximate the viscosity solutions in high-order schemes. For deterministic systems a family of concepts have been introduced to solve nonlinear control problems without requiring the solution of any PDE (see [103] and references therein). In [104, 105] optimal control and $\mathcal{L}_2$ disturbance attenuation is considered. Results therein have been extended to constrained optimal control in [106], optimal control and disturbance attenuation via measurement feedback in [107, 108], mixed $\mathcal{H}_2/\mathcal{H}_\infty$ control in [109] and differential games in [110]. Currently, these methods are not available for stochastic systems, which have an additional challenge that the HJB equation is of second order. In this chapter, we propose a systematic method for constructing *approximate* solutions to the infinite-horizon optimal control problem and the infinite-horizon min-max zero-sum two-player game, as well as *exact* solutions to the $\mathcal{H}_\infty$ control problem for *stochastic* systems. The method requires only the solution of an *algebraic* equation in place of the HJB *partial differential* equation. The resulting controller is nonlinear, does not require the solution of PDEs and has better performance than the control laws stemming from the associated linear quadratic approximations and deterministic nonlinear approaches. In the context of optimal control and min-max zero-sum differential games, the level of approximation can be interpreted as an exactly quantifiable *additional cost/reward*. Several important differences between the deterministic and the stochastic settings are highlighted. We also discuss how the proposed method can be extended to more general

classes of control problems, such as nonzero-sum differential games, see *e.g.* [111]. The chapter is concluded by extensive simulations demonstrating the efficacy of the proposed approach. A preliminary version of this work has been published in [112]. The novel contributions of this chapter are: the study and solution of the $\mathcal{H}_\infty$ control problem; the min-max zero-sum two-player game; all the proofs of the results; all technical remarks; extensive numerical simulations and the accompanying comparison with the stochastic linear and deterministic nonlinear methods.

The remainder of the chapter is organized as follows. In Section 5.2 we recall some preliminary results in the theory of stochastic systems. In Section 5.3 we define the three classes of problems. In Section 5.4 we formulate corresponding auxiliary problems which we subsequently solve. This is achieved in two steps detailed in Sections 5.5 and 5.6, respectively. Extensive numerical simulations are presented in Section 5.7. Some concluding remarks are given in Section 5.8.

5.2 Preliminary: Stochastic Differential Equations

This section briefly recalls some preliminary results on stochastic differential equations, which are fundamental for understanding the rest of the chapter. The material of this section can be found in [113].

5.2.1 Probability Space and Stochastic Process

The probability space denoted by $(\nabla, \mathcal{A}, \mathcal{P})$ consists in a set ∇ of all elementary events, a σ-algebra $\mathcal{A}$ associated with ∇, *i.e.* the set of all observable events in ∇, and a probability measure $\mathcal{P}$ on the measurable space $(\nabla, \mathcal{A})$.

In particular, the empty set $\emptyset$ and the whole set ∇ belong to $\mathcal{A}$ by definition. Furthermore, the σ-algebra $\mathcal{A}$ has the properties as follows.

- if the event A belongs to $\mathcal{A}$, then $\nabla \backslash A$ belongs to $\mathcal{A}$.
- if events A and B belong to $\mathcal{A}$, then $A \cup B$ and $A \cap B$ belong to $\mathcal{A}$.
- if events A_i, $i \geq 1$, belong to $\mathcal{A}$, then $\cup_{i=1}^{\infty} A_i$ belong to $\mathcal{A}$.

The couple $(\nabla, \mathcal{A})$ is called a measurable space. A function $Y : \nabla \to \mathbb{R}^n$ is said to be $\mathcal{A}$-measurable if $Y^{-1}(U) = \{\omega \in \nabla; Y(\omega) \in U\} \in \mathcal{A}$ for all open sets $U \subseteq \mathbb{R}^n$. The σ-algebra generated by Y is the smallest σ-algebra on ∇ containing all the sets $Y^{-1}(U)$ for any open $U \subseteq \mathbb{R}^n$.

$\mathcal{P}$ is a probability measure on the measurable space $(\nabla, \mathcal{A})$ with the properties as follows.

- $\mathcal{P}(\emptyset) = 0$.
- $\mathcal{P}(\nabla) = 1$.
- if events A_i, $i \geq 1$, belong to $\mathcal{A}$, A_i and A_j is disjoint for $i \neq j$, then $\mathcal{P}(\cup_{i=1}^{\infty} A_i) = \sum_{i=1}^{\infty} \mathcal{P}(A_i)$.

If $\mathcal{P}(A) = 1$, then we say the event A occurs *almost surely*. Unless otherwise specified, the rest of the section sets the theory in the probability space $(\nabla, \mathcal{A}, \mathcal{P})$.

A stochastic process with state space $\mathbb{R}^n$ is a family $\{x_t, t \in \mathbb{R}\}$ of $\mathbb{R}^n$-valued random variables defined on $(\nabla, \mathcal{A}, \mathcal{P})$. It can be considered equivalently as a function of two variables, namely for fixed $t \in \mathbb{R}$, the function $x_t(\cdot)$ is an $\mathbb{R}^n$-valued random variable and, for fixed $\omega \in \nabla$, the function $x.(\omega)$ is an $\mathbb{R}^n$-valued function of time. In the remainder, a stochastic process $\{x_t, t \in \mathbb{R}\}$ on $(\nabla, \mathcal{A}, \mathcal{P})$ is simply denoted by x_t for ease of notation.

5.2.2 Brownian Motion

Brownian motion, also known as the Wiener process, is a typical stochastic process commonly used in physics and finance to describe the random movement of molecules or prices. The one-dimensional Brownian motion is a continuous-time stochastic process with the following properties.

- $\mathcal{W}_0 = 0$.
- $\mathcal{W}t$ is a Gaussian random variable with an expected value of zero and variance t.
- Given with a time sequence $t_1 < t_2 \cdots < t_k$, the increments $\mathcal{W}_{t_2} - \mathcal{W}_{t_1}$, $\mathcal{W}_{t_3} - \mathcal{W}_{t_2}$, $\cdots$, $\mathcal{W}_{t_k} - \mathcal{W}_{t_{k-1}}$ are independent random variables.
- The realisation $\mathcal{W}_t(w)$ is continuous for almost all $w \in \nabla$.

Note that even if almost all paths of the Brownian motion are continuous, they are nowhere differentiable.

5.2.3 Stochastic Differential Equations

A general stochastic differential equation is given by

$$dx_t = f(t, x_t)dt + h(t, x_t)d\mathcal{W}_t, \qquad x_0 = c, \qquad 0 \leq t \leq T \leq \infty, \tag{5.1}$$

where $x_t \in \mathbb{R}^n$, $f : [0, T] \times \mathbb{R}^n \to \mathbb{R}^n$ and $h : [0, T] \times \mathbb{R}^n \to \mathbb{R}^n$ are measurable on $[0, T] \times \mathbb{R}^n$, the random variable c is the initial value at time zero and $\mathcal{W}_t$ is the one-dimensional Brownian motion. The term $f(t, x_t)dt$ is called drift term while the term $h(t, x_t)dt$ is called diffusion term.

We assume that the general stochastic differential equation (5.1) describes the dynamics of the state of a stochastic system with $T = \infty$. Before we introduce the notions of stability, we make some standard assumptions as follows.

- The existence and uniqueness of the solution of (5.1).
- The initial condition c is a constant with probability 1.
- $f(t,0) \equiv l(t,0) \equiv 0$ implies that $x_t \equiv 0$. The unique solution of (5.1) with $c = 0$ is the origin.

Finally, we are ready to recall different notions of the stability of stochastic systems given by [114], namely the almost sure stability and almost sure asymptotic stability.

Definition 5.1. The zero equilibrium point of system (5.1) is said to be *stable almost surely* if

$$\mathcal{P}(\lim_{c\to 0} \sup_{0\leq t\leq \infty} |x_t| = 0) = 1.$$

Definition 5.2. The zero equilibrium point of system (5.1) is said to be *asymptotically stable almost surely*, if it is stable almost surely and there exists $\delta' > 0$ such that $|c| < \delta'$ implies for any $\epsilon > 0$

$$\lim_{\delta\to\infty} \mathcal{P}(\sup_{t\geq\delta} |x_t| > \epsilon) = 0.$$

5.3 Preliminaries: Three Classes of Problems

In this section we recall three classes of control problems, namely the infinite-horizon optimal control problem, the $\mathcal{H}_\infty$ control problem and the min-max zero-sum two-player game. The three problems are formulated in order to highlight their similarities, which are then exploited to develop a unique method for constructing their (approximate) solutions.

5.3.1 Infinite-Horizon Optimal Control

Consider a stochastic nonlinear input-affine system described by the equations

$$dx_t = [f(x_t) + g(x_t)u]dt + [h(x_t) + l(x_t)u]d\,\mathcal{W}_t, \tag{5.2}$$

with state $x_t \in \mathbb{R}^n$ and input $u(t) \in \mathbb{R}^m$. Assume that $f : \mathbb{R}^n \to \mathbb{R}^n$, $g : \mathbb{R}^n \to \mathbb{R}^{n\times m}$, $h : \mathbb{R}^n \to \mathbb{R}^n$ and $l : \mathbb{R}^n \to \mathbb{R}^{n\times m}$ are smooth mappings and that the initial value problem associated with (5.2) has a unique solution[1]. Moreover, assume that the origin is an equilibrium point of (5.2), *i.e.* $f(0) = 0$ and $h(0) = 0$. The infinite-horizon optimal control problem can be formulated as follows.

Problem 5.1. The *infinite-horizon optimal control problem* consists in finding a control u that minimizes the cost functional[2]

$$J(x_0, u) = E\left\{\int_0^\infty \frac{1}{2}\left[q(x_t) + r(x_t, u(t))\right] dt\right\}, \tag{5.3}$$

where[3] $q = x_t^\top Q(x_t)x_t$, with $Q = Q^\top$ such that $Q : \mathbb{R}^n \to \mathbb{R}^{n\times n}_{>0}$, and $r = u^\top R(x_t)u$, with $R = R^\top$ such that $R : \mathbb{R}^n \to \mathbb{R}^{m\times m}$, subject to the constraint (5.2). Moreover, $u(t) \in U \subset \mathbb{R}^m$, with U compact, needs to be such that the zero equilibrium of the closed-loop system is locally asymptotically stable almost surely.

Note that R does not have to be a positive definite function (see, *e.g.* [94, 117]). A solution to Problem 5.1, when it exists, can be determined by solving the HJB PDE

$$\begin{aligned}\min_u \Bigg\{ &\frac{1}{2}h^\top V_{xx} h \;+h^\top V_{xx} l u + \frac{1}{2}u^\top l^\top V_{xx} l u \\ &+V_x f + V_x g u + \frac{1}{2}q + \frac{1}{2}u^\top R u\Bigg\} = 0,\end{aligned} \tag{5.4}$$

where $V : \mathbb{R}^n \to \mathbb{R}$ is the value function of the optimal control problem, *i.e.* it satisfies the relation

$$V(x_0) = \min_u J(x_0, u). \tag{5.5}$$

[1] A sufficient condition for system (5.2) to have a unique global solution is that the mappings satisfy a Lipschitz condition, see [115, Corollary 6.3.5].

[2] Different definitions of the cost functional exist for infinite-horizon stochastic optimal control problems. Since we are interested in closed-loop asymptotic stability we have chosen a classical definition given in *e.g.* [98, 116]. If close-loop stability is not of interest, then an alternative choice could include a discount factor.

[3] The assumption that q is positive definite can be relaxed: if q is positive semidefinite the results of the chapter hold assuming that system (5.2) with output $y_t = q(x)$ is zero-state detectable.

If the value function is known, then the optimal control is given by, see *e.g.* [94],

$$u^* = -\left(R + l^\top V_{xx} l\right)^{-1} \left(g^\top V_x^\top + l^\top V_{xx} h\right). \tag{5.6}$$

Substituting $u = u^*$ into the HJB equation (5.4) yields

$$\begin{aligned} 0 \;&=\; h^\top V_{xx} h + 2V_x f + q \\ &-\; \left(V_x g + h^\top V_{xx} l\right)\left(R + l^\top V_{xx} l\right)^{-1}\left(g^\top V_x^\top + l^\top V_{xx} h\right). \end{aligned} \tag{5.7}$$

If one is able to find a function V satisfying the second-order PDE (5.7), then the control (5.6) solves Problem 5.1. Note that, as a consequence of this discussion, a necessary condition for the solution of the infinite-horizon optimal control problem is that $R(x_t) + l(x_t)^\top V_{xx}(x_t) l(x_t)$ is invertible at least for every point of the optimal trajectory of (5.2) generated under u^*. While this is guaranteed if R is positive definite (similarly to the deterministic case), as already pointed out the positive definiteness of R is not required in general (see [94]).

In practice, the main drawback associated with the optimal control (5.6) is that it is very challenging to find a solution to the second-order PDE (5.7).

5.3.2 $\mathcal{H}_\infty$ Control and Min-Max Zero-Sum Two-Player Game

Consider now an augmentation of system (5.8), namely

$$\begin{aligned} dx_t \;&=\; [f(x_t) + g(x_t)u + \varphi(x_t)\,\mathsf{d}]dt \\ &+\; [h(x_t) + l(x_t)u + \vartheta(x_t)\,\mathsf{d}]d\mathcal{W}_t, \\ y_t \;&=\; \begin{bmatrix} p(x_t)^\top & u^\top \end{bmatrix}^\top, \end{aligned} \tag{5.8}$$

where $\mathsf{d}(t) \in \mathbb{R}^r$ is a disturbance with well-defined $\mathcal{L}_2$-gain and $\varphi : \mathbb{R}^n \to \mathbb{R}^{n\times r}$, $\vartheta : \mathbb{R}^n \to \mathbb{R}^{n\times r}$ and $p : \mathbb{R}^n \to \mathbb{R}^q$ are smooth mappings. Again, we assume uniqueness of the solution of (5.8). Since in the following $p(x_t)^\top p(x_t)$ plays the same role that

$q(x_t)$ had in the previous section, we set $p(x_t)^\top p(x_t) = q(x_t)$ for notational simplicity. The remaining quantities have the same meaning given in previous section. The $\mathcal{L}_2$ attenuation/$\mathcal{H}_\infty$ control problem can be formulated as follows.

Problem 5.2. Given a real number $0 < \mu < 1$, the *regional* $\mathcal{L}_2$ *attenuation problem*, also known as *regional* $\mathcal{H}_\infty$ *control problem*, consists in determining a control u and a region $\bar{\Omega} \subset \mathbb{R}^n$ containing the origin of $\mathbb{R}^n$ such that

$$E\left\{\int_0^\infty ||y_t||^2 dt\right\} \leq E\left\{\mu^2 \int_0^\infty ||\,\mathsf{d}(t)||^2 dt\right\} \tag{5.9}$$

holds for every d and every trajectory of the system that remains in $\bar{\Omega}$. Moreover, $u(t) \in U \subset \mathbb{R}^m$, with U compact, needs to be such that the zero equilibrium of the closed-loop system is locally asymptotically stable almost surely.

It is well-known that the solution of this problem can be found by interpreting Problem 5.2 as a relaxation of a min-max zero-sum two-player game, see [97] (and [98] for the stochastic formulation). In particular, consider the problem of finding u which solves

$$\min_u \max_{\mathsf{d}} J_{\mathcal{L}_2}(x_0, u, \mathsf{d}), \tag{5.10}$$

with $J_{\mathcal{L}_2}(x_0, u, \mathsf{d}) = E\left\{\int_0^\infty \frac{1}{2}\left[||y_t||^2 - \mu^2||\,\mathsf{d}(t)||^2\right] dt\right\}$. In this framework, the "player" u seeks to minimize a cost, whereas the "player" d seeks to maximize a reward. Locally around the origin, the cost $J_{\mathcal{L}_2}(0, 0, \mathsf{d})$ is, by construction, non-positive for any d. Thus, the solution of the min-max problem solves the regional $\mathcal{L}_2$ attenuation problem by setting $\bar{\Omega}$ as the neighborhood of the origin for which the cost is negative. The solution of (5.10), when it exists, can be determined by solving the HJB PDE

$$\begin{aligned}\min_u \max_{\mathsf{d}} \Big\{ & \frac{1}{2}q + \frac{1}{2}u^\top u - \frac{1}{2}\mu^2\,\mathsf{d}^\top\,\mathsf{d} + \frac{1}{2}h^\top V_{xx} h \\ & + h^\top V_{xx}(lu + \vartheta\,\mathsf{d}) + \frac{1}{2}(u^\top l^\top + \mathsf{d}^\top\,\vartheta^\top) V_{xx}(lu + \vartheta\,\mathsf{d}) \\ & + V_x f + V_x(gu + \varphi\,\mathsf{d})\Big\} = 0,\end{aligned} \tag{5.11}$$

where $V : \mathbb{R}^n \to \mathbb{R}$ is the value function of the min-max zero-sum two-player game, *i.e.*

it satisfies the relation $V(x_0) = \min_u \max_{\mathsf{d}} J_{\mathcal{L}_2}(x_0, u, \mathsf{d})$. If the value function is known, then the optimal policies are given by

$$\begin{bmatrix} u^* \\ \mathsf{d}^* \end{bmatrix} = \begin{bmatrix} I + l^\top V_{xx} l & l^\top V_{xx} \vartheta \\ \vartheta^\top V_{xx} l & \vartheta^\top V_{xx} \vartheta - \mu^2 \end{bmatrix}^{-1} \begin{bmatrix} -g^\top V_x^\top - l^\top V_{xx} h \\ -\varphi^\top V_x^\top - \vartheta^\top V_{xx} h \end{bmatrix}. \tag{5.12}$$

Let

$$\widetilde{u}^* = \begin{bmatrix} u^* \\ \mathsf{d}^* \end{bmatrix}, \quad \begin{matrix} \widetilde{g} \\ \widetilde{l} \end{matrix} = \begin{bmatrix} g & \varphi \\ l & \vartheta \end{bmatrix}, \quad \widetilde{R} = \begin{bmatrix} I & 0 \\ 0 & -\mu^2 \end{bmatrix}. \tag{5.13}$$

Then the optimal policies can be written compactly as

$$\widetilde{u}^* = -\left(\widetilde{R} + \widetilde{l}^\top V_{xx} \widetilde{l}\right)^{-1} \left(\widetilde{g}^\top V_x^\top + \widetilde{l}^\top V_{xx} h\right). \tag{5.14}$$

Replacing (5.14) in the HJB equation (5.11) yields

$$\begin{aligned} 0 \;&=\; h^\top V_{xx} h + 2 V_x f + q \\ &-\; \left(V_x \widetilde{g} + h^\top V_{xx} l\right) \left(\widetilde{R} + \widetilde{l}^\top V_{xx} \widetilde{l}\right)^{-1} \left(\widetilde{g}^\top V_x^\top + \widetilde{l}^\top V_{xx} h\right). \end{aligned} \tag{5.15}$$

Recalling that the goal of the $\mathcal{H}_\infty$ control problem is to satisfy the inequality (5.9) (rather than a strict equality), it is common in the literature, see *e.g.* [95], to replace equation (5.15) with the inequality

$$\begin{aligned} 0 \;&\geq\; h^\top V_{xx} h + 2 V_x f + q \\ &-\; \left(V_x \widetilde{g} + h^\top V_{xx} l\right) \left(\widetilde{R} + \widetilde{l}^\top V_{xx} \widetilde{l}\right)^{-1} \left(\widetilde{g}^\top V_x^\top + \widetilde{l}^\top V_{xx} h\right), \end{aligned} \tag{5.16}$$

which is marginally simpler to solve. Solving this inequality still provides a solution of the $\mathcal{H}_\infty$ control problem because it corresponds to solving the min-max problem with respect to an increased cost functional that is still negative locally around the origin. Hence, if one is able to find a function V satisfying the second-order partial differential inequality (5.16), then the control (5.14) solves Problem 5.2.

In practice, the main drawback associated with the optimal policy/control (5.14) is that it is very challenging to find a solution to the second-order partial differential equation (5.15) or inequality (5.16).

Remark 5.1. The optimal control (5.14) and the HJB equation (5.15) are formally identical to the ones obtained for the infinite-horizon optimal control problem, *i.e.* (5.6) and (5.7).

Remark 5.2. The form of the output y_t of system (5.8) is taken from [95] and provides notational simplicity. However, another popular choice is to consider the output $y_t = p(x) + m(x)u$. The results of this chapter hold likewise under the "regularity" assumptions that $p(x)^\top m(x) = 0$ and $m(x)^\top m(x) = I$, see *e.g.* [118].

Given the equivalence presented in this section, in the following we do not distinguish between the $\mathcal{H}_\infty$ control problem and the min-max game anymore. Thus, we mention only the former. At the end of the chapter, we briefly comment on the role of the equality versus inequality for the interpretation of the results of the proposed method.

5.4 Formulation of the Auxiliary Problems

As a result of the previous discussion, we see that the considered three classes of control problems rely upon the solution of second-order partial differential equations or inequalities for which closed-form solutions very often are not readily available. In this chapter we systematically construct approximate solutions to these and, thereby, construct solutions of certain auxiliary problems that provide approximate (in the case of optimal control and min-max-zero-sum games) or exact (in the case of $\mathcal{H}_\infty$ control) solutions of the original problems. In this section we precisely formulate these auxiliary problems.

5.4.1 Approximate Regional Optimal Control

Before formulating the approximate optimal control problem it is instrumental to formally define the terms "dynamic control law" and "dynamic extension" which are used frequently in the remainder of the chapter.

Definition 5.3. Consider system (5.2). The function u in (5.2) is a *dynamic control law* if for some $\nu > 0$ it is described by the equations

$$\dot{\xi}_t = \alpha(x_t, \xi_t), \qquad u = \gamma(x_t, \xi_t), \tag{5.17}$$

where $\xi_t \in \mathbb{R}^\nu$ is the state of the *dynamic extension*, and $\alpha : \mathbb{R}^n \times \mathbb{R}^\nu \to \mathbb{R}^\nu$ and $\gamma : \mathbb{R}^n \times \mathbb{R}^\nu \to \mathbb{R}^m$ are smooth mappings, with $\alpha(0,0) = 0$ and $\gamma(0,0) = 0$.

The following problem is an approximation of Problem 5.1.

Problem 5.3. The *approximate regional dynamic infinite-horizon optimal control* problem consists in determining a *dynamic control law* (5.17) and a *region* $\Omega \subset \mathbb{R}^n \times \mathbb{R}^\nu$ strictly containing the origin of $\mathbb{R}^n \times \mathbb{R}^\nu$ such that the cost functional

$$\begin{aligned} &\bar{J}(x_0, \xi_0, u) = \\ &\quad = E\left\{ \int_0^\infty \left[\frac{1}{2}(q(x_t) + r(x_t, u(t))) + c(x_t, \xi_t) \right] dt \right\}, \end{aligned} \tag{5.18}$$

with $c : \mathbb{R}^n \times \mathbb{R}^\nu \to \mathbb{R}_{\geq 0}$, is minimized by the dynamic control law in the sense of

$$\bar{J}(x_0, \xi_0, \gamma) \leq \bar{J}(x_0, \xi_0, \bar{u}),$$

for all $\bar{u}$ and for all $(x_0, \xi_0) \in \Omega$ such that the trajectories of the closed-loop system remain in Ω and converge to zero almost surely, *i.e.* the zero equilibrium is locally asymptotically stable almost surely.

The relation between Problems 5.1 and 5.3 is based on two approximations. First, Problem 5.3 is a *local* version of Problem 5.1 since we want to find a solution in a region

Ω. Second, Problem 5.3 solves Problem 5.1 with respect to a modified cost functional. In particular, the running cost is increased by the *additional running cost* c which weights the state x_t of system (5.2) and the state ξ_t of the dynamic extension (5.17). The level of approximation is exactly quantified in terms of the additional running cost.

5.4.2 Regional $\mathcal{H}_\infty$ Control

If we define a positive semidefinite function $\widetilde{c}$ as the difference between zero and the value of the HJB inequality (5.16) arising in the solution of the $\mathcal{H}_\infty$ control problem, then solving the inequality (5.16) can be interpreted as solving an *equality* with respect to the additional running cost $\widetilde{c}$. In other words, this corresponds to solving (5.10) with respect to the new cost functional

$$\begin{aligned} &J_{\mathcal{L}_2}(x_0, u, \mathsf{d}) = \\ &= E\left\{\int_0^\infty \left[\frac{1}{2}(||y_t||^2 - \mu^2||\,\mathsf{d}(t)||^2) + \widetilde{c}(x(t))\right] dt\right\}, \end{aligned} \tag{5.19}$$

with $\widetilde{c}\colon \mathbb{R}^n \to \mathbb{R}_{\geq 0}$. Note that locally around the origin, also this cost is negative, thus implying (5.9). This observation highlights that in the case of the $\mathcal{H}_\infty$ control problem, Problem 5.2 is already in a form similar to the one of Problem 5.3. However, solving Problem 5.2 is still challenging because it does not include a dynamic extension that can be exploited to aid the design of the control. Thus, in the spirit of Problem 5.3 we introduce the following modified problem.

Problem 5.4. The *regional dynamic $\mathcal{H}_\infty$ control problem* consists in solving Problem 5.2 by means of the dynamic control law (5.17).

Remark 5.3. Differently from the optimal control problem in Problem 5.1, we are already in the situation of solving an inequality. Hence, we do not need to formulate an *approximate* version of Problem 5.2: a solution to Problem 5.4 is a precise solution to Problem 5.2, albeit a more conservative one because $E\left\{\int_0^\infty ||y_t||^2 dt\right\} \leq E\left\{\mu^2 \int_0^\infty (||\mathsf{d}(t)||^2 - 2\widetilde{c}(x(t))dt\right\} \leq E\left\{\mu^2 \int_0^\infty ||\mathsf{d}(t)||^2 dt\right\}$.

5.5 Step 1: Design of the algebraic solution, extended value function and control u

We solve Problems 5.3 and 5.4 in two steps. In the first step we construct the mapping γ of the dynamic control law (5.17). In the second step we design the mapping α of the dynamic extension ξ.

5.5.1 Infinite-Horizon Optimal Control

To provide a systematic method for solving Problem 5.3, it is useful first to recall the solution of the linearized problem, also known as stochastic linear quadratic regulator (LQR) see *e.g.* [94]. In particular, system (5.2) is linearized as

$$dx_t = [Ax_t + Bu]dt + [Cx_t + Du]d\mathcal{W}_t, \tag{5.20}$$

with

$$A = \left.\frac{\partial f}{\partial x_t}\right|_{x_t=0}, \quad B = g(0), \quad C = \left.\frac{\partial h}{\partial x_t}\right|_{x_t=0}, \quad D = l(0),$$

$\bar{Q} = Q(0)$ and $\bar{R} = R(0)$. It is easy to show (see *e.g.* [94, Theorem 6.1]) that the value function associated to the LQR problem is $\bar{V} = \frac{1}{2}x_t^\top \bar{P} x_t$ and that the optimal control is given by

$$u^* = -\left(\bar{R} + D^\top \bar{P} D\right)^{-1}\left(B^\top \bar{P}^\top + D^\top \bar{P} C\right) x_t, \tag{5.21}$$

where $\bar{P} = \bar{P}^\top > 0$ is the solution of the stochastic algebraic Riccati equation

$$\begin{aligned} 0 &= A^\top \bar{P} + \bar{P}A + C^\top \bar{P} C + \bar{Q} \\ &\quad -(\bar{P}B + C^\top \bar{P} D)(\bar{R} + D^\top \bar{P} D)^{-1}(B^\top \bar{P} + D^\top \bar{P} C), \\ \bar{R} &+ D^\top \bar{P} D > 0, \end{aligned} \tag{5.22}$$

which can be solved numerically as shown in, *e.g.*, [116]. One may wonder if this linear strategy (5.21) solves Problem 5.3. This is not the case. In fact, while it is true that

around zero the LQR problem approximates Problem 5.1, there is no guarantee that the difference between the cost associated with the nonlinear problem and the cost associated with the LQR problem is positive, as required by Problem 5.3, and moreover we cannot minimize this difference. Hence, the solution of Problem 5.3 needs to have "better" properties than the linear strategy resulting from the LQR approximation.

In what follows the structure of the LQR problem is used as a basis to construct a *nonlinear* value function, defined on an extended state-space, which is positive definite in a neighborhood of the origin and yields a solution to Problem 5.3. This is achieved through the definition of a so-called "algebraic $\bar{P}$ solution" (a nonlinear deformation of a linear $\bar{P}$). This forms the basis of the design of a dynamic control law which solves Problem 5.3. To this end, recall (see, *e.g.* [119]) that since we assumed that zero is an equilibrium point (*i.e.* $f(0) = 0$, $h(0) = 0$) we can always find continuous, possibly non-unique, functions $F : \mathbb{R}^n \to \mathbb{R}^{n\times n}$ and $H : \mathbb{R}^n \to \mathbb{R}^{n\times n}$ such that $f(x_t) = F(x_t)x_t$ and $h(x_t) = H(x_t)x_t$ for all $x_t \in \mathbb{R}^n$. From now on, we omit the arguments of all the mappings, namely $F(x_t)$, $H(x_t)$, $g(x_t)$, $l(x_t)$, $P(x_t)$, $Q(x_t)$ and $R(x_t)$, to simplify the notation, unless the argument is not clear from the context.

Definition 5.4. Consider system (5.2) and the cost functional (5.3). Let $\Sigma : \mathbb{R}^n \to \mathbb{R}^{n\times n}_{\geq 0}$, with $\Sigma(x_t) = \Sigma(x_t)^\top$ and $\bar{\Sigma} = \Sigma(0)$. Assume that the system

$$\begin{aligned} 0 &= F^\top P + PF + H^\top PH + Q + \Sigma \\ &\quad -(Pg + H^\top Pl)(R + l^\top Pl)^{-1}(g^\top P + l^\top PH), \\ R &+ l^\top Pl > 0, \end{aligned} \tag{5.23}$$

has a global solution $P : \mathbb{R}^n \to \mathbb{R}^{n\times n}$, with $P(x_t) = P(x_t)^\top$, such that $P(0) = \bar{P}$, where $\bar{P}$ is the solution of the stochastic algebraic Riccati equation (5.22) with $\bar{Q}$ replaced by $\bar{Q} + \bar{\Sigma}$. The solution P is said to be an *algebraic $\bar{P}$ solution*.

We stress here that, as already mentioned, the quantities in (5.23) are functions, not constant matrices.

Remark 5.4. An algebraic $\bar{P}$ solution, if it exists, is not unique and depends on the selection of both F and Σ. However, the results of this chapter hold irrespective of the choice of F and Σ. Note also that by continuity a local solution to (5.23) can always be found as long as the stochastic Riccati equation (5.22) has a solution.

Remark 5.5. While (5.7) is a *partial differential* equation, (5.23) is a (state-dependent) *algebraic* equation. Consequently solving (5.23) is much easier than solving (5.7).

In the following let $\nu = n$ and assume the existence of an algebraic $\bar{P}$ solution. Exploiting the algebraic $\bar{P}$ solution we can define the function

$$\mathcal{V}(x_t, \xi_t) := \frac{1}{2} x_t^\top P(\xi_t) x_t + \frac{1}{2} ||x_t - \xi_t||_W^2, \tag{5.24}$$

with $\xi_t \in \mathbb{R}^n$ and $W = W^\top \in \mathbb{R}^{n \times n}_{>0}$. Moreover, we also define

$$\mathcal{R}(x_t, \xi_t) := R(x_t) + l(x_t)^\top \mathcal{V}_{xx}(x_t, \xi_t) l(x_t),$$

and

$$\begin{aligned} \mathcal{HJB} := \; & q + h^\top \mathcal{V}_{xx}\, h + 2\, \mathcal{V}_x\, f + 2\, \mathcal{V}_\xi\, \alpha \\ & - \left(\mathcal{V}_x\, g + h^\top \mathcal{V}_{xx}\, l\right) \mathcal{R}^{-1} \left(g^\top \mathcal{V}_x^\top + l^\top \mathcal{V}_{xx}\, h\right). \end{aligned} \tag{5.25}$$

Then, the following result holds.

Proposition 5.1. Consider the cost functional (5.18) and the interconnection of system (5.2) with the control law (5.17). Assume that P is an algebraic $\bar{P}$ solution of (5.23) such that function (5.24) is the value function of Problem 5.3. Then the minimizing dynamic control u is given by

$$u^* = -\mathcal{R}^{-1} \left(g^\top \mathcal{V}_x^\top + l^\top \mathcal{V}_{xx}\, h\right). \tag{5.26}$$

Moreover, the additional running cost is $c = -\mathcal{HJB}$.

Proof. If function (5.24) is the value function of Problem 5.3 (we show in the next

section how to guarantee this), then it has to satisfy the HJB equation

$$\begin{aligned}\min_u \Big\{ &\frac{1}{2} h^\top \mathcal{V}_{xx}\, h + h^\top \mathcal{V}_{xx}\, lu + \frac{1}{2} u^\top l^\top \mathcal{V}_{xx}\, lu + \mathcal{V}_x\, f \\ &+ \mathcal{V}_x\, gu + \mathcal{V}_\xi\, \alpha + \frac{1}{2} q + \frac{1}{2} u^\top R u + \frac{1}{2} c \Big\} = 0.\end{aligned} \tag{5.27}$$

This follows from a direct application of the dynamic programming principle considering the cost functional (5.18) and the interconnection of system (5.2) with the control law (5.17) as specified in Problem 5.3. Straightforward computation (setting the derivative with respect to u of the argument of (5.27) equal to zero and solving the resulting equation with respect to u) shows that the minimizing dynamic control u is given by (5.26). Replacing the optimal control u^* in the HJB equation (5.27) yields

$$\begin{aligned} 0 \;&=\; c + q + h^\top \mathcal{V}_{xx}\, h + 2\, \mathcal{V}_x\, f + 2\, \mathcal{V}_\xi\, \alpha \\ &\quad - \big(\mathcal{V}_x\, g + h^\top \mathcal{V}_{xx}\, l\big)\, \mathcal{R}^{-1} \big(g^\top \mathcal{V}_x^\top + l^\top \mathcal{V}_{xx}\, h\big) \\ &=\; c + \mathcal{HJB}\,. \end{aligned} \tag{5.28}$$

Since c is positive semidefinite, it follows from (5.28) that

$$\mathcal{HJB} \leq 0. \tag{5.29}$$

Hence, the control law (5.26), computed using (5.23)-(5.24), solves Problem 5.3 with additional running cost $c = -\,\mathcal{HJB}$. □

In Section 5.6 we show constructively under which conditions it is possible to design the dynamics of ξ_t such that function (5.24), which we call the *extended value function*, is indeed the value function corresponding to Problem 5.3 and that, consequently, the inequality (5.29) holds. Note that, since $\mathcal{V}$ solves (5.28) by construction, the procedure does not require the solution of any PDE.

5.5.2 $\mathcal{H}_\infty$ Control

The steps of the preceding subsection can be repeated exactly for the $\mathcal{H}_\infty$ control problem. The augmented linearized system is described by

$$dx_t = [Ax_t + Bu + N\,\mathsf{d}]dt + [Cx_t + Du + M\,\mathsf{d}]d\,\mathcal{W}_t, \tag{5.30}$$

with $N = \varphi(0)$, and $M = \vartheta(0)$. The remaining quantities have the same meaning given in the previous section. From the discussion in Section 5.3.2 and in particular exploiting the definitions in (5.13), we immediately see that all the equations developed in the previous section are identical for the $\mathcal{H}_\infty$ problem if we use

$$\widetilde{B} = \begin{bmatrix} B & N \end{bmatrix} \quad \text{and} \quad \widetilde{D} = \begin{bmatrix} D & M \end{bmatrix}, \tag{5.31}$$

in place of B and D, and the definitions in (5.13) in place of g, l, R and u. Then the optimal control u^* (with respect to an opportunely defined additional cost c) and the "worst-case" disturbance d^* correspond to the first m and last r, respectively, components of

$$\widetilde{u}^* = -\left(\widetilde{R} + \widetilde{l}^\top \mathcal{V}_{xx}\,\widetilde{l}\right)^{-1}\left(\widetilde{g}^\top \mathcal{V}_x^\top + \widetilde{l}^\top \mathcal{V}_{xx}\,h\right). \tag{5.32}$$

5.6 Step 2: Design of the dynamic extension

Thanks to the developments and definitions introduced in the previous sections, we can now treat the three control problems in a unified manner. We develop the following section for the infinite-horizon optimal control problem. Similar results hold for the $\mathcal{H}_\infty$ control problem and min-max zero-sum two-player game once the notation (5.13) and (5.31) is used (in place of u^*, g, l, R, B and D in the context of optimal control). The idea is to construct the dynamic extension such that $\mathcal{HJB}$ is non-positive, which in turn implies that (5.24) is the value function of Problem 5.3 for the additional cost $c = -\mathcal{HJB}$.

To streamline the presentation of the results of this section, we introduce some preliminary definitions. Let $\Phi : \mathbb{R}^n \times \mathbb{R}^n \to \mathbb{R}^{n\times n}$ be a continuous mapping such that

$$x_t^\top P(x_t) - x_t^\top P(\xi_t) = (x_t - \xi_t)^\top \Phi(x_t, \xi_t)^\top,$$

and $\Psi : \mathbb{R}^n \times \mathbb{R}^n \to \mathbb{R}^{n\times n}$ be the matrix defined as

$$\Psi(x_t, \xi_t) := \frac{1}{2}\frac{\partial}{\partial \xi_t}\left(P(\xi_t)x_t\right).$$

Define

$$\Delta(x_t, \xi_t) := (W - \Phi(x_t, \xi_t))W^{-1}\Psi(x_t, \xi_t)^\top.$$

Let $\Pi : \mathbb{R}^n \times \mathbb{R}^n \to \mathbb{R}^{n\times n}$ be a continuous mapping such that

$$\Pi(x_t, \xi_t) := P(x_t) - P(\xi_t) - W.$$

Finally, we define

$$F_{cl} := F - g\mathcal{R}^{-1}(g^\top P(x_t) + l^\top \mathcal{V}_{xx}\, H),$$

noting that $F_{cl}x_t = f + g\hat{u}$, with $\hat{u}$ obtained from (5.26) replacing $\mathcal{V}_x$ with $x_t^\top P(x_t)$. We are now ready to solve Problem 5.3. Recall that the arguments of mappings are omitted when they are clear from the context, for instance P denotes $P(x_t)$.

Proposition 5.2. Consider the cost functional (5.18) and the interconnection of system (5.2) with the control law (5.17). Assume that P is an algebraic $\bar{P}$ solution of (5.23) with Σ selected such that

$$\Delta^\top F_{cl} + F_{cl}\Delta + Y_2 - H^\top \Pi H < \Sigma + Y_1 + \Delta^\top g\mathcal{R}^{-1}g^\top\Delta, \tag{5.33}$$

where

$$\begin{aligned} Y_1(x_t) &= (Pg + H^\top \mathcal{V}_{xx}\, l)\mathcal{R}^{-1}(g^\top P + l^\top \mathcal{V}_{xx}\, H) \geq 0, \\ Y_2(x_t) &= (Pg + H^\top Pl)\left(R + l^\top Pl\right)^{-1}(g^\top P + l^\top PH) \geq 0, \end{aligned} \tag{5.34}$$

for all $(x_t, \xi) \in \Omega$. Then there exists $\bar{k} \geq 0$ such that for all $k > \bar{k}$ the function $\mathcal{V}$ defined in (5.24) satisfies the HJB equation (5.27) for all $(x_t, \xi) \in \Omega$ with

$$\dot{\xi} = -k\,\mathcal{V}_\xi^\top, \qquad u = -\mathcal{R}^{-1}\left(g^\top \mathcal{V}_x^\top + l^\top \mathcal{V}_{xx}\, h\right). \tag{5.35}$$

Moreover, Problem 5.3 is solved with the additional running cost $c = -\mathcal{HJB} \geq 0$.

The proof of Proposition 5.2 is technical. A sketch proof is given by following similar steps as the proof of [105, Proposition 2]. The idea of the proof is to select the dynamics of ξ such that (5.29) holds. Consider (5.25) and note that $\mathcal{V}_{xx} = P - \Pi$, $\mathcal{V}_\xi = x_t^\top \Psi - (x_t - \xi)^\top W$ and $\mathcal{V}_x = x_t^\top P + (x_t - \xi)^\top (W - \Phi)^\top$. Substituting these relations and $\alpha = -k\,\mathcal{V}_\xi^\top$ in (5.25) yields a quadratic form in the variables x_t and $(x_t - \xi)$, namely

$$\mathcal{HJB} = -\begin{bmatrix} x_t^\top & (x_t - \xi)^\top \end{bmatrix} \left(M + 2kS^\top S\right) \begin{bmatrix} x_t \\ (x_t - \xi) \end{bmatrix},$$

with $S = \begin{bmatrix} \Psi^\top & -W \end{bmatrix}$, and

$$M = \begin{bmatrix} M_{11} & -F_{cl}^\top (W - \Phi) \\ -(W - \Phi)^\top F_{cl} & (W - \Phi)^\top g \mathcal{R}^{-1} g^\top (W - \Phi) \end{bmatrix},$$

where $M_{11} = \Sigma + Y_1 - Y_2 + H^\top \Pi H$.

Now, we want to show that (5.29) holds. To this end we exploit the result in [120]. The matrix S has constant rank equal to n because W is positive definite. Moreover, the matrix $Z^\top = \begin{bmatrix} I & \Psi W^{-1} \end{bmatrix}$ spans the kernel of S, *i.e.* $SZ = 0$, and, if the condition (5.33) holds, Z is such that $Z^\top M Z$, *i.e.* the restriction of the matrix M to the subspace defined by the matrix Z, is positive definite. By [120] it follows that there exists $\bar{k} \geq 0$ such that, for all $k > \bar{k}$, $\mathcal{HJB} \leq 0$. This proves that the inequality (5.29) is satisfied for all $(x_t, \xi) \in \Omega$, and in particular that $\mathcal{HJB} = 0$ at $x_t = 0$, $\xi = 0$.

Furthermore, note that $\mathcal{V}$ is a non-strict Lyapunov function for the closed-loop system (5.2)-(5.35) because $\mathcal{V} > 0$ for all $(x_t, \xi) \in \Omega \setminus 0$ and $\dot{\mathcal{V}} \leq \mathcal{H}\mathcal{J}\mathcal{B} \leq 0$. The latter follows from the observation that $\mathcal{H}\mathcal{J}\mathcal{B} \leq 0$ for all $k > \bar{k}$ and from (5.27) and (5.25). Hence, by the stochastic LaSalle's invariance principle, see [121], the control law (5.35) locally asymptotically stabilizes the zero equilibrium of the closed-loop system almost surely.

The result of Proposition 5.2 relies upon the ability to select a function Σ such that condition (5.33) is satisfied. While this condition may be difficult to check in general, it becomes easy to fulfill when considered locally around the origin.

Corollary 5.1. Consider the cost functional (5.18) and the interconnection of system (5.2) with the control law (5.35). Let P be an algebraic $\bar{P}$ solution of (5.23) with $\bar{\Sigma} = \Sigma(0)$ selected such that

$$\bar{\Sigma} + Y_1(0) > Y_2(0) + C^\top W C, \tag{5.36}$$

where

$$\begin{aligned} Y_1(0) &= \big(PB + C^\top X D\big)\big(R + D^\top X D\big)^{-1}\big(B^\top P + D^\top X C\big), \\ Y_2(0) &= \big(PB + C^\top P D\big)\big(R + D^\top P D\big)^{-1}\big(B^\top P + D^\top P C\big), \end{aligned} \tag{5.37}$$

with $X = P + W$. Then there exits $\bar{k} \geq 0$ and $\hat{\Omega} \subset \mathbb{R}^n \times \mathbb{R}^n$ such that for all $k > \bar{k}$ the function $\mathcal{V}$ defined in (5.24) satisfies the HJB equation (5.27) for all $(x_t, \xi) \in \hat{\Omega}$ with $\dot{\xi}$ and u selected as in (5.35).

Proof. Assume that $\bar{\Sigma}$ satisfies (5.36). Note that at the origin $\Delta(0, 0) = 0$ in (5.33). Thus, condition (5.36) is equal to condition (5.33) at $(0, 0)$. By continuity of the functions in the inequality (5.33), there exists a non-empty set $\hat{\Omega} \subset \mathbb{R}^n \times \mathbb{R}^n$ strictly containing the origin such that (5.33) is satisfied for all $(x_t, \xi) \in \hat{\Omega}$. □

Remark 5.6. If $D = 0$, then condition (5.36) reduces to $\bar{\Sigma} > C^\top W C$. If, furthermore, $C = 0$, then the condition reduced to $\bar{\Sigma} > 0$, which is a sufficient condition for the

corollary to hold in the deterministic framework. Note also that condition (5.36) can be satisfied with "small" $\bar{\Sigma}$ if W is "small".

Remark 5.7. By continuity, all the inverse matrices in Proposition 5.2 are well-defined locally around the origin if the algebraic $\bar{P}$ solution is well-defined.

Since the extended value function $\mathcal{V}$ is known, we can easily quantify c by computing (5.25). Moreover, since k in (5.35) is a design parameter, we can select it to minimize the additional running cost. In particular, in the next result we give the conditions to solve Problem 5.3 with additional running cost $c \equiv 0$.

Corollary 5.2. Consider the cost functional (5.18) and the interconnection of system (5.2) with the control law (5.35). Let P be an algebraic $\bar{P}$ solution of (5.23) with Σ selected such that condition (5.33) holds. Assume that there exists a region $\widetilde{\Omega} \subset \Omega \setminus \{0\}$ such that $\mathcal{V}_\xi \mathcal{V}_\xi^\top$ is invertible for all $(x, \xi) \in \widetilde{\Omega}$. Then the inequality (5.29) is satisfied with the equality sign for all $(x_t, \xi) \in \widetilde{\Omega}$ if we select

$$\begin{aligned} k(x_t, \xi) = \frac{1}{2} \left(\mathcal{V}_\xi \mathcal{V}_\xi^\top\right)^{-1} \Big(& q + h^\top \mathcal{V}_{xx}\, h + 2\, \mathcal{V}_x\, f \\ & - \big(\mathcal{V}_x\, g + h^\top \mathcal{V}_{xx}\, l\big)\big(R + l^\top \mathcal{V}_{xx}\, l\big)^{-1}\big(g^\top \mathcal{V}_x^\top + l^\top \mathcal{V}_{xx}\, h\big)\Big). \end{aligned} \tag{5.38}$$

Proof. Note that k in (5.38) is obtained by solving $\mathcal{HJB} = 0$ with respect to k. □

Remark 5.8. In general, the function k obtained from Corollary 5.2 may be negative which is not acceptable because of the closed-loop stability requirement of the dynamic extension. On the other hand, note that any value of k greater than the one obtained from Corollary 5.2 satisfies the inequality (5.29) (see the proof of Proposition 5.2).

Remark 5.9. All the results of this section apply invariantly to Problem 5.4. The only, yet important, difference is that the solution of Problem 5.4 is an *exact* solution of the $\mathcal{H}_\infty$ control problem (Problem 5.2), as pointed out in Remark 5.3.

Remark 5.10. In solving the $\mathcal{H}_\infty$ control problem we have also solved the two-player min-max zero-sum game, however, differently from the previous remark, the solution of

the game is approximated. In this case the additional running cost c is in addition to q, *i.e.* c is an additional cost for the minimizing player and an additional reward for to the maximizing player. Finally, note that the "advantage" can be swapped in favor of the minimizing player if the sign of the HJB inequality (5.29) is inverted.

Remark 5.11. A similar machinery can be adopted to obtain approximate solutions to the more general class of problems described by stochastic *nonzero-sum N-player differential games*. The solutions to these games are characterised by a system of *coupled* second-order PDEs. In this case the single algebraic $\bar{P}$ solution defined in this note should be replaced by a set of matrix-valued mappings satisfying *coupled* algebraic equations. Hence, the N-player extension of Proposition 5.2 would allow for the systematic construction of "approximate solutions", which can be interpreted in terms of an ϵ_α-Nash equilibrium solution (similarly to what has been done in [110] for deterministic systems).

5.7 Simulations

In this section, we illustrate our results by means of several numerical simulations. The performance of the proposed dynamic control law (denoted by u_d in the following) are compared with the stochastic linear control law stemming from the LQR/$\mathcal{H}_\infty$ approximation (denoted by u_l) and with a deterministic nonlinear method based on state-dependent Riccati equations (SDREs) (denoted by u_e), see [122]. To this end we use parametric systems so that we can adjust the "level of nonlinearity" and the "level of noise". We first start with the optimal control problem.

5.7.1 Infinite-Horizon Optimal Control

To assess the performance of the dynamic control law, let us consider the following parametric nonlinear system

$$\begin{aligned} dx_1 &= x_2 dt, \\ dx_2 &= (\eta_1 x_1^2 + u)dt + (\eta_2 x_2)d\mathcal{W}, \end{aligned} \tag{5.39}$$

with $x(t) = [x_1, x_2]^{\mathrm{T}} \in \mathbb{R}^2$, $u(t) \in \mathbb{R}$, $\eta_1 \in \mathbb{R}\backslash\{0\}$, $\eta_2 \in \mathbb{R}\backslash\{0\}$ and the cost

$$J(x_0, u) = E\left\{\int_0^\infty \frac{1}{2}x(t)^{\mathrm{T}}x(t)dt + \frac{1}{2}u(t)^{\mathrm{T}}u(t)dt\right\}. \tag{5.40}$$

Note that η_1 and η_2 are parameters that represent the level of nonlinearity and noise respectively. We select

$$F(x) = \begin{bmatrix} 0 & 1 \\ \eta_1 x_1 & 0 \end{bmatrix}, \ \Sigma(x) = \bar{\Sigma}\begin{bmatrix} \sigma_{11} & 0 \\ 0 & \sigma_{22} \end{bmatrix}.$$

Then the explicit solution $P(x_t) = (p_{ij})$ of the algebraic equation (5.23) is given by[4]

$$\begin{aligned} p_{11} &= p_{22}\Delta, \quad p_{12} = p_{21} = \Delta + \eta_1 x_1, \\ p_{22} &= \frac{1}{2}\eta_2^2 + \sqrt{\frac{1}{4}\eta_2^4 + 2\Delta + 2\eta_1 x_1 + s_{22}}, \end{aligned} \tag{5.41}$$

where $s_{11} = \sigma_{11} + 1$, $s_{22} = \sigma_{22} + 1$, and $\Delta = \sqrt{\eta_1^2 x_1^2 + s_{11}}$. Then, we can determine the corresponding dynamic control input u_d as in (5.35).

All simulations are performed using the Euler-Maruyama method with a time step of 0.001, and with the initial state of the system and of the dynamic extension taken to be the same, *i.e.* $x_0 = \xi_0$. In the first simulation, x_0 is taken as $(-0.5, 0.5)$ and the parameters η_1 and η_2 are selected as 5 and 0.5, respectively. For illustrative purposes, we first show the time histories of the states and control inputs corresponding to the

[4]Any symbolic solver can be used for the purpose of solving (5.23). We have used Maple.

three control laws (*i.e* u_d, u_e and u_l) for a single realization of the noise in Fig. 5.1. This figure shows that the linear control law cannot stabilize the system (for this realization) and results in an infinite cost. Both dynamic and SDRE control laws could stabilize the system (for this realization). However, the dynamic control law induces a faster convergence and, thus, a smaller "single-realization cost". Note, however, that the real cost is an expectation defined as (5.40). In the following we indicate the cost (5.40) corresponding to u_d, u_e and u_l by J_{u_d}, J_{u_e} and J_{u_l}, respectively. To compute J_{u_d}, J_{u_e} and J_{u_l}, we consider the average cost of 1000 realizations of the noise, yielding $J_{u_d} = 0.477$, $J_{u_e} = 0.517$ and $J_{u_l} = \infty$. As expected, $J_{u_d} < J_{u_e}$ as $\eta_2 \neq 0$.

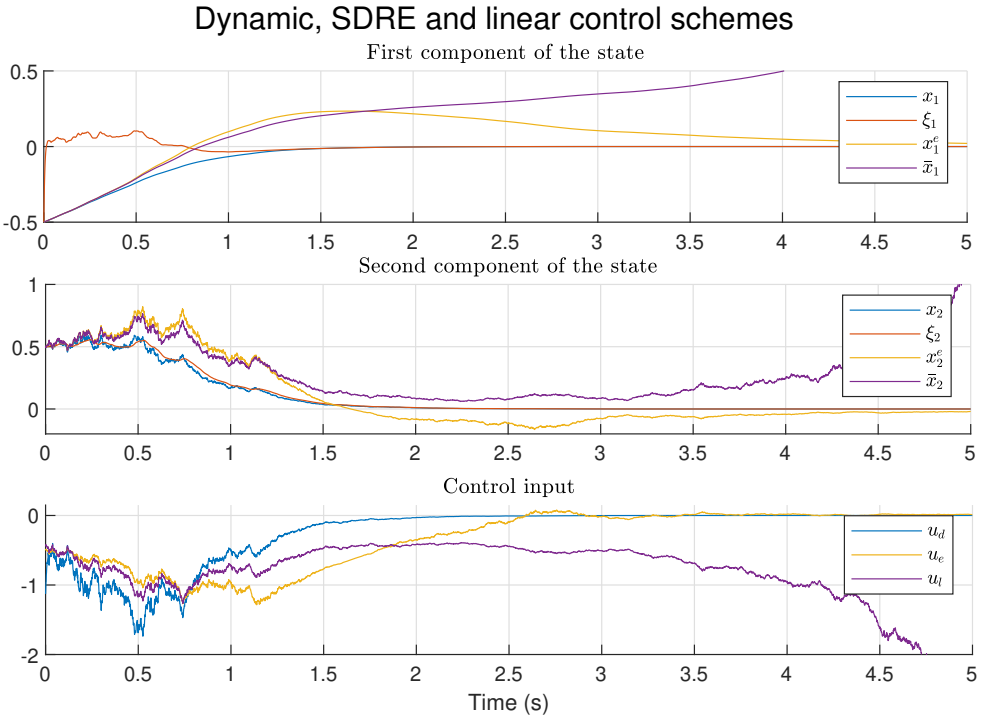

Figure 5.1: Top and middle: time histories of x (the state using u_d), ξ (the state of the dynamic extension), x^e (the state using u_e) and $\bar{x}$ (the state using u_l). Bottom: control inputs.

Now we evaluate the performance of u_d, u_e and u_l for different parameters η_1 and η_2. To this end, we maintain the initial conditions x_0 as $(-0.5, 0.5)$ but vary η_1 from 4 to 6 and η_2 from 0.3 to 0.5. The ratios of J_{u_e} and J_{u_l} with respect to J_{u_d} *i.e.* $J^r_{u_e} = J_{u_e}/J_{u_d}$ and $J^r_{u_l} = J_{u_l}/J_{u_d}$, for different η_1 and η_2 are given in Table 5.1. A value greater than 1 indicates that the dynamic control law u_d performs better than u_e or u_l, respectively. The greater the value in the table, the better the dynamic control law performs. A

"∞" in the table means that the equilibrium of system (5.39) has not been stabilized by either u_l or u_e for some realizations of the noise, resulting in an infinite ratio. We

Table 5.1: Ratios $J^r_{u_e}$ and $J^r_{u_l}$ for different η_1 and η_2.

$J^r_{u_e}/J^r_{u_l}$ η_2 / η_1	0.3	0.4	0.5
4	1.009/1.013	1.020/1.043	1.049/∞
5	1.016/1.030	1.039/∞	1.084/∞
6	1.022/∞	1.077/∞	1.151/∞

also count for how many realizations the system is stabilized. For all three control laws, the proportion of stable simulations over 1000 realizations is denoted as ρ_{u_d}, ρ_{u_e} and ρ_{u_l}, respectively. These proportions are reported in Table 5.2. It can be seen that all control laws u_d, u_e and u_l could stabilize the system for small nonlinearities and noise (*e.g.* $\eta_1 = 4$ and $\eta_2 = 0.3$). However, as η_1 or η_2 increase, the control law u_l fails more and more frequently, whereas the dynamic control law u_d and the SDRE control law u_e still stabilize the equilibrium point.

Table 5.2: Proportions ρ_{u_d}, ρ_{u_e} and ρ_{u_l} for different η_1 and η_2.

$\rho_{u_d}/\rho_{u_e}/\rho_{u_l}$ η_2 / η_1	0.3	0.4	0.5
4	1/1/1	1/1/1	1/1/0.981
5	1/1/1	1/1/0.956	1/1/0.931
6	1/1/0.963	1/1/0.882	1/1/0.820

We also expect that the performance of the dynamic control law u_d improves with respect to the control laws u_e and u_l by taking x_0 farther away from the origin. To this end, we compute the ratios $J^r_{u_e}$ and $J^r_{u_l}$ for fixed parameters $\eta_1 = 5$, $\eta_2 = 0.5$, varying x_0 from $(-0.2, 0.2)$ to $(-0.4, 0.4)$. The results, reported in Table 5.3, confirm that as x_0 moves farther from the origin, the ratio $J^r_{u_l}$ increases significantly due to the greater nonlinearity, while $J^r_{u_e}$ increases due to the larger noise injection (because of $\eta_2 x_2 d\mathcal{W}$). Note that for $x_0 = (-0.4, 0.4)$, the control law u_l cannot stabilize the system (indicated by "∞").

Table 5.3: Ratios $J^r_{u_e}$ and $J^r_{u_l}$ for different x_0.

x_0	(-0.2,0.2)	(-0.3,0.3)	(-0.4,0.4)
$J^r_{u_e}/J^r_{u_l}$	1.006/1.010	1.026/1.063	1.040/∞

5.7.2 $\mathcal{H}_\infty$ Control

We now adapt system (5.39) to study the $\mathcal{H}_\infty$ problem, namely let us consider the system

$$\begin{aligned} dx_1 &= x_2 dt, \\ dx_2 &= (\eta_1 x_1^2 + u + 0.5d)dt + (\eta_2 x_2)d\mathcal{W}, \\ y &= [x_1, x_2, u]^T, \end{aligned} \tag{5.42}$$

with $y(t) \in \mathbb{R}$, $d(t) \in \mathbb{R}$ a disturbance with well-defined $\mathcal{L}_2$ gain, $\eta_1 \in \mathbb{R}\backslash\{0\}$ and $\eta_2 \in \mathbb{R}\backslash\{0\}$. The cost $J_{\mathcal{L}_2}(x_0, u, d)$ (see (5.10)) is controlled to be negative in a region including the origin. Again, F and Σ are selected as in the previous example. Considering the definitions in (5.13), we use $\widetilde{g}$, $\widetilde{l}$ and $\widetilde{R}$ in place of g, l and R in (5.23), obtaining the explicit solution $P(x_t) = (p_{ij})$ given by

$$\begin{aligned} &p_{11} = p_{22}\Delta, \quad p_{12} = p_{21} = \frac{(\Delta + \eta_1 x_1 \mu)\mu}{s_{33}}, \\ &p_{22} = \frac{1}{2}\eta_2^2\mu + \sqrt{\frac{1}{4}\eta_2^4\mu^2 + 2\mu\Delta + 2\eta_1 x_1 \mu^2 + s_{22}s_{33}}, \end{aligned} \tag{5.43}$$

where $s_{11} = \sigma_{11} + 1$, $s_{22} = \sigma_{22} + 1$, $s_{33} = \mu^2 - \frac{1}{4}$ and $\Delta = \sqrt{\eta_1^2 x_1^2 \mu^2 + s_{33}s_{11}}$. We are now ready to design and assess the performance of the dynamic control input u_d.

Consider the disturbance $d(t) = 0.8e^{-t}$ and an attenuation factor of $\mu = 0.95$. The time step is 0.001 for all simulations. We test the control laws u_d, u_e and u_l under different parameters. To this end, we vary η_1 from 4 to 6 and η_2 from 1.25 to 1.75 respectively. The initial condition x_0 is fixed as $(0, 0.05)$. The control law u_l and u_e fail to achieve the desired attenuation for larger values of nonlinearity and uncertainty. In particular, the performance of the control law u_l is poor under large nonlinearity ($\eta_1 = 6$) while the performance of the control law u_e is poor under large uncertainty ($\eta_2 = 1.75$). These results are reported in Table 5.4, which gives the sign of the cost in (5.10) for different

η_1 and η_2. The symbols "$-$" and "$+$" represent negative or positive costs, respectively, indicating whether the desired attenuation is achieved or not, respectively.

Table 5.4: The sign of J_{u_d}, J_{u_e} and J_{u_l} for different η_1, η_2.

$J_{u_d}/J_{u_e}/J_{u_l}$ η_2 / η_1	1.25	1.5	1.75
4	$-/-/-$	$-/-/-$	$-/+/-$
5	$-/-/-$	$-/-/-$	$-/+/-$
6	$-/-/+$	$-/-/+$	$-/+/+$

Finally, we simulate the system under different initial conditions but same parameters $\eta_1 = 5$ and $\eta_2 = 1.5$, finding an approximation of the attenuation region $\bar{\Omega}$. To this end, we consider a mesh grid around the origin with a grid distance of 0.05. All nodes of the grid are tested as an initial condition in the simulations. The regions where the system is stable and the disturbance is successfully attenuated by u_d, u_e and u_l are denoted as $\bar{\Omega}_d$, $\bar{\Omega}_e$ and $\bar{\Omega}_l$, respectively. Fig. 5.2 confirms that the dynamic control law u_d provides the largest attenuation region (blue).

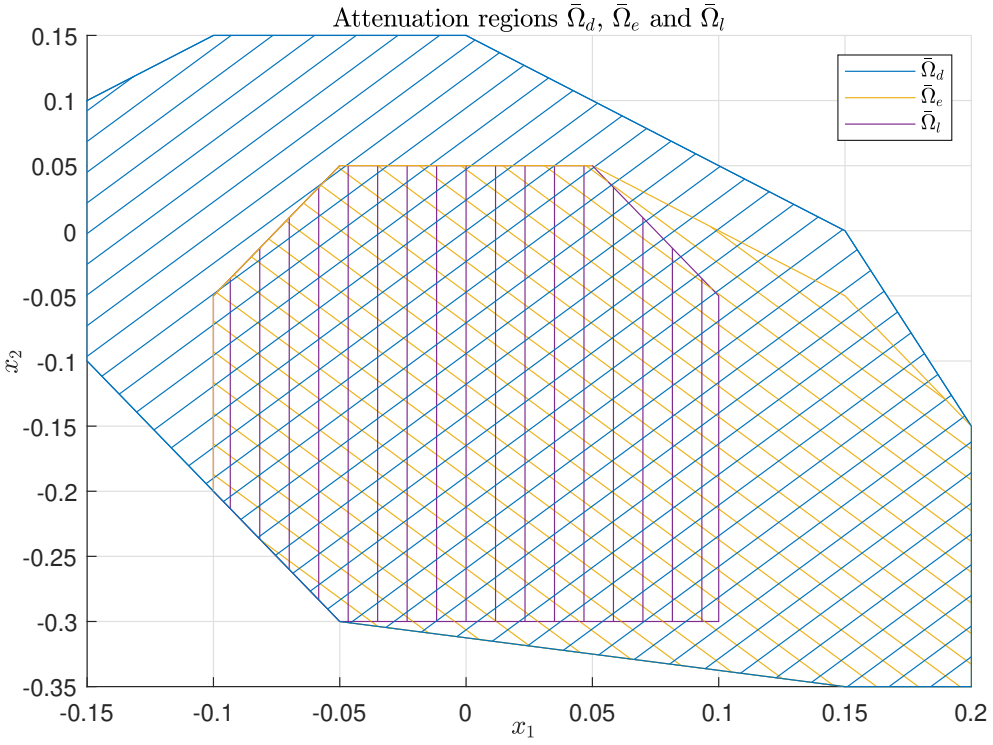

Figure 5.2: Attenuation regions $\bar{\Omega}_d$ (blue), $\bar{\Omega}_e$ (yellow) and $\bar{\Omega}_l$ (purple).

5.8 Conclusion

In this chapter we have considered three related problems, *i.e.* the infinite-horizon optimal control problem, the $\mathcal{H}_\infty$ control problem and the min-max zero-sum two-player game for stochastic nonlinear systems. Exploiting the notion of algebraic $\bar{P}$ solution we have proposed *approximate* solutions for the infinite-horizon optimal control problem and the min-max zero-sum game, and an *exact* solution for the $\mathcal{H}_\infty$ control problem. A major advantage of the proposed method is that the control design hinges only on the solution of *algebraic equations*. Additionally, in the context of optimal control and min-max zero-sum games the level approximation can be exactly quantified in terms of an additional cost/reward, which can be minimized. Some interesting differences between the deterministic and stochastic settings have been highlighted and extensions of the proposed technique to the more general class of problems described by stochastic nonzero-sum games have been outlined. The efficacy and improved performance of the proposed method with respect to linear and/or deterministic counterparts have been demonstrated via extensive numerical simulations.

Part III

Observation

Chapter 6

A Hybrid Observer for Stochastic Linear Systems

6.1 Introduction

The problem of observability and observer design of dynamical systems has been widely studied. It consists in constructing an estimation of the state of the system that converges to the true value of the state. When the dynamical system is described by stochastic differential equations (SDEs), the problem becomes remarkably more difficult due to the presence of unknown Brownian motion in the dynamics of the system.

Several estimation techniques for stochastic systems have been proposed in the literature. An early approach based on a Lyapunov-like method to solve the stochastic estimation problem was proposed by Tarn and Rasis [123]. Later on, several approaches have been developed for related or generalised classes of stochastic systems, such as discrete-time stochastic nonlinear systems [124], stochastic time-delay systems [125] and networked control systems [126]. In addition to these extensions, several classes of observers have been proposed for stochastic estimation. For instance, in [126–130], the observer design problem is changed into an optimization problem where the observer gains are selected by solving linear matrix inequalities (LMIs). Other stochastic observers include

Luenberger observers [131], reduced-order observers [132] and hybrid observers [133].

In this chapter, we focus on the problem of observer design for stochastic linear systems, with the objective of obtaining improved state estimation with respect to the state of the art. We begin by recalling the difficulties of stochastic observability and recalling that perfect state estimation is possible only by using an "idealistic", but non-causal, stochastic observer which has complete access to the Brownian motion. Of course, this last assumption (knowledge of the Brownian motion) is unrealistic. Thus, our objective is to find an alternative causal approach that approximates the behaviour of the idealistic observer. We note that although the Brownian motion is not measurable, it is possible to approximate the variations of the Brownian motion in discrete time. To this end, we introduce an *a posteriori* approach that reconstructs the variations of the Brownian motion discretely. By combining this reconstruction with the idealistic observer, a hybrid observer is constructed. The performance of this hybrid observer depends on a sampling period. This sampling period is related to how frequently the variations of the Brownian motion are approximated and, for an idealistic zero sampling period, the behaviour of the idealistic observer is recovered. Although the zero sampling period is not achievable in practical use, by definition of asymptotic stability in probability, the probability of a large estimation error is guaranteed to be small by using a small enough sampling period.

The remainder of the chapter is organized as follows. In Section 6.2 we first recall the difficulties of stochastic observability and we then formulate the problem. In Section 6.3 we construct the hybrid observer and solve our problem. Section 6.4 contains numerical simulations that illustrate the results of the chapter. Section 6.5 contains some concluding remarks.

6.2 Preliminaries

In this section, we provide a formulation of the problem that we aim to solve. We first start with the motivation and explain the potential of a hybrid approach for stochastic observability. To this end, we recall the difficulties involved with stochastic observability which are discussed, for instance, in [134]. Consider a stochastic linear system with two outputs

$$\begin{aligned} dx_t &= (Ax_t + Bu_t)dt + Fx_t d\mathcal{W}_t, \\ y_t^a &= C_a x_t, \quad y_t^b = C_b x_t, \end{aligned} \tag{6.1}$$

where $x_t \in \mathbb{R}^n$ is the state, $u_t \in \mathbb{R}$ is the control input, $y_t^a \in \mathbb{R}$ and $y_t^b \in \mathbb{R}$ are the system outputs, $\mathcal{W}_t$ is the Brownian motion, $A \in \mathbb{R}^{n\times n}$, $B \in \mathbb{R}^{n\times 1}$, $F \in \mathbb{R}^{n\times n}$, $C_a \in \mathbb{R}^{1\times n}$ and $C_b \in \mathbb{R}^{1\times n}$. Assume that our objective is to find an observer such that the estimation error of the state converges to zero asymptotically. A first attempt[1] for achieving this is to use a traditional deterministic observer, namely

$$d\hat{x}_t^D = (A\hat{x}_t^D + Bu_t + L(y_t^a - C_a\hat{x}_t^D))dt, \tag{6.2}$$

where $\hat{x}_t^D$ is the estimation of x_t and L is the observer gain. Interconnecting the deterministic observer (6.2) with system (6.1), we obtain the error dynamics

$$de_t^D = (A - LC_a)e_t^D dt + Fx_t d\mathcal{W}_t, \tag{6.3}$$

where $e_t^D = x_t - \hat{x}_t^D$ is the estimation error. Although (6.3) has a stable equilibrium point with a suitable L, the stochastic term $Fx_t d\mathcal{W}_t$ keeps exciting the error dynamics. In particular, the estimation error e_t^D will not converge to zero unless the state x_t converges to zero. Therefore, the deterministic observer (6.3) cannot achieve our estimation objective. To overcome this problem the literature has focused on achieving mean-square stability of the error dynamics by Lyapunov-like methods [123, 127]. In particular, [127] indicates that although perfect observation cannot be achieved by

[1] One may consider the Kalman filter as a first attempt. However, note that in (6.1) the Brownian motion is not simply added as the process noise but multiplied with the state as the diffusion term.

a deterministic observer, the estimation error can be exponentially bounded in the mean-square sense.

In this chapter, we follow a different approach. To properly introduce this approach let us assume that for now, we can construct an *idealistic* stochastic observer of the type

$$\begin{aligned} d\hat{x}_t^I &= (A\hat{x}_t^I + Bu_t + L_1(y_t^a - C_a\hat{x}_t^I))dt \\ &\quad + (F\hat{x}_t^I + L_2(y_t^a - C_a\hat{x}_t^I))d\mathcal{W}_t, \end{aligned} \tag{6.4}$$

where $\hat{x}_t^I \in \mathbb{R}^n$ is the estimation of the state given by the idealistic observer, L_1 and L_2 are observer gains and $\mathcal{W}_t$ is the Brownian motion. One can see that this observer is unrealistic because $\mathcal{W}_t$ is unknown in practice. By interconnecting (6.1) and (6.4), we obtain the following error dynamics

$$de_t^I = (A - L_1C_a)e_t^I dt + (F - L_2C_a)e_t^I d\mathcal{W}_t, \tag{6.5}$$

where $e_t^I = x_t - \hat{x}_t^I$ is the estimation error of the idealistic observer. Then it is clear that if the gains L_1 and L_2 are chosen such that (6.5) is asymptotically stable in probability or mean-square, then the estimation error will go to zero asymptotically in probability or mean-square.

In summary, while the idealistic observer (6.4) can achieve, with opportune choices of L_1 and L_2, a zero estimation error in probability, it is unrealistic because it requires knowledge of the Brownian motion. In this chapter, we propose a new practical observer with the objective of approximating the behaviour of the idealistic observer (6.4). First of all, consider the quantity $\Delta\mathcal{W}_\varepsilon(k) = \mathcal{W}_{t_k} - \mathcal{W}_{t_{k-1}}$, where $\varepsilon = t_k - t_{k-1}$ is the sampling period. For simplicity, from now on we abuse the notation and indicate with $\mathcal{W}_k$, x_k and so on the quantities $\mathcal{W}_{t_k}$, x_{t_k} and so on. The idea that we want to formulate is the following: if we can construct an approximation $\Delta\widehat{\mathcal{W}}_\varepsilon(k)$ of $\Delta\mathcal{W}_\varepsilon(k)$ and we can find an appropriate concept of convergence, then it could be possible to construct an observer based on the quantity $\Delta\widehat{\mathcal{W}}_\varepsilon(k)$ which has the property of behaving as the idealistic

observer (6.4) when ε goes to zero. To precisely formulate this problem, we introduce the following hybrid observer

$$\begin{aligned} d\hat{x}_t^H &= (A\hat{x}_t^H + Bu_t + L_1(y_t^a - C_a\hat{x}_t^H))dt, \\ \hat{x}_k^{H+} &= \hat{x}_k^H + (F\hat{x}_{k-1}^{H+} + L_2(y_{k-1}^a - C_a\hat{x}_{k-1}^{H+}))\Delta\widehat{\mathcal{W}}_\varepsilon(k), \end{aligned} \tag{6.6}$$

where $\hat{x}_k^{H+}$ indicates the value of $\hat{x}_k^H$ after the jump. Thus, the hybrid dynamics of (6.6) flow from t_{k-1}^+ to t_k according to the law of the deterministic observer (6.2). At time t_k there is a jump and the state of the hybrid observer is updated according to the second equation in (6.6). We note that if $\Delta\widehat{\mathcal{W}}_\varepsilon(k) = \Delta\mathcal{W}_\varepsilon(k)$, then by definition of the Itô integral the limiting solution of (6.6) as $\varepsilon \to 0$ is the solution of the idealistic observer. In summary, if we can design an opportune approximation $\Delta\widehat{\mathcal{W}}_\varepsilon(k)$ of $\Delta\mathcal{W}_\varepsilon(k)$ then we can recover the idealistic convergence in the limit. In other words, we want to solve the following problem.

Problem 6.1. Consider system (6.1), the hybrid observer (6.6) and their associated estimation error system with state e_t^H. The problem of *ε-approximate stochastic observer design* consists in designing the parameters of the hybrid observer (6.6) such that if $\varepsilon \to 0$ then the associated estimation error system is asymptotically stable in probability.

Note that from a practical point of view the limiting behaviour is not achievable. However, by definition of asymptotic stability in probability we have the property that for all $\alpha > 0$ and $\gamma > 0$, there exists $\beta > 0$ and $\eta > 0$, such that for all $\varepsilon \leq \beta$ and $\delta \geq \eta$ we have that

$$\mathcal{P}\left\{\sup_{t\geq\delta} ||e^H(t, e_0, t_0)|| > \gamma\right\} < \alpha.$$

In other words, we can always guarantee that the probability of a large estimation error is small, by picking a small enough ε. In the rest of the chapter, we design $\Delta\widehat{\mathcal{W}}_\varepsilon(k)$, L_1 and L_2 to solve Problem 6.1.

6.3 Hybrid Stochastic Observer

In this section, we solve Problem 6.1. We first focus on the scalar case. This is of course just a toy example (as the observation problem is trivial in the scalar case) but since this case is simpler, it provides easier insights to understand. Then we solve the general case.

Now, we start by designing $\Delta\widehat{\mathcal{W}}_\varepsilon(k)$. Previous research shows that if one had access to the state, then $\Delta\widehat{\mathcal{W}}_\varepsilon(k)$ can be constructed from the diffusion term of the system dynamics. Consider system (6.1), assume that there exists $\delta > 0$ such that $|Fx_k| \geq \delta$ almost surely for all $k \in \mathbb{Z}_{\geq 0}$. Then, an approximation of $\Delta\mathcal{W}_\varepsilon(k)$ is given by [135]

$$\Delta\overline{\mathcal{W}}_\varepsilon(k) = (Fx_{k-1})^\dagger[\Delta x_k - (Ax_{k-1} + Bu_{k-1})\varepsilon], \tag{6.7}$$

where $\Delta x_k = x_k - x_{k-1}$. As discussed in [135], $\Delta\overline{\mathcal{W}}_\varepsilon(k)$ converges to $\Delta\mathcal{W}_\varepsilon(k)$ weakly as $\varepsilon \to 0$. It is clear that this approximation is not an available solution for Problem 6.1 as the system state is unknown. Note that when $\Delta\widehat{\mathcal{W}}_\varepsilon(k)$ is being computed, all the estimations of the state before time t_k are known. Therefore, a first attempt for constructing $\Delta\widehat{\mathcal{W}}_\varepsilon(k)$ is to approximate (6.7) by replacing the state with its estimation. However, this is still unrealistic as $\hat{x}_k^{H+}$ is not available at time t_k and, according to the hybrid observer (6.6), Δx_k cannot be approximated until time t_k^+ when $\hat{x}_k^{H+}$ is provided. For this reason, (6.7) cannot be used for constructing $\Delta\widehat{\mathcal{W}}_\varepsilon(k)$ of the hybrid observer (6.6). However, it gives us an idea about how to construct $\Delta\widehat{\mathcal{W}}_\varepsilon(k)$ from the diffusion term.

Instead of using the diffusion term of the system dynamics, we consider the diffusion term of the output dynamics $dy_t^b = C_b dx_t$. This is motivated by the fact that the quantity $\Delta y_k^b = y_k^b - y_{k-1}^b$, which is the variation of a measurable output y_t^b, can be easily acquired. Similarly to the assumption for (6.7), the associated diffusion coefficient C_bFx_{k-1} should be non-zero. Considering that this diffusion coefficient is approximated as $C_bF\hat{x}_{k-1}^{H+}$ for constructing $\Delta\widehat{\mathcal{W}}_\varepsilon(k)$, it is reasonable to assume the following.

Assumption 6.1. Consider system (6.1), there exists $\delta > 0$ and $\delta' > 0$ such that $\left|C_b F \hat{x}_k^{H+}\right| \geq \delta$ almost surely for all $k \geq \delta'$.

This assumption guarantees that the approximation of the output diffusion coefficient is non-zero after a certain number of samplings. Note that if the system state x_t converges to zero, as discussed in Section 6.2, observation can be easily achieved by a deterministic observer. Therefore, we focus on the case in which the system state x_t and the corresponding state estimation $\hat{x}_k^{H+}$ do not converge to zero. One may also find that if $C_b F = 0_{1\times n}$, then Assumption 6.1 does not hold at any sampling time. This indicates that the system output y_t^b contains no information of the Brownian motion and thus cannot be used for constructing $\Delta\widehat{\mathcal{W}}_\varepsilon(k)$. In addition to this, Assumption 6.1 may still be invalid for some $k \in \mathbb{Z}_{\geq 0}$. From a practical point of view, if $C_b F \hat{x}_{k-1}^{H+} = 0$, then we can skip the sampling at t_k and postpone it to t_{k+1}. With the absence of $\Delta\widehat{\mathcal{W}}_\varepsilon(k)$ at t_k, our hybrid observer would simply degenerate to the deterministic observer at the sampling time t_k. Now let Assumption 6.1 hold, $\Delta\widehat{\mathcal{W}}_\varepsilon(k)$ is designed as

$$\Delta\widehat{\mathcal{W}}_\varepsilon(k) = (C_b F \hat{x}_{k-1}^{H+})^{-1}[\Delta y_k^b - C_b(A\hat{x}_{k-1}^{H+} + Bu_{k-1})\varepsilon]. \tag{6.8}$$

It is clear that this approximation is improved as the estimation of the state is improved. In particular, if the perfect observation $\hat{x}_{k-1}^{H+} = x_{k-1}$ is achieved as $\varepsilon \to 0$, then in (6.8) we would have

$$\begin{aligned}\Delta\widehat{\mathcal{W}}_\varepsilon(k) &= (C_b F x_{k-1})^{-1}[\Delta y_k^b - C_b(Ax_{k-1} + Bu_{k-1})\varepsilon] \\ &= (C_b F x_{k-1})^{-1} C_b[\Delta x_k - (Ax_{k-1} + Bu_{k-1})\varepsilon].\end{aligned} \tag{6.9}$$

Now recall the forward-Euler discretization of system (6.1) [136]

$$x_k - x_{k-1} = (Ax_{k-1} + Bu_{k-1})\varepsilon + Fx_{k-1}\Delta\mathcal{W}_\varepsilon(k) + o(\varepsilon^2), \tag{6.10}$$

where $o(\varepsilon^2)$ is a higher-order term of ε^2, *e.g.* there exists a time independent constant

$M > 0$ such that $o(\varepsilon^2) \leq M\varepsilon^2$ for all k. Substituting (6.10) in (6.9) yields

$$\begin{aligned}\Delta\widehat{\mathcal{W}}_\varepsilon(k) &= (C_b F x_{k-1})^{-1} C_b [F x_{k-1} \Delta\mathcal{W}_\varepsilon(k) + o(\varepsilon^2)] \\ &= \Delta\mathcal{W}_\varepsilon(k) + o(\varepsilon^2),\end{aligned}$$

which implies $\Delta\widehat{\mathcal{W}}_\varepsilon(k)$ converges to $\Delta\mathcal{W}_\varepsilon(k)$ weakly as $\varepsilon \to 0$. Then as discussed in Section 6.2, the behaviour of the idealistic observer is recovered in the limit.

Now combining (6.8) with (6.6), a hybrid stochastic observer is constructed. Note that two different outputs y_t^a and y_t^b are used in this hybrid structure, one for computing $\Delta\widehat{\mathcal{W}}_\varepsilon(k)$ and another one for estimating the state. The need for two outputs is motivated later in Section 6.3. Now, we focus on the design of L_1 and L_2 for solving Problem 6.1. For a better understanding of this hybrid observer, we first focus on the scalar case.

6.3.1 Scalar Case

First of all, note that in the scalar case the observation problem is trivial because $x_t = y_t^a / C_a$. However, this study of the scalar case is helpful to understand the general case later in Section 6.3.2. Now we introduce a proposition for designing the observer gains L_1 and L_2.

Proposition 6.1. Consider system (6.1) and the hybrid observer (6.6) in the scalar case. Let Assumption 6.1 hold. The associated estimation error e_t^H converges to zero asymptotically in probability as $\varepsilon \to 0$ for any $L_1 C_a > 0$ and $L_2 = 0$.

Proof. For the time being, we focus on the discretization of the estimation error dynamics e_t^H and denote $e_k^{H+} = x_k - \hat{x}_k^{H+}$ (because $x_k = x_k^+$). Note that the forward-Euler discretization of the hybrid observer (6.6) is given by

$$\begin{aligned}\hat{x}_k^{H+} = \hat{x}_{k-1}^{H+} &+ (A\hat{x}_{k-1}^{H+} + Bu_{k-1} + L_1(y_{k-1}^a - C_a\hat{x}_{k-1}^{H+}))\varepsilon \\ &+ (F\hat{x}_{k-1}^{H+} + L_2(y_{k-1}^a - C_a\hat{x}_{k-1}^{H+}))\Delta\widehat{\mathcal{W}}_\varepsilon(k) + o(\varepsilon^2).\end{aligned} \tag{6.11}$$

By interconnecting (6.10) with (6.11), we have

$$\begin{aligned} e_k^{H+} =& e_{k-1}^{H+} + (A - L_1 C_a) e_{k-1}^{H+} \varepsilon + F x_{k-1} \Delta \mathcal{W}_\varepsilon(k) \\ & - F \hat{x}_{k-1}^{H+} \Delta \widehat{\mathcal{W}}_\varepsilon(k) - L_2 C_a e_{k-1}^{H+} \Delta \widehat{\mathcal{W}}_\varepsilon(k) + o(\varepsilon^2). \end{aligned} \tag{6.12}$$

To simplify (6.12), we first focus on the term $F\hat{x}_{k-1}^{H+}\Delta\widehat{\mathcal{W}}_\varepsilon(k)$. Recall the expression of $\Delta\widehat{\mathcal{W}}_\varepsilon(k)$ from (6.8) and observe that in the scalar case $F\hat{x}_{k-1}^{H+}(C_b F\hat{x}_{k-1}^{H+})^{-1} = C_b^{-1}$, thus

$$\begin{aligned} & F\hat{x}_{k-1}^{H+}\Delta\widehat{\mathcal{W}}_\varepsilon(k) \\ &= C_b^{-1}[(y_k^b - y_{k-1}^b) - C_b(A\hat{x}_{k-1}^{H+} + Bu_{k-1})\varepsilon + o(\varepsilon^2)] \\ &= (x_k - x_{k-1}) - (A\hat{x}_{k-1}^{H+} + Bu_{k-1})\varepsilon + o(\varepsilon^2). \end{aligned} \tag{6.13}$$

Note that the term $(x_k - x_{k-1})$ is given by the forward-Euler discretization of system (6.1). Substituting (6.10) in (6.13) yields

$$\begin{aligned} F\hat{x}_{k-1}^{H+}\Delta\widehat{\mathcal{W}}_\varepsilon(k) &= (Ax_{k-1} + Bu_{k-1})\varepsilon + Fx_{k-1}\Delta\mathcal{W}_\varepsilon(k) \\ &\quad - (A\hat{x}_{k-1}^{H+} + Bu_{k-1})\varepsilon + o(\varepsilon^2) \\ &= Ae_{k-1}^{H+}\varepsilon + Fx_{k-1}\Delta\mathcal{W}_\varepsilon(k) + o(\varepsilon^2). \end{aligned} \tag{6.14}$$

Finally, substituting (6.14) in (6.12), we have the error dynamics

$$e_k^{H+} = e_{k-1}^{H+} - L_1 C_a e_{k-1}^{H+}\varepsilon - L_2 C_a e_{k-1}^{H+}\Delta\widehat{\mathcal{W}}_\varepsilon(k) + o(\varepsilon^2). \tag{6.15}$$

Thus, if $0 < L_1 C_a < \dfrac{2}{\varepsilon}$ and $L_2 = 0$, then e_k^{H+} will converge to zero asymptotically as $\varepsilon \to 0$. Now we look at what happens between sampling times. The estimation of the state between sampling times is given by the deterministic observer (6.2). Without loss of generality, consider the time interval (t_{k-1}^+, t_k), the error dynamics of e_t^H is given by

$$de_t^H = (A - L_1 C_a)e_t^H dt + Fx_t d\mathcal{W}_t, \tag{6.16}$$

where $t \in (t_{k-1}^+, t_k)$. Note that the increments of the Brownian motion follows normal

distribution with zero mean and variance $(t - t_{k-1}^+) < (t_k - t_{k-1}^+) = \varepsilon$. Therefore, consider the error dynamics (6.16), the variations of e_t^H are bounded in probability for $t \in (t_{k-1}^+, t_k)$, which means that for any $\alpha > 0$ and $\gamma > 0$, there exist $\beta > 0$ such that for all $\varepsilon \leq \beta$ we have that

$$\mathcal{P}\left\{\sup_{t\in(t_{k-1}^+,t_k)} ||e^H(t, e_{k-1}^{H+}, t_{k-1}^+) - e_{k-1}^{H+}|| > \gamma\right\} < \alpha.$$

The probability of large variations in the estimation error is guaranteed to be low by picking a sufficient small sampling period ε. In other words, we can always guarantee that for $t \in (t_{k-1}^+, t_k)$, e_t^H is close enough to e_{k-1}^{H+} with high probability. In conclusion, e_t^H will converge to zero asymptotically in probability as $\varepsilon \to 0$ with any observer gains satisfying $L_1 C_a > 0$ and $L_2 = 0$ and Problem 6.1 is solved for the scalar case.

□

Remark 6.1. From a practical point of view, ε cannot be exactly zero. For any finite ε, we require $0 < L_1 C_a < \dfrac{2}{\varepsilon}$ as per proof of Proposition 6.1.

6.3.2 General Case

We are now ready to consider the general case. The main difference is that (6.13) is not valid for the general case and thus the error dynamics of e_k^{H+} cannot be simplified as (6.15). However, we can still obtain the estimation error dynamics in a similar way.

Proposition 6.2. Consider the stochastic linear system (6.1) and the hybrid observer (6.6). Let Assumption 6.1 hold. The forward-Euler discretization of the error dynamics e_t^H is given by

$$\begin{aligned} e_k^{H+} = e_{k-1}^{H+} &+ [(I - \Psi_{k-1})A - L_1 C_a] e_{k-1}^{H+} \varepsilon + o(\varepsilon^2) \\ &+ (I - \Psi_{k-1}) F e_{k-1}^{H+} \Delta\mathcal{W}_\varepsilon(k) - L_2 C_a e_{k-1}^{H+} \Delta\widehat{\mathcal{W}}_\varepsilon(k), \end{aligned} \tag{6.17}$$

where $\Psi_k = F\hat{x}_k^{H+}(C_b F \hat{x}_k^{H+})^{-1} C_b$.

Proof. Similar with the scalar case, we still focus on simplifying the term $F\hat{x}_{k-1}^{H+}\Delta\widehat{\mathcal{W}}_\varepsilon(k)$. Note that in the general case $F\hat{x}_k^{H+}(C_bF\hat{x}_k^{H+})^{-1}C_b \neq I$ and cannot be cancelled. Therefore, denoting $\Psi_k = F\hat{x}_k^{H+}(C_bF\hat{x}_k^{H+})^{-1}C_b$ and substituting (6.8) in (6.12) yields

$$\begin{aligned} e_k^{H+} &= e_{k-1}^{H+} + (A - L_1C_a)e_{k-1}^{H+}\varepsilon + Fx_{k-1}\Delta\mathcal{W}_\varepsilon(k) + o(\varepsilon^2) \\ &\quad - \Psi_{k-1}[Ae_{k-1}^{H+}\varepsilon + Fx_{k-1}\Delta\mathcal{W}_\varepsilon(k)] - L_2C_ae_{k-1}^{H+}\Delta\widehat{\mathcal{W}}_\varepsilon(k) \\ &= e_{k-1}^{H+} + [(I - \Psi_{k-1})A - L_1C_a]e_{k-1}^{H+}\varepsilon + o(\varepsilon^2) \\ &\quad + (I - \Psi_{k-1})Fx_{k-1}\Delta\mathcal{W}_\varepsilon(k) - L_2C_ae_{k-1}^{H+}\Delta\widehat{\mathcal{W}}_\varepsilon(k). \end{aligned} \tag{6.18}$$

We observe that $\Psi_{k-1}F\hat{x}_{k-1}^{H+} = F\hat{x}_{k-1}^{H+}$. Thus, we have

$$\begin{aligned} (I - \Psi_{k-1})Fx_{k-1} &= (I - \Psi_{k-1})F(e_{k-1}^{H+} + \hat{x}_{k-1}^{H+}) \\ &= (I - \Psi_{k-1})Fe_{k-1}^{H+} + (I - \Psi_{k-1})F\hat{x}_{k-1}^{H+} \\ &= (I - \Psi_{k-1})Fe_{k-1}^{H+} + F\hat{x}_{k-1}^{H+} - F\hat{x}_{k-1}^{H+} \\ &= (I - \Psi_{k-1})Fe_{k-1}^{H+}. \end{aligned} \tag{6.19}$$

Thus, substituting (6.19) in (6.18) we obtain (6.17).

□

System (6.17) is a discrete time-varying stochastic system. The stability problem of this type of systems is complex. However, a stability criterion is provided, for instance, in [137]. Thus, L_1 and L_2 can be designed by applying [137, Theorem 3.1/4.1]. Once the discrete error dynamics (6.17) is guaranteed to be stable in probability by using suitable L_1 and L_2, we again look at what happens between the sampling times. As discussed before, the probability of large variations in the estimation error is low for sufficient small sampling period. Therefore, e_t^H will converge to zero asymptotically in probability as $\varepsilon \to 0$ and Problem 6.1 is solved for the general case.

Now we conclude this section with a series of observations.

Remark 6.2. If Proposition 6.2 is applied to the scalar case, we note that

$$\Psi_k = F\hat{x}_k^{H+}(C_bF\hat{x}_k^{H+})^{-1}C_b = 1. \tag{6.20}$$

Substituting this expression in (6.17), yields

$$e_k^{H+} = e_{k-1}^{H+} - L_1C_ae_{k-1}^{H+}\varepsilon - L_2C_ae_{k-1}^{H+}\Delta\widehat{\mathcal{W}}_\varepsilon(k) + o(\varepsilon^2),$$

i.e. the error dynamics (6.15) of the scalar case is retrieved. In other words, the error dynamics (6.17) can be simplified as (6.15) in the scalar case and the two results are consistent.

Now based on the error dynamics (6.17), we can explain the need for the two outputs y_t^a and y_t^b for solving Problem 6.1. For simplicity, we again set $L_2 = 0_{n\times 1}$.

Proposition 6.3. If C_a and C_b are linearly dependent, then the dynamics of (6.17) is not influenced by L_1.

Proof. If C_a and C_b are linearly dependent, then there exists $\alpha \neq 0$ such that $C_a = \alpha C_b$. We observe that

$$\begin{aligned} C_b(I - \Psi_{k-1}) &= C_b - C_bF\hat{x}_{k-1}^{H+}(C_bF\hat{x}_{k-1}^{H+})^{-1}C_b \\ &= C_b - C_b = 0_{1\times n} \end{aligned} \tag{6.21}$$

Thus, multiplying C_b on the both sides of (6.17) yields

$$\begin{aligned} C_be_k^{H+} &= C_be_{k-1}^{H+} + C_b[(I - \Psi_{k-1})A - L_1C_a]e_{k-1}^{H+}\varepsilon + C_b(I - \Psi_{k-1})Fe_{k-1}^{H+}\Delta\mathcal{W}_\varepsilon(k) + o(\varepsilon^2) \\ &= C_be_{k-1}^{H+} - C_bL_1C_ae_{k-1}^{H+}\varepsilon + o(\varepsilon^2) \\ &= C_be_{k-1}^{H+} - (\alpha C_bL_1)C_be_{k-1}^{H+}\varepsilon + o(\varepsilon^2). \end{aligned} \tag{6.22}$$

Denoting $E_k = C_be_k^{H+}$, the previous scalar system is rewritten as

$$E_k = E_{k-1} - (C_aL_1)E_{k-1}\varepsilon + o(\varepsilon^2). \tag{6.23}$$

Note that if e_k^{H+} converges to zero, then E_k converges to zero, but the opposite may not hold. Applying the results of Proposition 6.1, for $C_a L_1 > 0$ and ε sufficiently small we have that E_k converges to zero. Furthermore, since $E_k = 0$ is a stable equilibrium point of the scalar system (6.23), $\{e_t^H | C_b e_t^H = 0\}$ will be an invariant set as $\varepsilon \to 0$. In particular, if e_{k-1}^{H+} belongs to this invariant set, then

$$e_k^{H+} = e_{k-1}^{H+} + (I - \Psi_{k-1}) A e_{k-1}^{H+} \varepsilon + (I - \Psi_{k-1}) F e_{k-1}^{H+} \Delta \mathcal{W}_\varepsilon(k) + o(\varepsilon^2), \tag{6.24}$$

where we have used that $L_1 C_a e_{k-1}^{H+} = \alpha L_1 E_{k-1} \to 0$ as $E_{k-1} \to 0$. Recall that $\Psi_{k-1} = F \hat{x}_{k-1}^{H+} (C_b F \hat{x}_{k-1}^{H+})^{-1} C_b$. Thus, the error system (6.24) is completely decided by the estimated state and the sampling period. Tuning the observer gain L_1 is ineffective and the estimation error will either converge to zero or keep increasing inside the invariant set. Therefore, two outputs y_t^a and y_t^b with linearly independent C_a and C_b are required. A detailed justification of this is also given in [138].

Remark 6.3. Consider Proposition 6.3 in the scalar case. For any non-zero C_b, $E_k = C_b e_k^{H+} = 0$ is equivalent with $e_k^{H+} = 0$. Thus the result of Proposition 6.1 is retrieved. This means that one output y_t^a is sufficient for solving the scalar case.

6.4 Example: deterministic, idealistic and hybrid stochastic observer

In this section, we illustrate our results by means of numerical simulations. The simulation results of the deterministic, idealistic and hybrid observers are provided and compared. The comparison shows that our hybrid observer is significantly better than the deterministic observer and is comparable with the idealistic observer. Moreover, in our approach the estimation of the state converges to the true value of the state as the sampling period $\varepsilon \to 0$. We first start with the scalar case.

6.4.1 Example: a simple scalar system

Consider system (6.1) with the parameters

$$A = -2, \quad B = 1, \quad F = -1, \quad C_a = C_b = 3.$$

The input and initial values are set as

$$u_t = 10, \quad x_0 = 2, \quad \hat{x}_0 = 1.$$

The observer gain of the deterministic observer is set as $L = 15$ to ensure the estimation error is bounded in the mean-square sense [127]. The same observer gains, $L_1 = 3$ and $L_2 = 0$, are used for both idealistic and hybrid observers (these gains correspond to a stable case). Two sampling periods $\varepsilon = 10^{-4}$ and $\varepsilon = 10^{-3}$ are tested for the hybrid observer. The simulation step (for the integration of the stochastic differential equations) is set at 10^{-6}. Fig. 6.1 shows the time history of the state of the system x_t (green) and of the corresponding estimated states $\hat{x}_t^D$ (purple), $\hat{x}_t^I$ (yellow) and $\hat{x}_t^H$ (red and blue) for the scalar case of deterministic, idealistic and hybrid observers, respectively. Fig. 6.2 shows the associated estimation errors. The figures confirm that, since the condition of Proposition 6.1 is satisfied, the hybrid observers perform well and, as expected, similarly to the idealistic observer. Moreover, Fig. 6.2 confirms that for our hybrid observer, the estimated state $\hat{x}_t^H$ is improved by using a smaller sampling period ε. For instance, the oscillations of the estimation error e_t^H decrease as the sampling period $\varepsilon \to 0$. Furthermore, we note that the estimation error e_t^H oscillates around a specific center line which represents the dynamics $\dot{e}_t = -L_1 C_a e_t$. Recall the error dynamics (6.15), we know that this center line is the limiting behaviour of e_t^H as the sampling period $\varepsilon \to 0$.

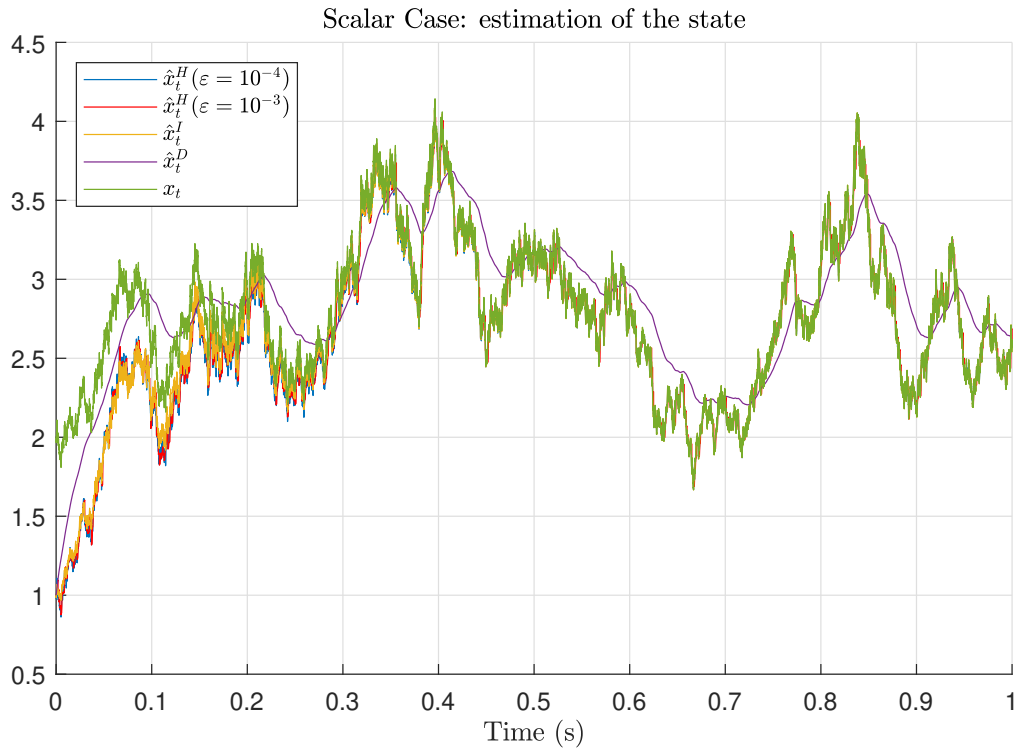

Figure 6.1: Time history of the state of the system x_t (green) and of the corresponding estimated states $\hat{x}_t^D$ (purple), $\hat{x}_t^I$ (yellow) and $\hat{x}_t^H$ (red and blue) for the scalar case of deterministic, idealistic and hybrid observers, respectively.

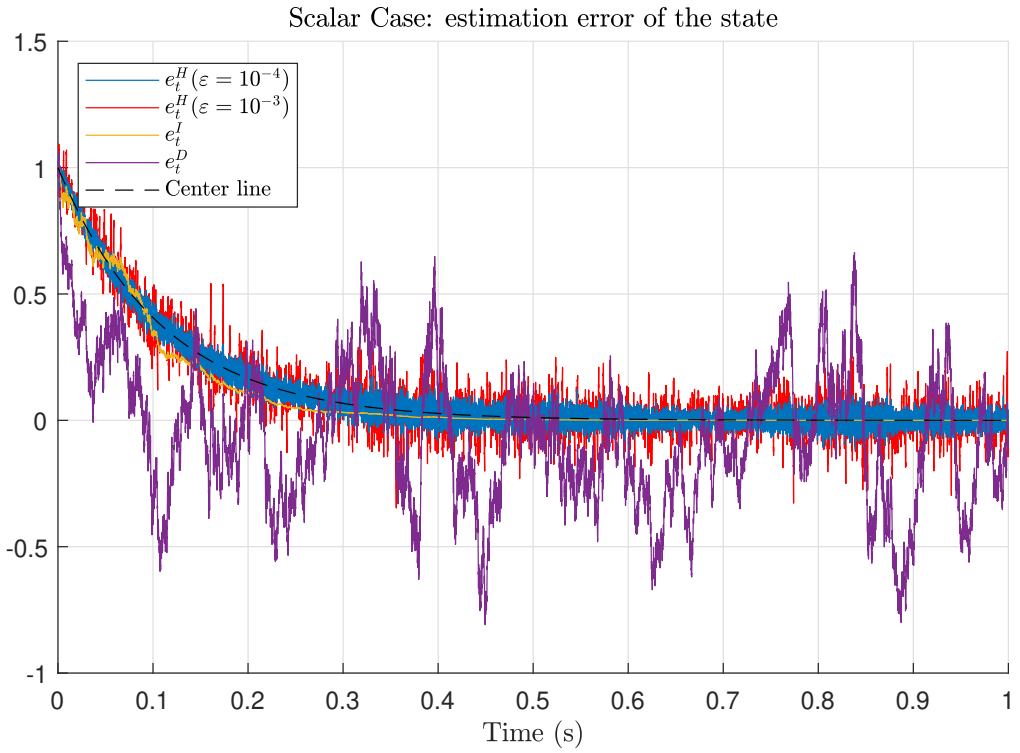

Figure 6.2: Time history of the estimation errors e_t^D (purple), e_t^I (yellow) and e_t^H (red and blue) for the scalar case of deterministic, idealistic and hybrid observers, respectively. The black dash line represents the error dynamics $\dot{e}_t = -L_1 C_a e_t$.

The above example confirms that the condition of Proposition 6.1 is sufficient. We now consider the case in which the estimation error of the hybrid observer does not converge to zero. We select $L_1 = -0.1$ and $L_2 = 0$. The system parameters, input and initial values are maintained. Now under this setting, we have $L_1 C_a = -0.3 < 0$. Thus, the condition of Proposition 6.1 is not satisfied in this example. The time histories of the estimated states and of their associated estimation errors are illustrated in Fig. 6.3 and Fig. 6.4 respectively. We can see that the estimation error e_t^H still oscillates around a center line but it diverges as a whole. Therefore, Fig. 6.1 to Fig. 6.4 confirm that the stability condition given by Proposition 6.1 is sufficient and tight (if L_2 is not used).

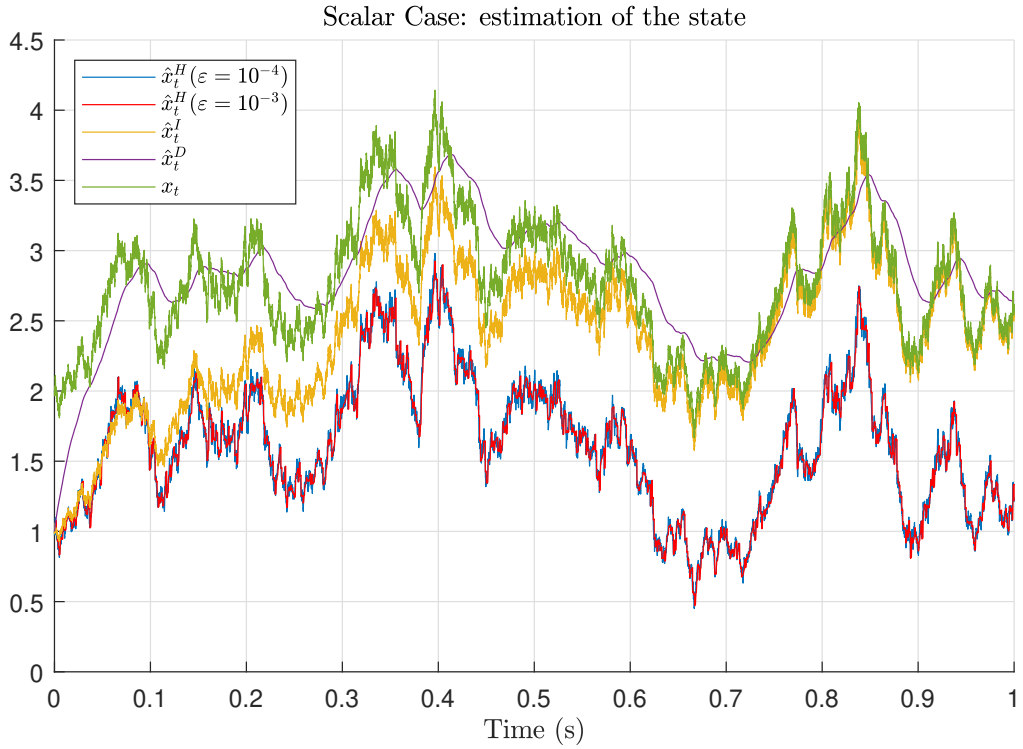

Figure 6.3: Time history of the state of the system x_t (green) and of the corresponding estimated states $\hat{x}_t^D$ (purple), $\hat{x}_t^I$ (yellow) and $\hat{x}_t^H$ (red and blue) for the scalar case of deterministic, idealistic and hybrid observers, respectively.

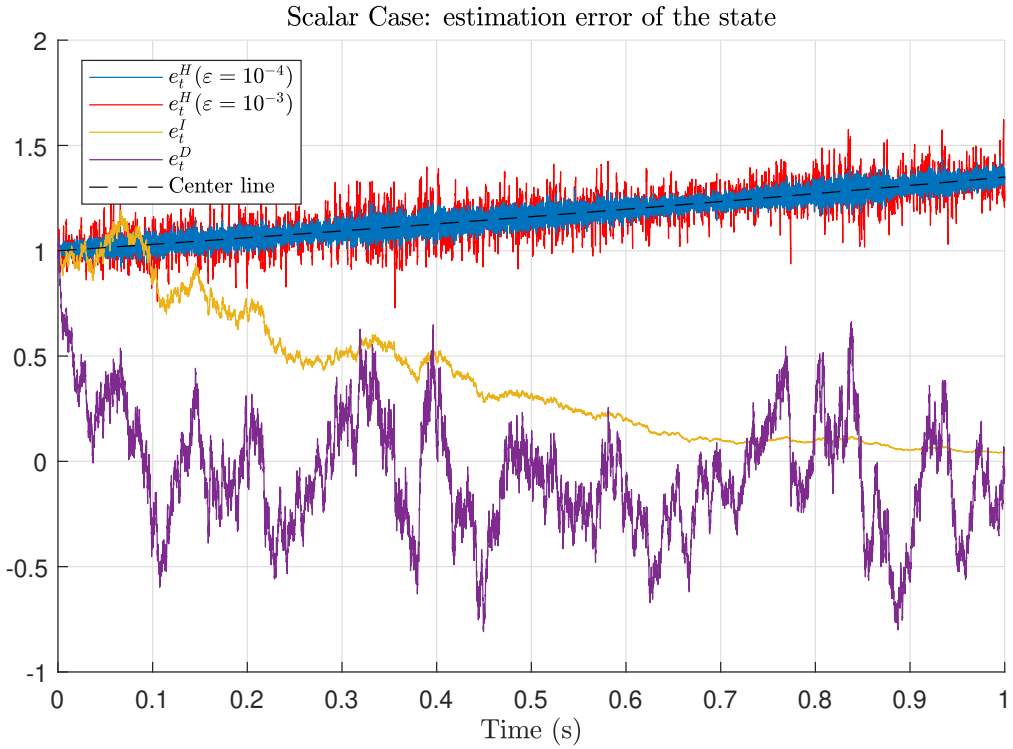

Figure 6.4: Time history of the estimation errors e_t^D (purple), e_t^I (yellow) and e_t^H (red and blue) for the scalar case of deterministic, idealistic and hybrid observers, respectively. The black dash line represents the error dynamics $\dot{e}_t = -L_1 C_a e_t$.

6.4.2 Example: a general system of order $n = 3$

Consider a three-dimensional system described by matrices

$$A = \begin{bmatrix} -10 & 7 & 3 \\ 0.2 & -10 & 9 \\ 0 & 1 & -10 \end{bmatrix}, \; B = \begin{bmatrix} 1 \\ 2 \\ 1 \end{bmatrix}, \; F = 0.5A, C_a = \begin{bmatrix} 1 & 3 & 2 \end{bmatrix}, \; C_b = \begin{bmatrix} 2 & 1 & 3 \end{bmatrix}.$$

The input and initial values are set as

$$u_t = 10, \;\; x_0 = \begin{bmatrix} 2 & 0 & 1 \end{bmatrix}^{\mathrm{T}}, \;\; \hat{x}_0 = \begin{bmatrix} 1 & 1 & 1 \end{bmatrix}^{\mathrm{T}}.$$

For both idealistic and hybrid observer, the observer gains are set as $L_1 = [-1, 2, 1]^{\mathrm{T}}$ and $L_2 = [0, 0, 0]^{\mathrm{T}}$. The observer gain of the deterministic observer is set as $L = [9, 6, 6]^{\mathrm{T}}$ to guarantee that the estimation error is bounded in the mean-square sense [127]. Two sampling periods $\varepsilon = 10^{-4}$ and $\varepsilon = 10^{-3}$ are tested for the hybrid observer. The

simulation step (for the integration of the stochastic differential equations) is set at 10^{-6}. The estimations of the state and of the associated estimation errors of the deterministic, idealistic and hybrid observers are given for $\hat{x}_1$ (Fig. 6.5), e_1 (Fig. 6.6), $\hat{x}_2$ (Fig. 6.7), e_2 (Fig. 6.8), $\hat{x}_3$ (Fig. 6.9) and e_3 (Fig. 6.10).

The figures confirm that the hybrid observers perform well and, as expected, similarly to the idealistic observer. Moreover, they confirm that for our hybrid observer, the estimated state is improved by using a smaller sampling period ε. For instance, the oscillations of the estimation error decrease as the sampling period $\varepsilon \to 0$.

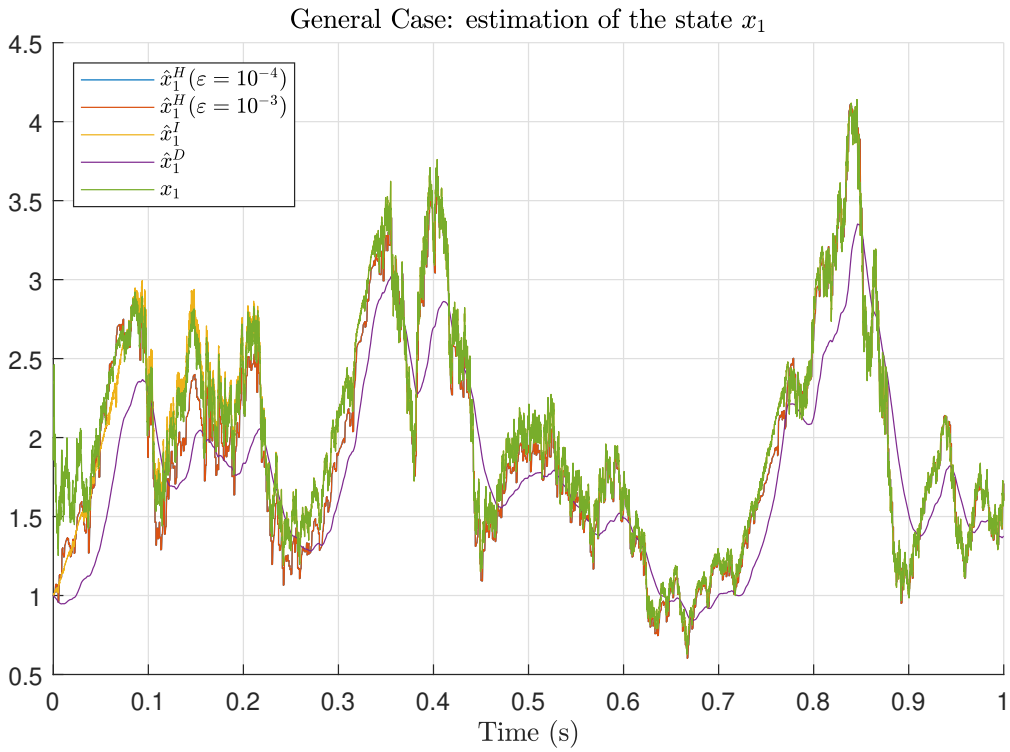

Figure 6.5: Time history of the state x_1 (green) and of the corresponding estimated state $\hat{x}_1^D$ (purple), $\hat{x}_1^I$ (yellow) and $\hat{x}_1^H$ (red and blue) for the general case of deterministic, idealistic and hybrid observers, respectively.

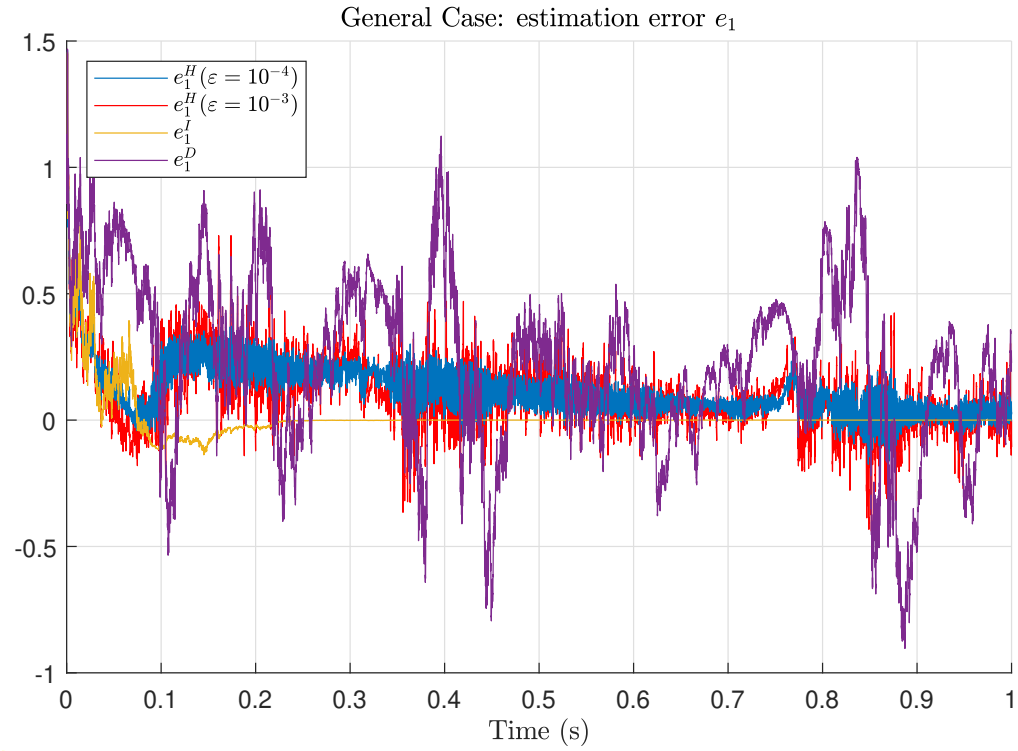

Figure 6.6: Time history of the estimation error e_1^D (purple), e_1^I (yellow) and e_1^H (red and blue) for the general case of deterministic, idealistic and hybrid observers, respectively.

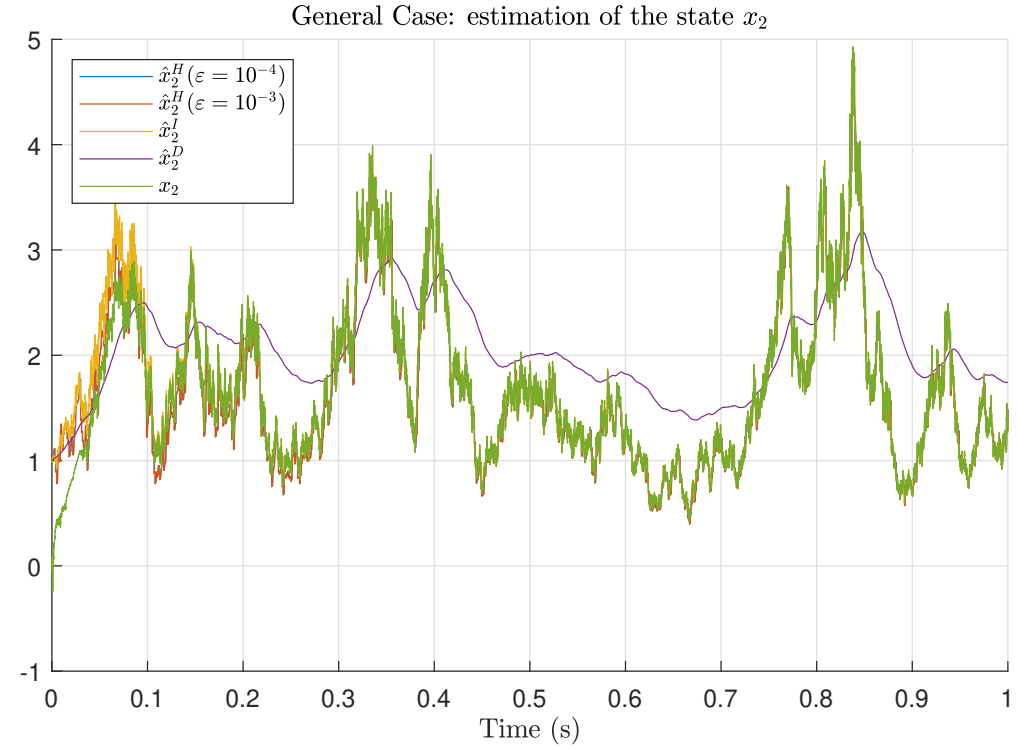

Figure 6.7: Time history of the state x_2 (green) and of the corresponding estimated state $\hat{x}_2^D$ (purple), $\hat{x}_2^I$ (yellow) and $\hat{x}_2^H$ (red and blue) for the general case of deterministic, idealistic and hybrid observers, respectively.

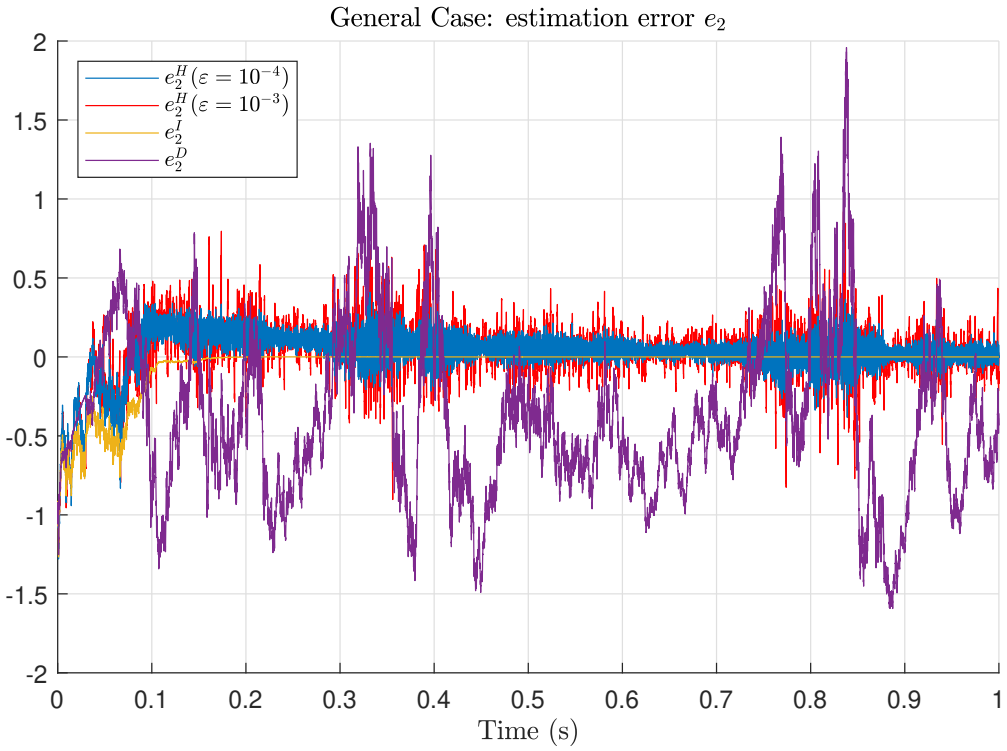

Figure 6.8: Time history of the estimation error e_2^D (purple), e_2^I (yellow) and e_2^H (red and blue) for the general case of deterministic, idealistic and hybrid observers, respectively.

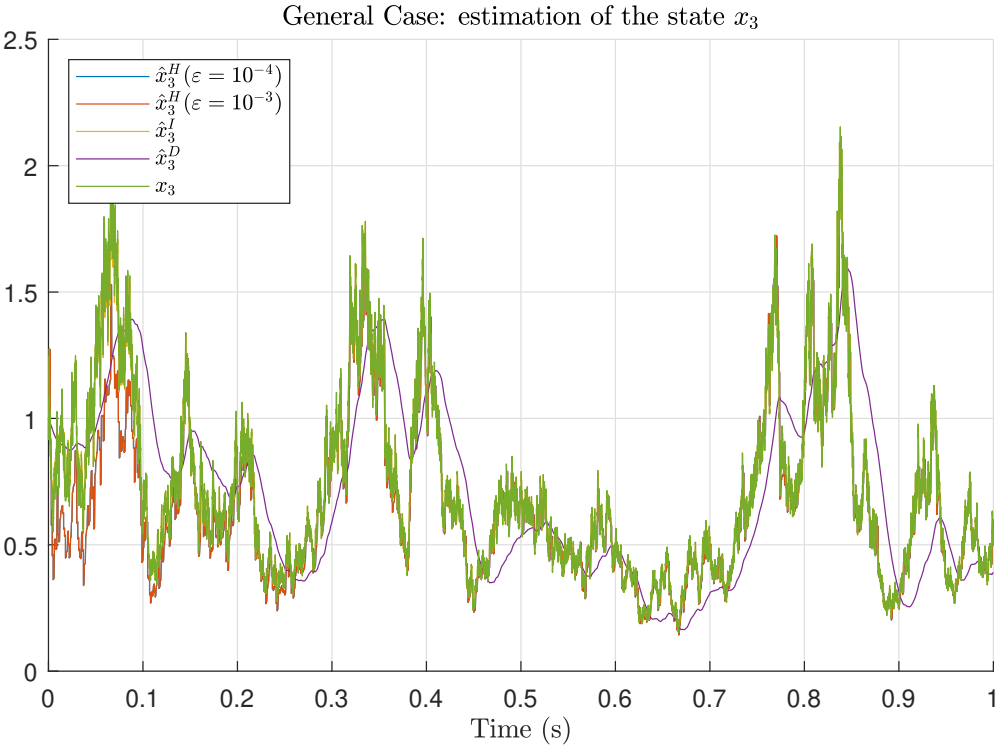

Figure 6.9: Time history of the state x_3 (green) and of the corresponding estimated state $\hat{x}_3^D$ (purple), $\hat{x}_3^I$ (yellow) and $\hat{x}_3^H$ (red and blue) for the general case of deterministic, idealistic and hybrid observers, respectively.

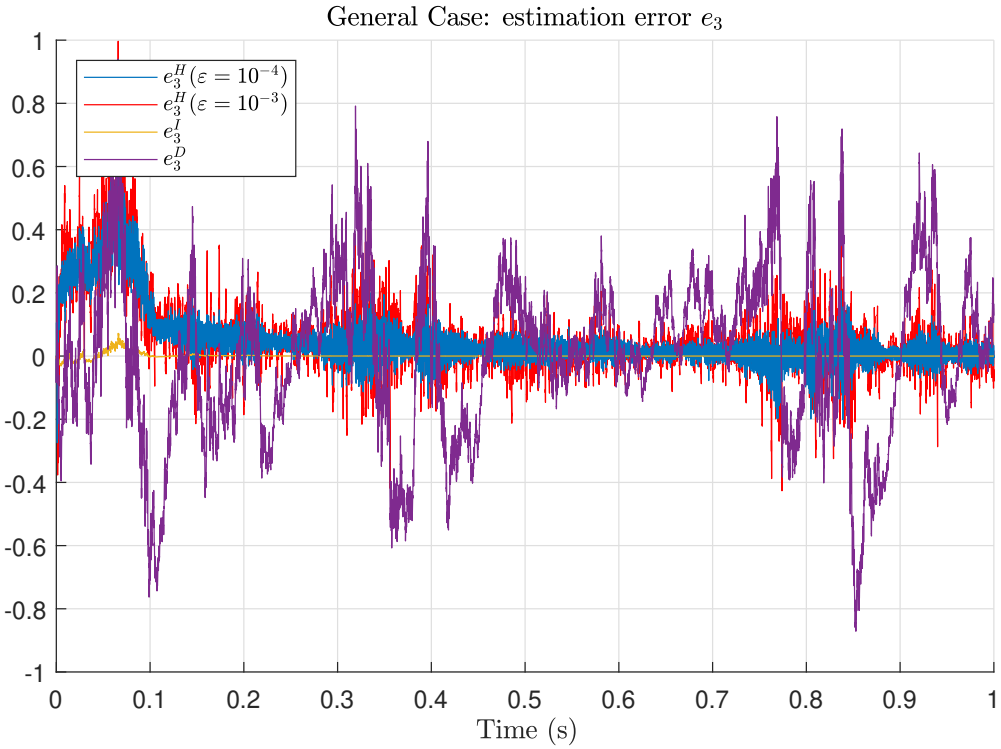

Figure 6.10: Time history of the estimation error e_3^D (purple), e_3^I (yellow) and e_3^H (red and blue) for the general case of deterministic, idealistic and hybrid observers, respectively.

6.5 Conclusion

In this chapter, we proposed a hybrid observer for stochastic linear systems. We first recalled the difficulties arising in the problem of stochastic observability. Then, to properly introduce our approach, we recalled an idealistic observer which assumes that the Brownian motion is known. This idealistic observer is non-causal. Thus, we introduced an *a posteriori* method to approximate the variations of the Brownian motion. Based on this approximation, we constructed a hybrid observer which approximates the behaviour of the idealistic observer. The associated estimation error converges to zero asymptotically in probability as the sampling period $\varepsilon \to 0$. Although this limiting behaviour cannot be achieved in practice, the probability of a large estimation error can be guaranteed to be small by using small enough ε.

Chapter 7

Conclusions

7.1 Contributions

This thesis contributes to three control topics, namely approximation, control and observation of complex dynamical systems.

Regarding the topic of approximation, one contribution is the data-driven MOR by moment-matching for MIMO systems. Novelties of the proposed method include the extension from SISO systems to MIMO systems by tangential directions and the extension from one-sided to two-sided moment-matching, which doubles the number of interpolation points. The validation of these results on a combined system of wind farms and classical generators is also a contribution. The proposed method has the advantages of data-driven and low computational complexity and, therefore, presents a potential for application in the field of renewable energy.

On the topic of control, a novel contribution is the approximate solutions of HJB equations that arise in the control problems of stochastic nonlinear systems. The main advantage of the proposed approximate solution is that the control design requires only the solution of simpler algebraic equations, avoiding solving partial differential equations. Furthermore, the level of approximation can be exactly quantified in terms of

an additional cost. By minimizing this additional cost, the approximation is improved. The comparison with other approximate methods shows the advantages of the proposed method.

Finally, the last contribution is a hybrid observer for the observation of stochastic linear systems. An *a posteriori* method is proposed to approximate the variations of the Brownian motion. Furthermore, the associated estimation error converges to zero asymptotically in probability as the sampling period tends to zero.

7.2 Future Work

The present work has raised several interesting topics for future research:

- **Nonlinear MOR**. Although the nonlinear MOR is recalled in Chapter 2, Chapter 4 only considers the linear MOR, relying on the linearization of the system. Further research should evaluate the performance of the nonlinear MOR presented in Section 2.3, which skips the linearization and provides a more accurate ROM. The key step is to select an appropriate family of basis functions for approximating the nonlinear moments.

- **Parametric MOR**. All results presented in Chapter 4 assume that the wind speed is constant. A more practical MOR method should consider time-varying wind speed, which is treated as a parameter for the ROM. This has raised a particular interest in the parametric MOR of wind farms. One possible way is to consider the expansion around a certain wind speed and this ensures the accuracy of the ROM within a neighborhood of the expansion point.

- **Other type of WTG**. Chapter 3 and Chapter 4 consider only PMSG-type wind farms. Another typical technology is the Doubly fed Induction Generator (DFIG). Unlike PMSG, DFIG is not isolated from the grid and, therefore, is influenced

more by grid-side disturbances. Future research can consider the model order reduction of DFIG-type or mixed-type wind farms.

- **Output-feedback control**. Chapter 5 focuses on three state-feedback control problems. Another interesting topic for further research is the output-feedback control of stochastic nonlinear systems.

- **Observer-based state-feedback control.** Chapter 6 proposes a hybrid observer for estimating the state. Given the state estimation, it is possible to stabilize the stochastic system by state-feedback control. Further research will explore the observer-based controller design for stochastic linear systems.

- **Nonlinearity and multi-dimensional Brownian motion.** Chapter 6 considers stochastic linear systems and one-dimensional Brownian motion. This result has been extended to stochastic nonlinear systems in [139]. Future research may simultaneously consider general stochastic nonlinear systems and multi-dimensional Brownian motion.

Appendix A

Parameters

A. Wind farm parameters

This section summarises the parameters of the wind farm as follows.

1) Wind turbine: $c_1 = 1$, $c_2 = 39.52$, $c_6 = 2.04$, $c_7 = 14.47$, $c_3 = c_4 = c_5 = c_8 = c_9 = 0$, $R = 40\text{m}$, $A = 5,026.5\text{m}^2$, $\rho = 1.225\text{kg/m}^3$, $\nu = 90$, $I_t = 4\text{kg} \cdot \text{km}^2$, $\tau = 0.1\text{s}$ and $v_w = 7\text{m/s}$.

2) Turbine speed controller: $\omega_{mn} = 1,602\text{min}^{-1}$, $K_p = 0.1^\circ \cdot s/\text{rad}$ and $K_i = 0.02^\circ/\text{rad}$.

3) Generator: 2 pairs of poles, $r_s = 15\text{m}\Omega$, $\lambda_m = 2.35\text{V} \cdot \text{s/rad}$, $L_q = 0.12732\text{mH}$ and $L_d = 0.12764\text{mH}$.

4) Generator vector controller: $Q_s^* = 10\text{VAr}$, $K_{pq} = 0.0637\text{V/A}$, $K_{iq} = 7.5\text{V/(A} \cdot \text{s)}$, $K_{pd} = 0.0638\text{V/A}$ and $K_{id} = 7.5\text{V/(A} \cdot \text{s)}$.

5) DC bus: $C = 10\text{mF}$ and $V_{DC}^* = 2.6\text{kV}$.

6) Grid side system: $r_l = 20\text{m}\Omega$, $L_l = 1\text{mH}$, $U_w^r = 0.97\text{kV}$, $U_g^r = 66\text{kV}$ and $f^r = 50\text{Hz}$.

7) Grid side controller: $K_{pg} = 0.6032\text{A/V}$ and $K_{ig} = 14.2122\text{A/(V} \cdot \text{s)}$.

8) Grid current controller: $K_{pc} = 0.2803\text{V/A}$ and $K_{ic} = 10\text{V/(A} \cdot \text{s)}$.

B. IEEE 14-bus system

This section introduces the topology of the IEEE 14-bus system, which consists of 14 buses, 5 generators, 11 loads and 20 transmission lines. The diagram of the IEEE 14-bus system is presented in Fig. A.1 [140].

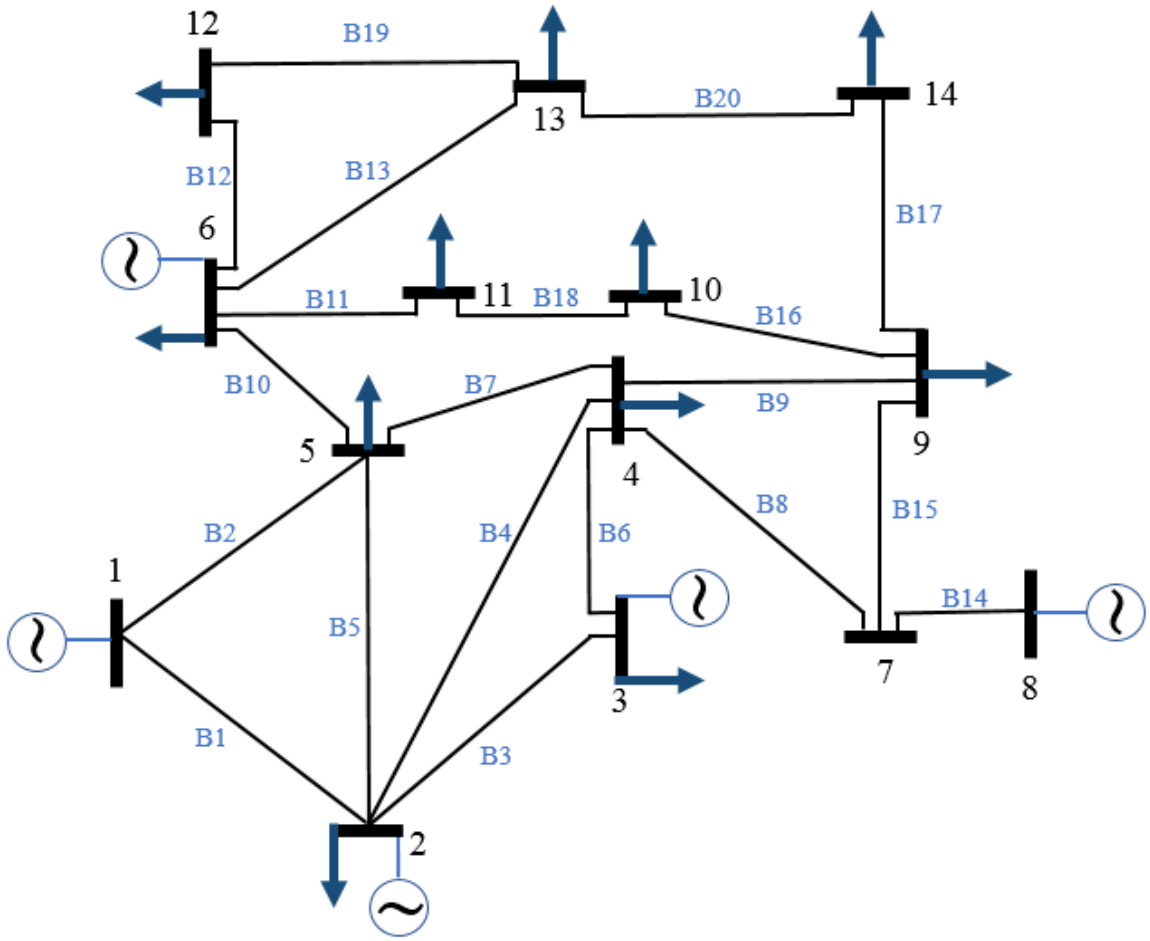

Figure A.1: The diagram of IEEE 14-bus system, indicating generators, loads positions and transmission lines.

C. IEEE 14-bus system parameters

This section summarises the bus and line parameters of the IEEE 14-bus system in Table A.1 and Table A.2, respectively.

Table A.1: Bus parameters

Bus No.	Generation		Load	
	Real(MW)	Reactive(MVAR)	Real(MW)	Reactive(MVAR)
1	100.0	-16.9	0.0	0.0
2	100.0	42.4	21.7	12.7
3	100.0	23.4	94.2	19.0
4	0.0	0.0	47.8	3.9
5	0.0	0.0	7.6	1.6
6	100.0	12.2	11.2	7.5
7	0.0	0.0	0.0	0.0
8	100.0	17.4	0.0	0.0
9	0.0	0.0	29.5	16.6
10	0.0	0.0	9.0	5.8
11	0.0	0.0	3.5	1.8
12	0.0	0.0	6.1	1.6
13	0.0	0.0	13.5	5.8
14	0.0	0.0	14.9	5.0

Table A.2: Line parameters

Bus No.	Between buses	Line impedance		Half line Susceptance(pu)
		Resistance(pu)	Reactance(pu)	
1	1-2	0.01938	0.05917	0.02640
2	2-3	0.04699	0.19797	0.02190
3	2-4	0.05811	0.17632	0.01870
4	1-5	0.05403	0.22304	0.02460
5	2-5	0.05695	0.17388	0.01700
6	3-4	0.06701	0.17103	0.01730
7	4-5	0.01335	0.04211	0.0064
8	5-6	0.0	0.25202	0.0088
9	4-7	0.0	0.20912	0.0085
10	7-8	0.0	0.17615	0.0090
11	4-9	0.0	0.55618	0.0082
12	7-9	0.0	0.11001	0.0084
13	9-10	0.03181	0.08450	0.0079
14	6-11	0.09498	0.19890	0.0087
15	6-12	0.12291	0.25581	0.0092
16	6-13	0.06615	0.13027	0.0086
17	9-14	0.12711	0.27038	0.0089
18	10-11	0.8205	0.19207	0.0077
19	12-13	0.22092	0.19988	0.0098
20	13-14	0.17093	0.34802	0.0091

D. Code availability

A Demo is developed to illustrate the proposed data-driven model order reduction (MOR) method. Provided with a simple benchmark model of the multiple-input-multiple-output (MIMO) systems, the corresponding reduced-order model (ROM) and bode plots are produced by this illustrative demo. For more benchmark models, see [51]. The code is available at `https://github.com/zilong-gong/WindFarmMOR`.

Bibliography

[1] Z. Gong, J. Mao, A. Junyent-Ferré, and G. Scarciotti, "Model order reduction of large-scale wind farms: A data-driven approach," *IEEE Transactions on Power Systems (accepted)*, 2024.

[2] Z. Gong, T. Mylvaganam, and G. Scarciotti, "Constructive approximate solutions to classes of state-feedback control problems for stochastic nonlinear systems," *Automatica (revision submitted)*, 2024.

[3] Z. Gong and G. Scarciotti, "A hybrid observer for practical observability of linear stochastic systems," in *61st IEEE Conference on Decision and Control (CDC)*, 2022, pp. 1033–1038.

[4] H. Zhang, Z. Gong, A. Junyent-Ferré, and G. Scarciotti, "A benchmark model for model order reduction: Large-scale wind farms," in *11th Vienna International Conference on Mathematical Modelling (accepted)*, 2025.

[5] A. Mellone, Z. Gong, and G. Scarciotti, "Modelling, prediction and design of covid-19 lockdowns by stringency and duration," *Scientific Reports*, vol. 11, no. 1, p. 15708, 2021.

[6] A. C. Antoulas, *Approximation of large-scale dynamical systems*. SIAM, 2005.

[7] B. Moore, "Principal component analysis in linear systems: Controllability, observability, and model reduction," *IEEE Transactions on Automatic Control*, vol. 26, no. 1, pp. 17–32, 1981.

[8] D. G. Meyer, "Fractional balanced reduction: Model reduction via fractional representation," *IEEE Transactions on Automatic Control*, vol. 35, no. 12, pp. 1341–1345, 1990.

[9] S. Lall and C. Beck, "Error-bounds for balanced model-reduction of linear time-varying systems," *IEEE Transactions on Automatic Control*, vol. 48, no. 6, pp. 946–956, 2003.

[10] S. Gugercin and A. C. Antoulas, "A survey of model reduction by balanced truncation and some new results," *International Journal of Control*, vol. 77, no. 8, pp. 748–766, 2004.

[11] M. Heinkenschloss, T. Reis, and A. Antoulas, "Balanced truncation model reduction for systems with inhomogeneous initial conditions," *Automatica*, vol. 47, no. 3, pp. 559–564, 2011.

[12] C. Grussler, T. Damm, and R. Sepulchre, "Balanced truncation of k-positive systems," *IEEE Transactions on Automatic Control*, vol. 67, no. 1, pp. 526–531, 2022.

[13] A. M. Burohman, B. Besselink, J. M. A. Scherpen, and M. K. Camlibel, "From data to reduced-order models via generalized balanced truncation," *IEEE Transactions on Automatic Control*, vol. 68, no. 10, pp. 6160–6175, 2023.

[14] S. Kung and D. Lin, "Optimal hankel-norm model reductions: Multivariable systems," *IEEE Transactions on Automatic Control*, vol. 26, no. 4, pp. 832–852, 1981.

[15] K. Glover, "All optimal hankel-norm approximations of linear multivariable systems and their L^∞-error bounds," *International journal of control*, vol. 39, no. 6, pp. 1115–1193, 1984.

[16] M. Safonov, R. Chiang, and D. Limebeer, "Optimal hankel model reduction for nonminimal systems," *IEEE Transactions on Automatic Control*, vol. 35, no. 4, pp. 496–502, 1990.

[17] K. Zhou, "Frequency-weighted L_∞ norm and optimal hankel norm model reduction," *IEEE Transactions on Automatic Control*, vol. 40, no. 10, pp. 1687–1699, 1995.

[18] D. Kumar and S. Nagar, "Model reduction by extended minimal degree optimal hankel norm approximation," *Applied Mathematical Modelling*, vol. 38, no. 11, pp. 2922–2933, 2014.

[19] X. Cao, M. B. Saltik, and S. Weiland, "Hankel model reduction for descriptor systems," in *54th IEEE Conference on Decision and Control (CDC)*, 2015, pp. 4668–4673.

[20] Y. Kawano and J. M. A. Scherpen, "Model reduction by differential balancing based on nonlinear hankel operators," *IEEE Transactions on Automatic Control*, vol. 62, no. 7, pp. 3293–3308, 2017.

[21] A. Antoulas, J. Ball, J. Kang, and J. Willems, "On the solution of the minimal rational interpolation problem," *Linear Algebra and its Applications*, vol. 137, pp. 511–573, 1990.

[22] T. T. Georgiou, "The interpolation problem with a degree constraint," *IEEE Transactions on Automatic Control*, vol. 44, no. 3, pp. 631–635, 1999.

[23] C. I. Byrnes, T. T. Georgiou, and A. Lindquist, "A generalized entropy criterion for nevanlinna-pick interpolation with degree constraint," *IEEE Transactions on Automatic Control*, vol. 46, no. 6, pp. 822–839, 2001.

[24] K. Gallivan, A. Vandendorpe, and P. Van Dooren, "Sylvester equations and projection-based model reduction," *Journal of Computational and Applied Mathematics*, vol. 162, no. 1, pp. 213–229, 2004.

[25] C. A. Beattie and S. Gugercin, "Interpolation theory for structure-preserving model reduction," in *47th IEEE Conference on Decision and Control (CDC)*, 2008, pp. 4204–4208.

[26] S. Gugercin, A. C. Antoulas, and C. Beattie, "$\mathcal{H}_2$ model reduction for large-scale linear dynamical systems," *SIAM journal on matrix analysis and applications*, vol. 30, no. 2, pp. 609–638, 2008.

[27] C. Beattie and S. Gugercin, "Interpolatory projection methods for structure-preserving model reduction," *Systems & Control Letters*, vol. 58, no. 3, pp. 225–232, 2009.

[28] U. Baur, C. Beattie, P. Benner, and S. Gugercin, "Interpolatory projection methods for parameterized model reduction," *SIAM Journal on Scientific Computing*, vol. 33, no. 5, pp. 2489–2518, 2011.

[29] N. Monshizadeh, H. L. Trentelman, and M. K. Camlibel, "Projection-based model reduction of multi-agent systems using graph partitions," *IEEE Transactions on Control of Network Systems*, vol. 1, no. 2, pp. 145–154, 2014.

[30] P. Benner, S. Gugercin, and K. Willcox, "A survey of projection-based model reduction methods for parametric dynamical systems," *SIAM Review*, vol. 57, no. 4, pp. 483–531, 2015.

[31] K. Kunisch and S. Volkwein, "Control of the burgers equation by a reduced-order approach using proper orthogonal decomposition," *Journal of optimization theory and applications*, vol. 102, pp. 345–371, 1999.

[32] K. Willcox and J. Peraire, "Balanced model reduction via the proper orthogonal decomposition," *AIAA journal*, vol. 40, no. 11, pp. 2323–2330, 2002.

[33] C. W. Rowley, "Model reduction for fluids, using balanced proper orthogonal decomposition," *International Journal of Bifurcation and Chaos*, vol. 15, no. 03, pp. 997–1013, 2005.

[34] K. Kunisch and S. Volkwein, "Proper orthogonal decomposition for optimality systems," *ESAIM: Mathematical Modelling and Numerical Analysis*, vol. 42, no. 1, pp. 1–23, 2008.

[35] P. Astrid, S. Weiland, K. Willcox, and T. Backx, "Missing point estimation in models described by proper orthogonal decomposition," *IEEE Transactions on Automatic Control*, vol. 53, no. 10, pp. 2237–2251, 2008.

[36] B. Kramer and K. E. Willcox, "Nonlinear model order reduction via lifting transformations and proper orthogonal decomposition," *AIAA Journal*, vol. 57, no. 6, pp. 2297–2307, 2019.

[37] L. S. Louca and J. L. Stein, "Energy-based model reduction of linear systems," in *6th Vienna International Conference on Mathematical Modelling*, 1999, pp. 629–639.

[38] W. S. Gray and J. Mesko, "General input balancing and model reduction for linear and nonlinear systems," in *1997 European Control Conference (ECC)*, 1997, pp. 2862–2867.

[39] J. M. Scherpen and W. S. Gray, "Minimality and local state decompositions of a nonlinear state space realization using energy functions," *IEEE Transactions on Automatic Control*, vol. 45, no. 11, pp. 2079–2086, 2000.

[40] ——, "Nonlinear hilbert adjoints: Properties and applications to hankel singular value analysis," *Nonlinear Analysis: Theory, Methods & Applications*, vol. 51, no. 5, pp. 883–901, 2002.

[41] M. Ilyas Ahmad, P. Benner, and I. Jaimoukha, "Krylov subspace methods for model reduction of quadratic-bilinear systems," *IET Control Theory & Applications*, vol. 10, no. 16, pp. 2010–2018, 2016.

[42] I. V. Gosea and A. C. Antoulas, "Data-driven model order reduction of quadratic-bilinear systems," *Numerical Linear Algebra with Applications*, vol. 25, no. 6, p. e2200, 2018.

[43] P. Benner, P. Goyal, and S. Gugercin, "$\mathcal{H}_2$-quasi-optimal model order reduction for quadratic-bilinear control systems," *SIAM Journal on Matrix Analysis and Applications*, vol. 39, no. 2, pp. 983–1032, 2018.

[44] H. Bai, T. Mylvaganam, and G. Scarciotti, "Model reduction for quadratic-bilinear systems using nonlinear moments," in *2022 European Control Conference (ECC)*, 2022, pp. 1702–1707.

[45] H. Bai and G. Scarciotti, "Two-sided interconnection-based model reduction for quadratic-bilinear systems," *IFAC-PapersOnLine*, vol. 58, no. 5, pp. 108–113, 2024.

[46] S. Lall, P. Krysl, and J. E. Marsden, "Structure-preserving model reduction for mechanical systems," *Physica D: Nonlinear Phenomena*, vol. 184, no. 1-4, pp. 304–318, 2003.

[47] K. Fujimoto, "Balanced realization and model order reduction for port-hamiltonian systems," *Journal of System Design and Dynamics*, vol. 2, no. 3, pp. 694–702, 2008.

[48] A. Astolfi, "Model reduction by moment matching for linear and nonlinear systems," *IEEE Transactions on Automatic Control*, vol. 55, no. 10, pp. 2321–2336, 2010.

[49] G. Scarciotti and A. Astolfi, "Data-driven model reduction by moment matching for linear and nonlinear systems," *Automatica*, vol. 79, pp. 340–351, 2017.

[50] ——, "Interconnection-based model order reduction - a survey," *European Journal of Control*, vol. 75, p. 100929, 2024.

[51] Y. Chahlaoui and P. Van Dooren, "Benchmark examples for model reduction," https://www.slicot.org/20-site/126-benchmark-examples-for-model-reduction, 2002.

[52] ——, "A collection of benchmark examples for model reduction of linear time-invariant dynamical systems." http://eprints.ma.man.ac.uk/1040, 2002.

[53] J. Mao and G. Scarciotti, "Data-driven model reduction by moment matching for linear systems through a swapped interconnection," in *2022 European Control Conference (ECC)*, 2022, pp. 1690–1695.

[54] A. Isidori, J. van Schuppen, E. Sontag, M. Thoma, and M. Krstic, "Communications and control engineering," *Nonlinear control systems*, 1995.

[55] J. Mao and G. Scarciotti, "Data-driven model order reduction simultaneously matching linear and nonlinear moments," *IEEE Control Systems Letters*, vol. 8, pp. 2331–2336, 2024.

[56] I. V. Gosea and A. C. Antoulas, "Data-driven model order reduction of quadratic-bilinear systems," *Numerical Linear Algebra with Applications*, vol. 25, no. 6, p. e2200, 2018.

[57] A. Junyent Ferré, "Control of power electronic converters for the operation of wind generation," Ph.D. dissertation, Universitat Politècnica de Catalunya, 2011.

[58] S. Heier, *Grid integration of wind energy: onshore and offshore conversion systems*. John Wiley & Sons, 2014.

[59] J. F. Manwell, J. G. McGowan, and A. L. Rogers, *Wind energy explained: theory, design and application*. John Wiley & Sons, 2010.

[60] M. Kesraoui, N. Korichi, and A. Belkadi, "Maximum power point tracker of wind energy conversion system," *Renewable energy*, vol. 36, no. 10, pp. 2655–2662, 2011.

[61] Y. Xia, K. H. Ahmed, and B. W. Williams, "Wind turbine power coefficient analysis of a new maximum power point tracking technique," *IEEE Transactions on Industrial Electronics*, vol. 60, no. 3, pp. 1122–1132, 2012.

[62] M. A. Abdullah, A. Yatim, C. W. Tan, and R. Saidur, "A review of maximum power point tracking algorithms for wind energy systems," *Renewable and Sustainable Energy Reviews*, vol. 16, no. 5, pp. 3220–3227, 2012.

[63] D. Goodfellow and G. Smith, "Control strategy for variable speed of a fixed-pitch wind turbine operating in a wide speed range," in *8th BWEA Conference*, 1986, pp. 219–228.

[64] R. Leidhold, G. Garcia, and M. Valla, "Maximum efficiency control for variable speed wind driven generators with speed and power limits," in *28th Annual Conference of the Industrial Electronics Society*, vol. 1. IEEE, 2002, pp. 157–162.

[65] L. Harnefors and H.-P. Nee, "Model-based current control of ac machines using the internal model control method," *IEEE Transactions on Industry Applications*, vol. 34, no. 1, pp. 133–141, 1998.

[66] H. Díaz and C. G. Soares, "Review of the current status, technology and future trends of offshore wind farms," *Ocean Engineering*, vol. 209, p. 107381, 2020.

[67] U.S. Energy Information Administration, "Monthly energy review," https://www.eia.gov/todayinenergy/detail.php?id=43675, 2020.

[68] G. Scarciotti, "Low computational complexity model reduction of power systems with preservation of physical characteristics," *IEEE Transactions on Power Systems*, vol. 32, no. 1, pp. 743–752, 2016.

[69] H. R. Ali, L. P. Kunjumuhammed, B. C. Pal, A. G. Adamczyk, and K. Vershinin, "Model order reduction of wind farms: Linear approach," *IEEE Transactions on Sustainable Energy*, vol. 10, no. 3, pp. 1194–1205, 2018.

[70] ——, "A trajectory piecewise-linear approach to nonlinear model order reduction of wind farms," *IEEE Transactions on Sustainable Energy*, vol. 11, no. 2, pp. 894–905, 2019.

[71] H. R. Ali and B. C. Pal, "Model order reduction of multi-terminal direct-current grid systems," *IEEE Transactions on Power Systems*, vol. 36, no. 1, pp. 699–711, 2020.

[72] V. Akhmatov and H. Knudsen, "An aggregate model of a grid-connected, large-scale, offshore wind farm for power stability investigations—importance of windmill mechanical system," *International Journal of Electrical Power & Energy Systems*, vol. 24, no. 9, pp. 709–717, 2002.

[73] J. Slootweg and W. Kling, "Aggregated modelling of wind parks in power system dynamics simulations," in *2003 IEEE Bologna Power Tech Conference Proceedings,*, vol. 3, 2003, pp. 6–pp.

[74] L. M. Fernández, F. Jurado, and J. R. Saenz, "Aggregated dynamic model for wind farms with doubly fed induction generator wind turbines," *Renewable Energy*, vol. 33, no. 1, pp. 129–140, 2008.

[75] L. Fernandez, C. Garcia, J. Saenz, and F. Jurado, "Equivalent models of wind farms by using aggregated wind turbines and equivalent winds," *Energy Conversion and Management*, vol. 50, no. 3, pp. 691–704, 2009.

[76] M. Ali, I.-S. Ilie, J. V. Milanovic, and G. Chicco, "Wind farm model aggregation using probabilistic clustering," *IEEE Transactions on Power Systems*, vol. 28, no. 1, pp. 309–316, 2012.

[77] J. Zou, C. Peng, H. Xu, and Y. Yan, "A fuzzy clustering algorithm-based dynamic equivalent modeling method for wind farm with dfig," *IEEE Transactions on Energy Conversion*, vol. 30, no. 4, pp. 1329–1337, 2015.

[78] P. Wang, Z. Zhang, Q. Huang, N. Wang, X. Zhang, and W.-J. Lee, "Improved wind farm aggregated modeling method for large-scale power system stability studies," *IEEE Transactions on Power Systems*, vol. 33, no. 6, pp. 6332–6342, 2018.

[79] B. Moore, "Principal component analysis in linear systems: Controllability, observability, and model reduction," *IEEE Transactions on Automatic Control*, vol. 26, no. 1, pp. 17–32, 1981.

[80] S. Gugercin and A. C. Antoulas, "A survey of model reduction by balanced truncation and some new results," *International Journal of Control*, vol. 77, no. 8, pp. 748–766, 2004.

[81] E. J. Grimme, "Krylov projection methods for model reduction," Ph.D. dissertation, University of Illinois at Urbana-Champaign, 1997.

[82] V. Druskin and V. Simoncini, "Adaptive rational krylov subspaces for large-scale dynamical systems," *Systems & Control Letters*, vol. 60, no. 8, pp. 546–560, 2011.

[83] D. Chaniotis and M. Pai, "Model reduction in power systems using krylov subspace methods," *IEEE Transactions on Power Systems*, vol. 20, no. 2, pp. 888–894, 2005.

[84] F. D. Freitas, J. Rommes, and N. Martins, "Gramian-based reduction method applied to large sparse power system descriptor models," *IEEE Transactions on Power Systems*, vol. 23, no. 3, pp. 1258–1270, 2008.

[85] J. H. Chow, *Power system coherency and model reduction*. Springer, 2013, vol. 84.

[86] C. Sturk, L. Vanfretti, Y. Chompoobutrgool, and H. Sandberg, "Coherency-independent structured model reduction of power systems," *IEEE Transactions on Power Systems*, vol. 29, no. 5, pp. 2418–2426, 2014.

[87] V. Druskin, L. Knizhnerman, and V. Simoncini, "Analysis of the rational krylov subspace and adi methods for solving the lyapunov equation," *SIAM Journal on Numerical Analysis*, vol. 49, no. 5, pp. 1875–1898, 2011.

[88] S. Gugercin, C. Beattie, and A. Antoulas, "Rational krylov methods for optimal h_2 model reduction," in *17th International Symposium on Mathematical Theory of Networks and Systems (MTNS)*, 2006, pp. 1665–1667.

[89] J. Mao and G. Scarciotti, "Data-driven model reduction by two-sided moment matching," *Automatica*, vol. 166, p. 111702, 2024.

[90] M. F. Shakib, G. Scarciotti, A. Y. Pogromsky, A. Pavlov, and N. van de Wouw, "Time-domain moment matching for multiple-input multiple-output linear time-invariant models," *Automatica*, vol. 152, p. 110935, 2023.

[91] T. C. Ionescu, "Two-sided time-domain moment matching for linear systems," *IEEE Transactions on Automatic Control*, vol. 61, no. 9, pp. 2632–2637, 2015.

[92] A. Padoan, G. Scarciotti, and A. Astolfi, "A geometric characterization of the persistence of excitation condition for the solutions of autonomous systems," *IEEE Transactions on Automatic Control*, vol. 62, no. 11, pp. 5666–5677, 2017.

[93] R. Vinter, *Optimal Control*, ser. Modern Birkhäuser Classics. Birkhäuser Boston, 2010.

[94] J. Yong and X. Y. Zhou, *Stochastic Controls: Hamiltonian Systems and HJB Equations*, ser. Stochastic Modelling and Applied Probability. Springer New York, 1999.

[95] A. J. van der Schaft, *$\mathcal{L}_2$-Gain and Passivity Techniques in Nonlinear Control*. Springer-Verlag, 1996.

[96] D. Hinrichsen and A. Pritchard, "Stochastic $\mathcal{H}^\infty$," *SIAM Journal on Control and Optimization*, vol. 36, no. 5, pp. 1504–1538, 1998.

[97] T. S. Basar and P. Bernhard, *$\mathcal{H}^\infty$-Optimal Control and Related Minimax Design Problems: A Dynamic Game Approach*, ser. Systems & Control. Bikháuser, 2008.

[98] V. A. Ugrinovskii, "Robust H_∞ infinity control in the presence of stochastic uncertainty," *International Journal of Control*, vol. 71, no. 2, pp. 219–237, 1998.

[99] R. W. Beard, G. N. Saridis, and J. T. Wen, "Galerkin approximations of the generalized hamilton-jacobi-bellman equation," *Automatica*, vol. 33, no. 12, pp. 2159–2177, 1997.

[100] F.-Y. Wang and G. Saridis, "Suboptimal control for nonlinear stochastic systems," in *31st Conference on Decision and Control (CDC)*, 1992, pp. 1856–1861.

[101] Z. Chen and S. Jagannathan, "Generalized hamilton–jacobi–bellman formulation-based neural network control of affine nonlinear discrete-time systems," *IEEE Transactions on Neural Networks*, vol. 19, no. 1, pp. 90–106, 2008.

[102] M. Falcone and R. Ferretti, "Discrete time high-order schemes for viscosity solutions of hamilton-jacobi-bellman equations," *Numerische Mathematik*, vol. 67, no. 3, pp. 315–344, 1994.

[103] M. Sassano, T. Mylvaganam, and A. Astolfi, "An algebraic approach to dynamic optimisation of nonlinear systems: a survey and some new results," *Journal of Control and Decision*, vol. 6, no. 1, pp. 1–29, 2019.

[104] M. Sassano and A. Astolfi, "Dynamic approximate solutions of the HJ inequality and of the HJB equation for input-affine nonlinear systems," *IEEE Transactions on Automatic Control*, vol. 57, no. 10, pp. 2490–2503, 2012.

[105] ——, "Approximate finite-horizon optimal control without PDE's," *Systems & Control Letters*, vol. 62, no. 2, pp. 97–103, 2013.

[106] G. Scarciotti and A. Astolfi, "Approximate finite-horizon optimal control for input-affine nonlinear systems with input constraints," *Journal of Control and Decision*, vol. 1, no. 2, pp. 149–165, 2014.

[107] T. Mylvaganam and M. Sassano, "Approximate optimal control via measurement feedback for a class of nonlinear systems," *Proceedings of the 20th IFAC World Congress*, vol. 50, no. 1, pp. 15 391–15 396, 2017.

[108] ——, "Disturbance attenuation by measurement feedback in nonlinear systems via immersion and algebraic conditions," *IEEE Transactions on Automatic Control*, vol. 65, no. 2, pp. 854–860, 2020.

[109] T. Mylvaganam and A. Astolfi, "A Nash game approach to mixed $\mathcal{H}_2/\mathcal{H}_\infty$ control for input-affine nonlinear systems," *10th IFAC Symposium on Nonlinear Control Systems*, vol. 49, no. 18, pp. 1024–1029, 2016.

[110] T. Mylvaganam, M. Sassano, and A. Astolfi, "Constructive ϵ-Nash equilibria for nonzero-sum differential games," *IEEE Transactions on Automatic Control*, vol. 60, no. 4, pp. 950–965, 2015.

[111] M. Wang, "Stochastic $\mathcal{H}_2/\mathcal{H}_\infty$ control with random coefficients," *Chinese Annals of Mathematics, Series B*, vol. 34, no. 5, pp. 733–752, 2013.

[112] G. Scarciotti and T. Mylvaganam, "Approximate infinite-horizon optimal control for stochastic systems," in *57th Conference on Decision and Control (CDC)*, 2018, pp. 3294–3298.

[113] L. Arnold, *Stochastic Differential Equations*, ser. A Wiley-Interscience publication. Wiley, 1974.

[114] F. Kozin, "A survey of stability of stochastic systems," *Automatica*, vol. 5, no. 1, pp. 95–112, 1969.

[115] L. Arnold, *Stochastic differential equations*, ser. A Wiley-Interscience publication. Wiley, 1974.

[116] M. A. Rami and X. Y. Zhou, "Linear matrix inequalities, Riccati equations, and indefinite stochastic linear quadratic controls," *IEEE Transactions on Automatic Control*, vol. 45, no. 6, pp. 1131–1143, 2000.

[117] S. Chen, X. Li, and X. Y. Zhou, "Stochastic linear quadratic regulators with indefinite control weight costs," *SIAM Journal on Control and Optimization*, vol. 36, no. 5, pp. 1685–1702, 1998.

[118] A. Astolfi, "Singular $\mathcal{H}_\infty$ control for nonlinear systems," *International Journal of Robust and Nonlinear Control*, vol. 7, no. 7, pp. 727–740, 1997.

[119] A. Wernli and G. Cook, "Suboptimal control for the nonlinear quadratic regulator problem," *Automatica*, vol. 11, no. 1, pp. 75–84, 1975.

[120] K. M. Anstreicher and M. H. Wright, "A note on the augmented Hessian when the reduced Hessian is semidefinite," *SIAM Journal on Optimization*, vol. 11, no. 1, pp. 243–253, 2000.

[121] X. Mao, "Stochastic versions of the LaSalle theorem," *Journal of Differential Equations*, vol. 153, no. 1, pp. 175–195, 1999.

[122] T. Çimen, "State-dependent Riccati equation (SDRE) control: A survey," *IFAC Proceedings Volumes*, vol. 41, no. 2, pp. 3761–3775, 2008, 17th IFAC World Congress.

[123] T.-J. Tarn and Y. Rasis, "Observers for nonlinear stochastic systems," *IEEE Transactions on Automatic Control*, vol. 21, no. 4, pp. 441–448, 1976.

[124] E. Yaz and A. Azemi, "Observer design for discrete and continuous non-linear stochastic systems," *International Journal of Systems Science*, vol. 24, no. 12, pp. 2289–2302, 1993.

[125] Y. Niu and D. W. Ho, "Robust observer design for itô stochastic time-delay systems via sliding mode control," *Systems & Control Letters*, vol. 55, no. 10, pp. 781–793, 2006.

[126] X. Fang and J. Wang, "Stochastic observer-based guaranteed cost control for networked control systems with packet dropouts," *IET Control Theory & Applications*, vol. 2, no. 11, pp. 980–989, 2008.

[127] E. Yaz and A. Azemi, "Lyapunov-based nonlinear observer, design for stochastic systems," in *29th IEEE Conference on Decision and Control (CDC)*, 1990, pp. 218–219.

[128] C. S. Jeong, E. E. Yaz, and Y. I. Yaz, "Stochastically resilient observer design for a class of continuous-time nonlinear systems," *IFAC Proceedings Volumes*, vol. 44, no. 1, pp. 1843–1848, 2011.

[129] A. P. Dani, S.-J. Chung, and S. Hutchinson, "Observer design for stochastic nonlinear systems using contraction analysis," in *51st IEEE Conference on Decision and Control (CDC)*, 2012, pp. 6028–6035.

[130] A. Barbata, M. Zasadzinski, and H. S. Ali, "H∞ observer design for a class of nonlinear singular stochastic systems," *IFAC-PapersOnLine*, vol. 50, no. 1, pp. 3885–3892, 2017.

[131] S. Bratan and S. Roshchupkin, "Synthesis of lunberger stochastic observer for estimation of the grinding operation state," in *MATEC Web of Conferences*, vol. 224. EDP Sciences, 2018, p. 01133.

[132] Y. Liu and J. Zhang, "Reduced-order observer-based control design for nonlinear stochastic systems," *Systems & Control Letters*, vol. 52, no. 2, pp. 123–135, 2004.

[133] X. Hulhoven, R. Hanus, and P. Bogaerts, "Stochastic hybrid observer for bioprocess state estimation," *IFAC Proceedings Volumes*, vol. 37, no. 3, pp. 19–24, 2004.

[134] T. Damm, *Rational Matrix Equations in Stochastic Control*, ser. Lecture Notes in Control and Information Sciences. Springer, 2004.

[135] A. Mellone and G. Scarciotti, "Output regulation of linear stochastic systems," *IEEE Transactions on Automatic Control*, vol. 67, no. 4, pp. 1728–1743, 2021.

[136] T. C. Gard, *Introduction to Stochastic Differential Equations*, ser. Monographs and textbooks in pure and applied mathematics. M. Dekker, 1988.

[137] L. Huang, H. Hjalmarsson, and H. Koeppl, "Almost sure stability and stabilization of discrete-time stochastic systems," *Systems & Control Letters*, vol. 82, pp. 26–32, 2015.

[138] A. Mellone and G. Scarciotti, "Error-feedback output regulation of linear stochastic systems: a hybrid nonlinear approach," *IFAC-PapersOnLine*, vol. 52, no. 16, pp. 520–525, 2019.

[139] ——, "Stochastic relative degree and path-wise control of nonlinear stochastic systems," *IEEE Transactions on Automatic Control*, vol. 68, no. 4, pp. 1970–1985, 2023.

[140] L. M. Leon, A. S. Bretas, and S. Rivera, "Quadratically constrained quadratic programming formulation of contingency constrained optimal power flow with photovoltaic generation," *Energies*, 2020.